Institute of Geophysics
Polish Academy of Sciences

PUBLICATIONS
OF THE INSTITUTE OF GEOPHYSICS
POLISH ACADEMY OF SCIENCES

Geophysical Data Bases, Processing and Instrumentation

442 (D-77)

Atmospheric Electricity: Papers on Thunderstorm and Cloud Electricity

Warsaw 2022 (Issue 4)

INSTITUTE OF GEOPHYSICS
POLISH ACADEMY OF SCIENCES

PUBLICATIONS
OF THE INSTITUTE OF GEOPHYSICS
POLISH ACADEMY OF SCIENCES

Geophysical Data Bases, Processing and Instrumentation

442 (D-77)

Atmospheric Electricity:
Papers on Thunderstorm and Cloud Electricity

Warsaw 2022

Honorary Editor
Roman TEISSEYRE

Editor-in-Chief
Marek KUBICKI

Advisory Editorial Board
Janusz BORKOWSKI (Institute of Geophysics, PAS)
Tomasz ERNST (Institute of Geophysics, PAS)
Maria JELEŃSKA (Institute of Geophysics, PAS)
Andrzej KIJKO (University of Pretoria, Pretoria, South Africa)
Natalia KLEIMENOVA (Institute of Physics of the Earth, Russian Academy of Sciences, Moscow, Russia)
Zbigniew KŁOS (Space Research Center, Polish Academy of Sciences, Warsaw, Poland)
Jan KOZAK (Geophysical Institute, Prague, Czech Republic)
Antonio MELONI (Instituto Nazionale di Geofisica, Rome, Italy)
Hiroyuki NAGAHAMA (Tohoku University, Sendai, Japan)
Kaja PIETSCH (AGH University of Science and Technology, Cracow, Poland)
Paweł M. ROWIŃSKI (Institute of Geophysics, PAS)
Steve WALLIS (Heriot Watt University, Edinburgh, United Kingdom)
Wacław M. ZUBEREK (University of Silesia, Sosnowiec, Poland)

Associate Editors
Łukasz RUDZIŃSKI (Institute of Geophysics, PAS) – **Solid Earth Sciences**
Jan WISZNIOWSKI (Institute of Geophysics, PAS) – **Seismology**
Jan REDA (Institute of Geophysics, PAS) – **Geomagnetism**
Krzysztof MARKOWICZ (Institute of Geophysics, Warsaw University) – **Atmospheric Sciences**
Mark GOŁKOWSKI (University of Colorado Denver) – **Ionosphere and Magnetosphere**
Andrzej KUŁAK (AGH University of Science and Technology) – **Atmospheric Electricity**
Marzena OSUCH (Institute of Geophysics, PAS) – **Hydrology**
Adam NAWROT (Institute of Geophysics, PAS) – **Polar Sciences**

Managing Editor
Anna DZIEMBOWSKA

Technical Editor
Marzena CZARNECKA

Published by the Institute of Geophysics, Polish Academy of Sciences

ISBN 978-83-66254-14-5 eISSN-2299-8020
DOI: 10.25171/InstGeoph_PAS_Publs-2022-020

Photo on the front cover by Piotr Barański

Editorial Office
Instytut Geofizyki Polskiej Akademii Nauk
ul. Księcia Janusza 64, 01-452 Warszawa

CONTENTS

Publications of the Institute of Geophysics, Polish Academy of Sciences
Geophysical Data Bases, Processing and Instrumentation
vol. 442 (D-77), 2022, pp. 3–3
DOI: 10.25171/InstGeoph_PAS_Publs-2022-021

Atmospheric Electricity: Papers on Thunderstorm and Cloud Electricity

PREFACE

Problems of thunderstorm and cloud electricity still remain in the mainstream of research of atmospheric physics researchers. Hence, in this special issue of *Publications of the Institute of Geophysics, Polish Academy of Sciences*, devoted to problems of atmospheric electricity, we present a set of six articles in which we publish some recent results on this subject, obtained by us and our co-workers. The article by Barański and Guzikowski shows how detections of cloud-to-ground lightning sources obtained from the Local Lightning and Detection Network (LLDN) operated in the Warsaw region can be supplemented by computer simulations of radar reflectivity, as well as dynamic and electric field structure of the considered thunderclouds in the WRF and WRF_ELEC models we used. In another article, Odzimek et al. describe meteorological and atmospheric electricity datasets and the methodology of analysing the atmospheric electric data from the Polish Atmospheric Electricity Observation Network used for the purpose of research studies on the electricity of Nimbostratus and Stratus clouds. Next, a series of three articles by Odzimek et al. summarise optical observations of sprite lightning Poland, made in Gliwice and Świder over 2011–2015. Finally, the article by Parfiniewicz et al. presents a new idea of using the virtual Fujita scale [VFS] number approach to assessment of lightning discharges development and severity for the derecho episode in Poland on 11 August 2017. It should be noted that for the first time the lightning detection data from the PERUN remote sensing system in Poland were successfully applied for the determination of the whole trace of a Mesoscale Convection System (MCS) with the derecho incident. This MCS was organised in the form of a very extended supercell. We have tracked the time development of such supercell with high spatial and temporal accuracy that would be impossible to obtain by using the routine radar data only.

Anna Odzimek and Piotr Barański

Received 28 November 2022
Accepted 31 December 2022

Publications of the Institute of Geophysics, Polish Academy of Sciences
Geophysical Data Bases, Processing and Instrumentation
vol. 442 (D-77), 2022, pp. 5–17
DOI: 10.25171/InstGeoph_PAS_Publs-2022-022

Dynamic and Electric Charge Structure of Thunderclouds Obtained from the WRF and WRF_ELEC Models and Related to the Charge Sources of Multiple CG Flashes Detected by the LLDN in the Warsaw Region during Thunderstorm Season in 2009

Piotr BARAŃSKI✉ and Jakub GUZIKOWSKI

Institute of Geophysics, Polish Academy of Sciences, Warsaw, Poland
✉ baranski@igf.edu.pl

Abstract

The paper presents the results of spatial location (in the coordinates of the local and rectangular Cartesian system: x, y, z) as well as the polarity and electric charge of all sources in thunderclouds discharged by individual return strokes during 17 multiple cloud-to-ground discharges recorded simultaneously by six measurement stations of the LLDN (Local Lightning Detection Network) system located in the Warsaw region in the spring and summer season of 2009. The post-time analysis of the collected digital electric field records of these discharges was carried out based on our own calculation algorithms, described in detail by Baranski et al. (2012). In turn, for two selected discharges from this group, one positive double ground flash from the 25 June 2009 storm and the other negative threefold ground flash from the 5 July 2009 storm, the supplementary simulations of radar reflectivity, the structure of the wind field and the thundercloud electric charge density were obtained from the WRF and WRF_ELEC models. Due to this, it was possible to distinguish with the time resolution up to 1 minute such regions of the thundercloud in which the simulated wind field and electric charge densities with different polarity created favourable conditions to initiate all return strokes of the considered multiple ground flashes and detected by the LLDN network. It also should be noted that the time resolution in the available routine radar observations from the IMWM-NRI is by one order of magnitude worse than the one delivered by the WRF simulations and amounts to 10 minutes.

Keywords: multiple ground flash, return stroke, lightning detection, thundercloud, WRF and WRF_ELEC models.

---

1. INTRODUCTION

In summer 2009 we have successfully operated the Local Lightning Detection Network (LLDN) in the Warsaw region that was consisting of 6 E-field measurements performed at the ground surface. The aim of this net was to provide an additional and complementary source of CG lightning data that allowed to evaluate 3D locations of point electric charge sources, i.e., to estimate parameters x, y, z in the local set of Cartesian coordinates, and the magnitude of the electric charge, Q, involved the lightning return strokes (RS) and continuing current (CC) of the considered multiple CGs (Baranski et al. 2012). Now, taking the possibility to use the WRF_ELEC model for the refining the dynamic and electric charge structure of thunderstorms occurring in Warsaw region in that time, we have made the comparison of how these two different methods are related to each other in the description/presentation of electric build up of the same thundercloud and in time when we were able to record lightning flash incident by the LLDN and initiated by this cloud.

The WRF_ELEC is an additional module dedicated to the Weather Research and Forecasting numerical model (WRF). It contains the basic electrification microphysics parameterization scheme prepared by the National Severe Storms Lab (NSSL) from Norman, Oklahoma, USA. The WRF is a system defined for numerical simulation of atmospheric processes and weather forecast. Its dynamic solver is based on the three-dimensional compressible non-hydrostatic equations and the charge separation schemes therein are used according to description presented first by Mansell et al. (2005).

In recent years many papers were published to show how using the extended and constantly modified numerical models connected to the WRF group, for example WRF_ELEC or WRF-ARW models, can improve and broaden the study of the dynamic and electric charge structure evolution of different and complex thunderstorm systems in the USA (Mansell et al. 2010; Fierro et al. 2013). Such models have simulated the particular and characteristic stages of thundercloud electric and dynamic development with a high resolution in space and time domain by the application of the explicit electrification and lightning parameterizations to the post-time analysis of the considered thunderstorm cases. It is worth noting that the simulated bulk lightning activity for different types of thunderstorm systems occurring in the USA and obtained from the WRF models have exhibited overall good qualitative agreement with the lightning detection and location data delivered by the Earth Networks Total Lightning Network (ENTLN) for the considered severe thunderstorm episodes.

2. LLDN PERFORMANCE AND CONFIGURATION

In summer 2009 the Local Lightning Detection Network (LLDN) in the Warsaw region was set up as the result of the research project No. COST/204/2006 granted by the Polish Ministry of Science and Higher Education. In that time this net consisted of six E-field measurement stations that were located at different and distant places in the Warsaw region. Such net configuration is shown in Fig. 1 and the exemplary general view of one LLDN station is given in Fig. 2. Each LLDN measuring station records variations of the vertical component of the electric field coming from a lightning flash. The stations have been equipped with an E-field antenna with a triggering circuit, two-channel data recording device, commercial GPS receiver and a power supply system with a battery backup. The specially constructed data recorders were based on the standard PC/104 built-in computer (AMD LX800 @ 500 MHz) run on Linux operating system. Each recording device has been designed as a stand-alone station working without any operator assistance required during a measurement session. The built-in internal hard drive (~150 GB data buffer) allowed to store the recorded data for 3 days at most, i.e., 72-hour continuous recording in the fast mode with bandwidth up to 100 kHz. The full error analysis of the best search solution in the case when we had at our disposal six LLDN stations located at different places in the Warsaw region is given by Baranski et al. (2012). This paper also contains a more detailed description of our LLDN recording system performance and its calibration.

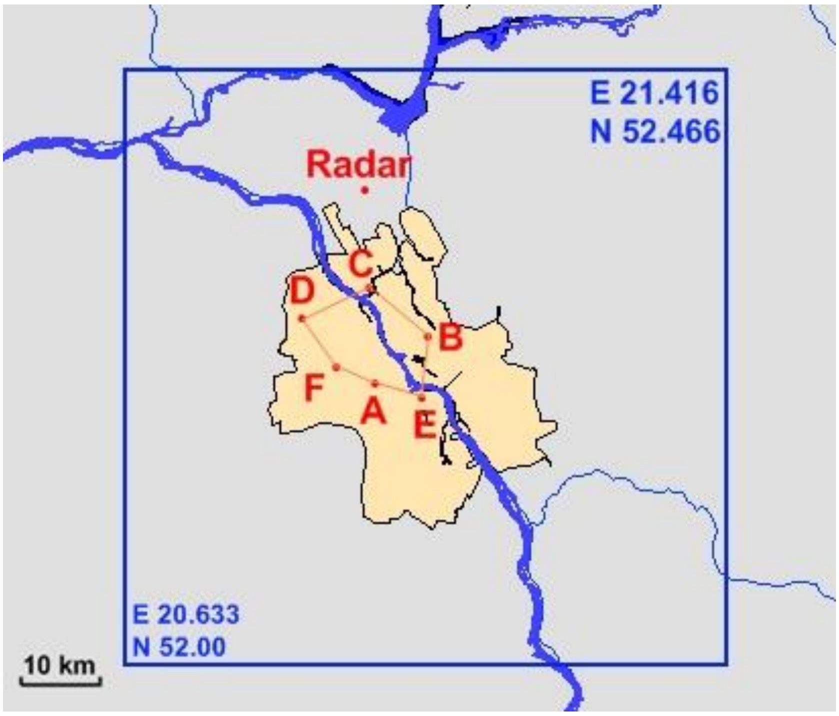

Fig. 1. Location map of six LLDN stations and meteorological radar (METEOR 1500C) set on the background of main rivers around Warsaw together with indication of the area (blue rectangle) covered by additional lightning detections obtained from the PERUN system in Poland.

Fig. 2. The general view of LLDN-F station located at the roof of IG PAS building (20°.939444 E, 52°.245833 N). The GPS/Garmin receiver and E-field antenna sensor mounted on the top of the grey box with the A/D recorder and the power supply buffer inside.

3. SIMULATION SETUP OF THE USED WRF AND WRF_ELEC SCHEME

In this section we present some principal information about the WRF system configuration together with the initial and boundary conditions that are used for the numerical study purpose. The main configuration of the WRF system we used is similar to the one presently applied by Krzyścin et al. (2020) for the comprehensive studies of 24 hr forecast of surface UV radiation in Poland. However, the main difference between these two approaches is connected to the microphysics parameterization. In our study, we used the NSSL microphysics parameterization, which was obligatory for the WRF_ELEC scheme. The NSSL is a 2-moment microphysics scheme, that allows to forecast six different precipitation types (after Mansell et al. 2010 together with Mansell and Ziegler 2013). In the scope of study of the convection weather processes, a graupel and a hail creation is important. Hence, the NSSL for this purpose uses the amount of mass and the number of thundercloud particles. The core of the WRF_ELEC, i.e., the numerical implementation of electric charge separation schemes, is taken from the work of Mansell et al. (2005). Such first implementation into the WRF model was described by Fierro et al. (2013) and included the details of the used basic discharge scheme, i.e., cylindrical discharge regions centered on lightning initiation points.

We implemented the WRF and WRF_ELEC scheme for the purpose of this paper, performing the relevant calculating procedures in three stages listed below.

3.1 The first stage

Here four nesting space domains were used for the WRF simulation. The initial and boundary weather conditions for the first domain (d01) was taken from the NCEP/NCAR Global Reanalysis Products (NCAR 2020). The spatial and temporal resolution for such data was 55×55 km and 1 h, respectively. This domain was implemented for the western and central area of Europe to simulate part of the global atmospheric circulation with a resolution of 12×12 km. The second domain (d02), operated with a resolution of 4×4 km, was dedicated only to the Poland area. The third domain (d03) with an area resolution of 1.333×1.333 km was applied to the Mazovia region and the last (d04), with an area resolution of 0.444×0.444 km, was used for the Warsaw region. For such simulations, the minimal 10-hour spin off was set. For the d01, d02, and d03 domains the 15 minutes temporal resolutions for archiving data was used, but for the d04 domain this time interval was only 1 minute. For all domains, 59 vertical levels were set between 0 and 21 km (a.g.s.l.). Only one nested run of the WRF was used, because farther simulation with the WRF_ELEC with four nested domains connected online between them was not possible. The details of the literature references used for this stage of the conducted evaluations are given in Table 1.

Table 1

The different metrological scheme options used by us for the particular WRF_ELEC procedure calculations with their related literature references

Scheme	
microphysics	NSSL 2-moment (Clark et al. 2012)
longwave radiation	RRTMG (Iacono et al. 2008)
shortwave radiation	Dudhia (Dudhia 1989)
surface layer	Eta similarity (Janjic 1996)
land surface	Pleim-Xu (Pleim and Xu 1995, 2003)
planetary boundary layer	Hong (Hong and Lim 2006)
cumulus	Tiedtke (Tiedtke 1989) only in d01

3.2 The second stage

Here we have used for the WRF_ELEC simulations its model configuration with the scheme details given in Table 2. The choice of such options was strongly imposed by the primary thundercloud electrification solver.

Table 2
The options used by us for the particular WRF_ELEC procedure calculations
with their related literature references

Scheme	
nssl_ipelec	non-inductive + inductive charging
nssl_idischarge	discharge turned on
nssl_iscreen	Ziegler et al. (1991)
nssl_lightrad	12000
nssl_disfrac	0.3
nssl_ecrit	120000
nssl_isaund	Brooks et al. (1997)
nssl_ibrkd	Dwyer (2003)

3.3 The third stage

The time intervals used for the numerical calculations for the selected two thunderstorm cases and including the time moment with the occurrence of chosen lightning CG flash are given in Table 3.

Table 3
The indication of time span used in performed relevant simulations
together with the time occurrence of two multiple CG flash incidents taken into account

Date of thunderstorm	Start of conducted simulation (UT)	Stop of conducted simulation (UT)	Time of analyzed CG flash incident with limitation to minutes (UT)
25 June 2009	06:00	23:00	16:11
5 July 2009	00:00	23:00	14:41

4. GENERAL CHARACTERISTICS OF MULTIPLE CG FLASHES RETRIEVED FROM LLDN DATABASE AND SELECTED FOR COMPARISON WITH DYNAMIC AND ELECTRIC CHARGE STRUCTURE SIMULATED BY THE WRF AND WRF_ELEC MODELS

Two exemplary cases of multiple CG flashes were selected from the LLDN database obtained in 2009 to be compared with the dynamic and electric charge structure of the particular thundercloud involved in the initiation of the considered CG flash incidents and simulated by the relevant WRF_ELEC modeling. These cases are marked by two blue shaded rows in Table 4.

Table 4

General characteristic parameters of 17 CGs lightning flashes obtained from the LLDN recordings during thunderstorm season in 2009

Flash no. (stroke order/type)	Interstroke intervals [ms]	Δd [km]	Δz [km]	Q_{total} [C]	χ^2 range
#1(1CC,2CC)	22	2.6	0.8	5.02	3÷3.6
#2(1RS,2CC,3CC,4CC)	46.9;59.3;51	12.2	7.5	–15.38	1÷40
#3(1RS,2CC,3CC)	82.7;25	0.5	0.2	–15.35	0.06÷0.3
#4(1RS,2RS,3RS,4RS,5RS,6RS)	23.7;25.8;34.1;11.3;28.9	3.8	5.8	–53.62	0.4÷2
#5(1RS,2RS,3RS)	21.3;10.5	2.7	0.4	–60.77	7÷14
#6(1RS,2RS,3RS)	41.3;28.3	1.0	3.8	–0.53	37.7÷108.9
#7(1RS,2RS,3RS)	57.8;32.9	1.0	1.4	–0.21	92.5÷177.5
#8(1RS,2RS,3RS,4RS,5CC,6RS)	55;36.2;102.7;62.1;148.1	5.7	3.8	–1.21	184.3÷223
#9(1RS,2RS,3RS,4RS)	48.2;30.7;35.1	8.1	5.8	–0.7	38.7÷187.9
#10(1RS,2RS,3RS)	40.8;36.1	0.8	0.5	–0.24	147.8÷187
#11(1RS,2RS)	49.6	4.3	0.2	–0.69	9÷20
#12(1RS,2RS,3RS)	21.2;37.8	2.7	0.1	–1.49	10÷11.6
#13(1RS,2RS,3RS)	52.3;55.9	5	0.9	–1.01	5.5÷9
#14(1RS,2RS,3RS)	70.6;66.3	6.6	0.7	–1.52	3÷6.8
#15(1RS,2RS,3RS)	46.1;66.2	0.4	1.7	–0.42	150.7÷178
#16(1RS,2RS,3RS,4RS)	32.5;64;31,7	6.4	3.4	–0.42	108÷222.8
#17(1RS,2RS)	24.6	1.0	1.7	–0.41	160÷211

Note: RS stands for return stroke, CC for continuing current, Δd for maximum horizontal flash extent, Δz for maximum vertical flash extent, Q total for total charge source of a particular flash.

In turn, the 3D locations together with the amount of electric charge of the particular return stroke sources for flashes #1 and #5 from Table 4 are presented in Figs. 3–4. Such drawings are the result of using the evaluation procedure of space configuration and electric structure of multiple CG flashes described in detail by Baranski et al. (2012).

On the other hand, the relevant WRF simulation of radar reflectivity for the 10 cm radar wavelength and for the thundercloud connected to the case of CG flash #1 is shown in Fig. 5, while in Fig. 6 is presented the related WRF_ELEC simulation of the electric charge density in the considered thundercloud resulting from the used dominant graupel cloud electrification mechanism/scheme and corresponding to the vertical cut along red line given in Fig. 5.

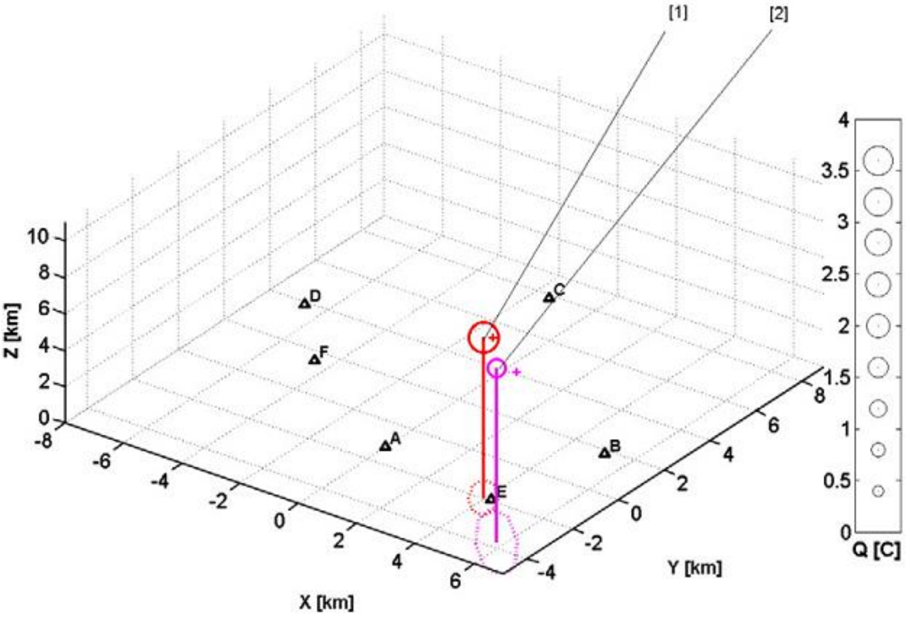

Fig. 3. Example of identification of the electric charge structure of positive multiple CG lightning flash recorded by LLDN in Warsaw during a thunderstorm on 25 June 2009. The first stroke of this flash (in red) was detected at 16:11:57.155491 UTC and the second one (in magenta) at 16:11:57.177478 UTC. Both were recognized as continuing current (CC) stages having charge sources of (3.65±0.59) C and (1.37±0.37) C, at heights, i.e., the z coordinate, (8.8±0.7) km and (9.6±0.6) km, respectively. Capital letters A, B, C, D, E, and F with small triangles indicate locations of the LLDN stations, and the red and magenta ellipses on the XY plane indicate errors of the evaluated x and y coordinates of the charge sources of these CC strokes. The goodness of the (x, y, z, Q) parameter fit was determined by calculating the χ^2 parameter which was equal to 2.5 for the first and 3.6 for the second stroke.

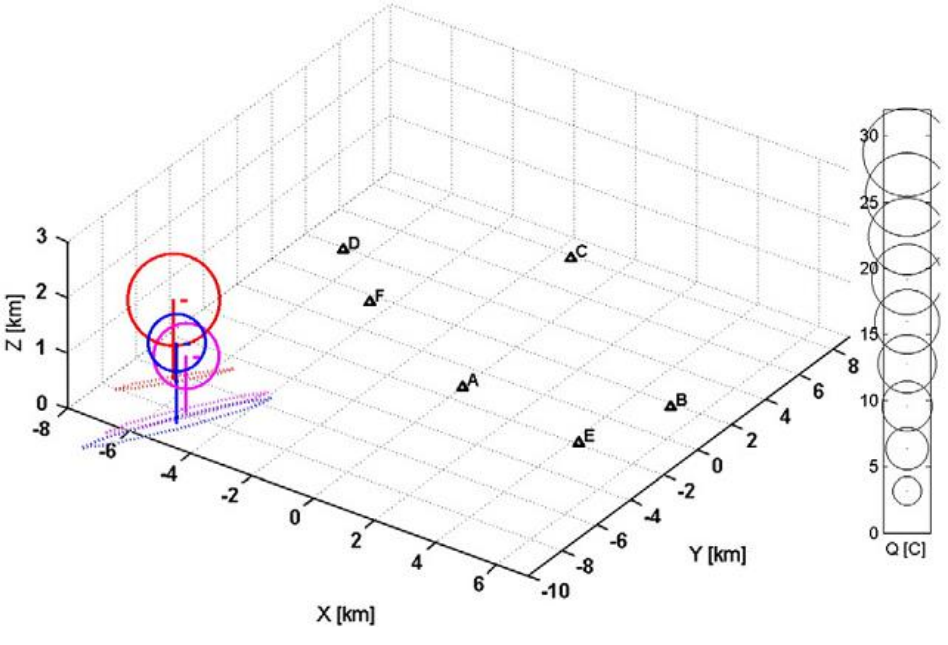

Fig. 4. Multiple negative CG flash consisting of 3 return strokes and distinguished from the LLDN data; denoting key: [red] RS on 5 July 2009, 14:41:14.3479, with $x = (-6.6\pm1.0)$ km, $y = (-6.4\pm1.7)$ km, $z = (1.4\pm7.2)$ km, $Q = (-31.75\pm165.95)$ C, and $\chi^2 = 14.0$, [magenta] RS on 5 July 2009, 14:41:14.3692, with $x = (-5.3\pm1.2)$ km, $y = (-7.9\pm2.7)$ km, $z = (1.0\pm16.4)$ km, $Q = (-16.43\pm270.21)$ C, and $\chi^2 = 7.1$, [blue] RS on 5 July 2009, 14:41:14.3797, with $x = (-5.2\pm1.4)$ km, $y = (-8.7\pm3.2)$ km, $z = (1.4\pm14.4)$ km, $Q = (-12.59\pm129.79)$ C, and $\chi^2 = 8.3$.

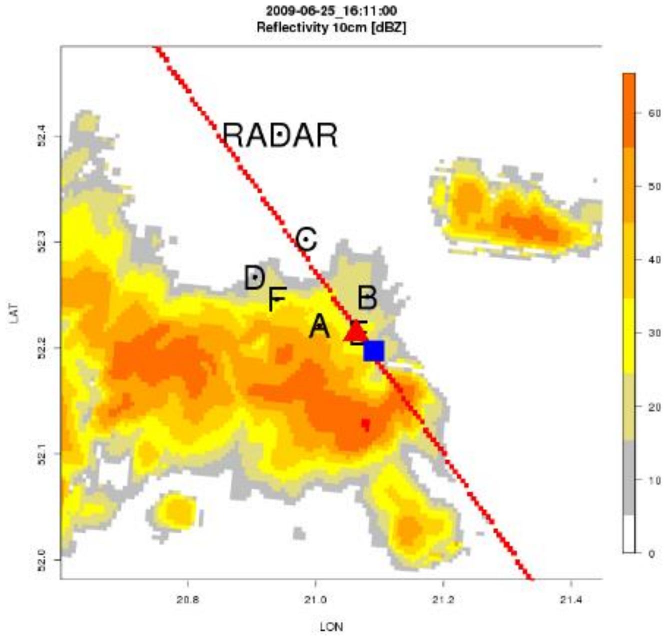

Fig. 5. The WRF simulation of radar reflectivity for the 10 cm radar wavelength and for the thundercloud connected to the case of CG flash #1. The red line is drawn as the best straightforward line fitted to the spread horizontal locations of two positive strokes from this flash and shows the best cross-section line that is used for making the subsequent vertical profile of electric charge density and updraft/downdraft wind pattern in the considered space domain. The first stroke is shown by red triangle and the second by blue square.

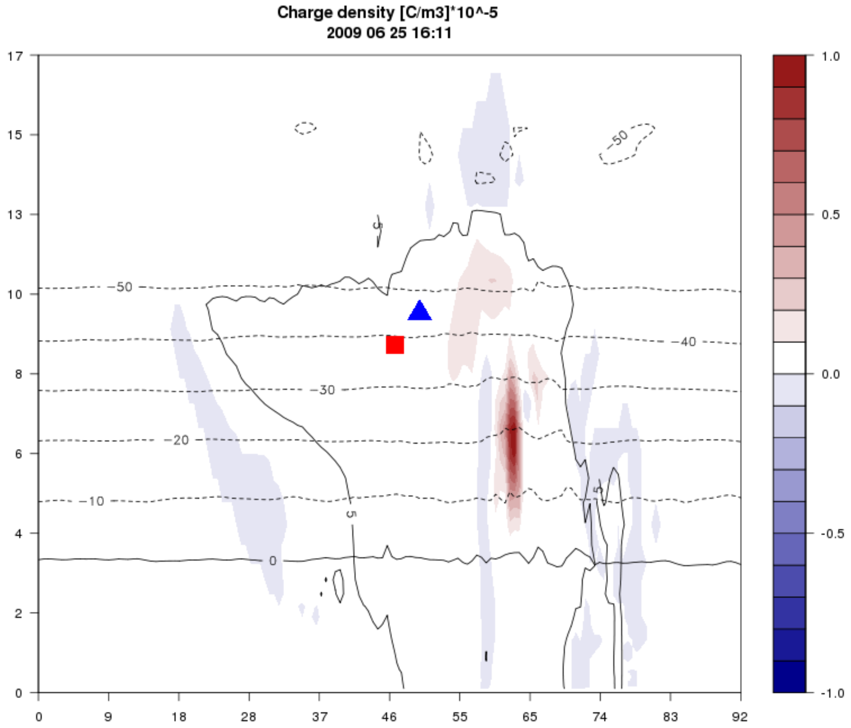

Fig. 6. The WRF_ELEC simulation of the electric charge density in the considered thundercloud resulting from the used dominant graupel cloud electrification mechanism/scheme and corresponding to the vertical cut along the red line shown in Fig. 5 The red triangle and blue square indicates the height of the electric charge source for the first and second stroke of CG flash #1, respectively, and evaluated from the LLDN recordings. The heights of the particular isotherm are given from 0°C by solid black line to –50°C by several black dash lines.

The third kind of performed WRF simulation and referred to the updraft/downdraft wind pattern in the considered thundercloud in the case of CG flash #1, and corresponding to the vertical cut along red line shown in Fig. 5, is depicted in Fig. 7.

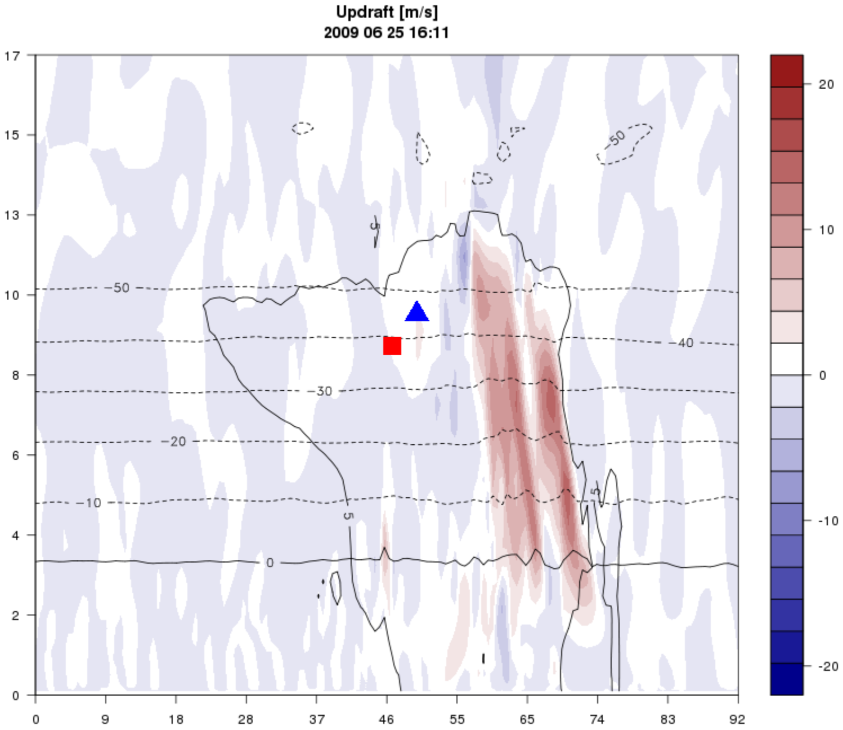

Fig. 7. The WRF simulation of the updraft/downdraft wind pattern in the considered thundercloud and corresponding to the vertical cut along red line shown in Fig. 5. The red triangle and blue square indicates the height of the electric charge source for the first and second stroke of CG flash #1, respectively, and evaluated from the LLDN recordings. The heights of the particular isotherm are given from 0°C by solid black line to –50°C by several black dash lines.

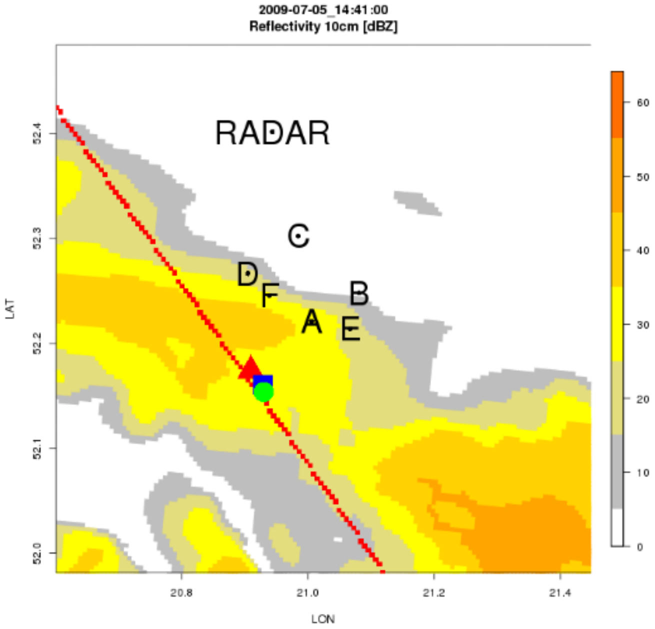

Fig. 8. Same as for Fig. 5, except the case of CG flash #5 with three negative return strokes denoted by red triangle, blue square, and green circle, respectively, and with the new drawn red line shows the best cross-section line belonging to the horizontal locations of these strokes.

The similar set of three following figures, but related to the electric and dynamic conditions of simulated thundercloud and corresponding to the next example of multiple CG flash taken into consideration, i.e., flash #5 from Table 4, is presented in Figs. 8–10.

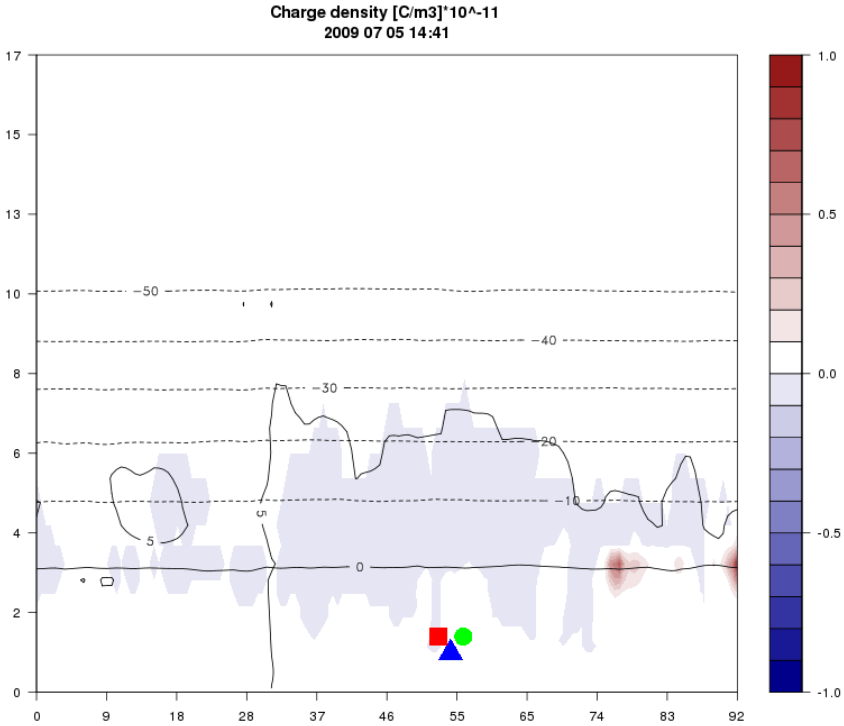

Fig. 9. Same as for Fig. 6, except the newly drawn red line shown in Fig. 8 and the case of CG flash #5 with three negative return strokes denoted by red triangle, blue square, and green circle, respectively, and with their 3D locations evaluated from the LLDN recordings.

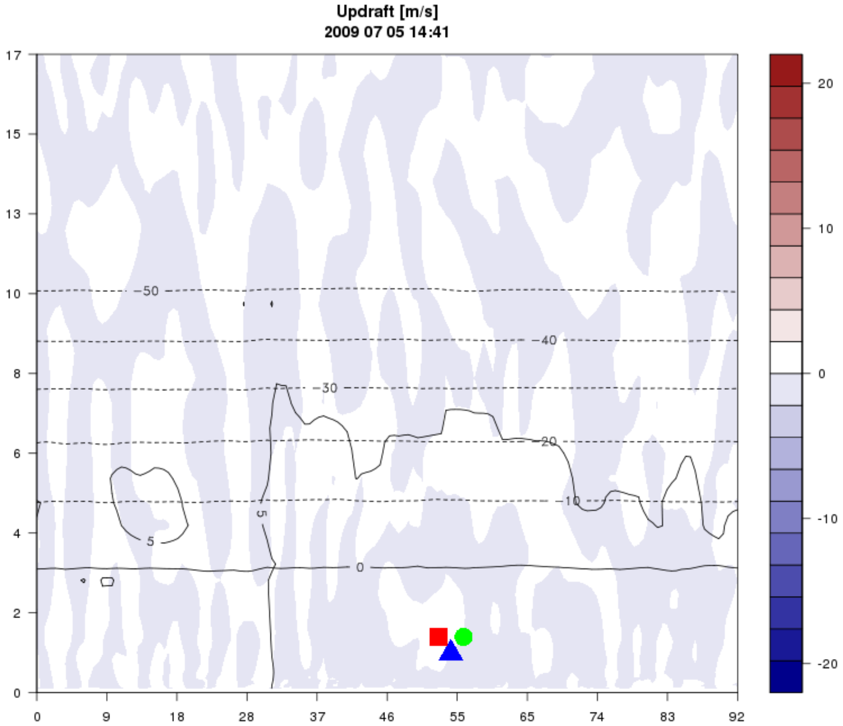

Fig. 10. Same as for Fig. 7, except the case of CG flash #5 with three negative return strokes, but with the new vertical cut along the red line shown in Fig. 8. The red triangle, blue square, and green circle, respectively, and with their 3D locations evaluated from the LLDN recordings.

5. CONCLUSIONS AND FINAL REMARKS

Comparing the 3D locations of the particular stroke from CG flash #1 presented in Fig. 3 and that one shown in Fig. 6 we can notice that these locations evaluated from the LLDN recordings are slightly shifted in relation to the volume of the uppermost positive electric charge near the cloud top and simulated/indicated by the WRF_ELEC model. This shift is less than 9 km. But, if we take into account that these locations evaluated from the LLDN recordings are also having own errors of the order of several kilometers, such a distance difference will be reduced. Moreover, the time simulation given by hours and minutes in Fig. 6 is not the same as this real/exact one with the 0.1 ms accuracy and obtained from the LLDN recordings for the time occurrence of the particular stroke from CG flash #1 (see description of Fig. 3). In that case, the time difference is 57 s. Thus, if we consider the strong updraft with a speed of about 15 m/s and spreading near the cloud top about 1 minute earlier than the exact time of occurrence of the particular stroke from CG flash #1 (see Fig. 6), the considered distance difference will be reduced by about 1 km.

The next comparison concerns the 3D locations of the particular stroke from CG flash #5 presented in Fig. 4 and the one shown in Fig. 9. Here, we have considered the multiple CG flash incident that has occurred below the height of 0°C isotherm and near the cloud base. Both the LLDN recordings and simulations obtained from the used WRF_ELEC model agree/confirm that the initiation of the particular stroke from CG flash #5 is coupled with some negative electric charge volumes appearing near the cloud base and joined to some precipitation shafts (see Fig. 10). For this case, the time difference between the time of the WRF_ELEC simulation and this one for the occurrence of the particular stroke from CG flash #5 (see description of Fig. 4) is only about 14 s. Hence, a possible distance corrections of mutual return stroke locations and displacement of negative electric charge volume evaluated from both methods/ways will be very small, not greater than about 20 m (see Fig. 10 and downdraft speed in the location region of the particular stroke from CG flash #5).

It is worth to note that while the E-field records obtained from the LLDN performance have given us a possibility to evaluate the 3D location and electric charge source of the particular CG stroke according to the one point electrostatic model we used, the conducted WRF_ELEC simulations in the selected vertical cross-section have indicated what kind of electric charge density space distribution/pattern could be involved in such CG flash initiation. These simulations can be carried out with an additional assumption that the inductive or non-inductive processes, or both of them, in the considered thundercloud were responsible for its resultant electrification. On the other hand, the calculated representation/picture of temperature, the updraft/downdraft wind field patterns and the radar reflectivity for 10 cm wavelength delivered by the WRF_ELEC model is supplementary and important information about the microphysical conditions/parameters that may be observed in the surroundings of this electric charge source of the particular lightning stroke detected by the LLDN.

Summarizing, it should be added that both ways of our post-time analysis, i.e., the LLDN recordings of electric field change of return strokes from multiple CG flashes and the results of WRF and WRF_ELEC model simulations, are also allowing to do a supplementary assessment of thundercloud electric charge patterns involved in the initiation of the considered two cases of multiple CG flashes of different polarity, have given coherent final results confirming their suitability and usefulness for future research and location of electric charge sources of ground strokes and dynamic conditions of those thundercloud regions/layers essential for such lightning occurrence. The high time resolution of the WRF and WRF_ELEC simulations of 1 min, i.e., an order of magnitude better than the one routinely available from the IMWM-NRI radar in Legionowo, is also important and valuable improvement in such examinations.

Acknowledgments. This work was partially supported within statutory activities No. 3841/E-41/S/2020 of Poland's Ministry of Education and Science.

References

Baranski, P., M. Loboda, J. Wiszniowski, and M. Morawski (2012), Evaluation of multiple ground flash charge structure from electric field measurements using the local lightning detection network in the region of Warsaw, *Atmos. Res.* **117**, 99–110, DOI: 10.1016/j.atmosres.2011.10.011.

Brooks, I.M., C.P.R. Saunders, R.P. Mitzeva, and S.L. Peck (1997), The effect on thunderstorm charging of the rate of rime accretion by graupel, *Atmos. Res.* **43**, 3, 277–295, DOI: 10.1016/S0169-8095(96)00043-9.

Clark, A.J., S.J. Weiss, J.S. Kain, I.L. Jirak, M. Coniglio, Ch.J. Melick, Ch. Siewert, R.A. Sobash, P.T. Marsh, A.R. Dean, M. Xue, F. Kong, K.W. Thomas, Y. Wang, K. Brewster, J. Gao, X. Wang, J. Du, D.R. Novak, F.E. Barthold, M.J. Bodner, J.J. Levit, C.B. Entwistle, T.L. Jensen, and J. Correia Jr. (2012), An overview of the 2010 hazardous weather testbed experimental forecast program spring experiment, *Bull. Am. Meteorol. Soc.* **93**, 1, 55–74, DOI: 10.1175/BAMS-D-11-00040.1.

Dudhia, J. (1989), Numerical study of convection observed during the winter monsoon experiment using a mesoscale two-dimensional model, *J. Atmos. Sci.* **46**, 20, 3077–3107, DOI: 10.1175/1520-0469(1989)046<3077:NSOCOD>2.0.CO;2.

Dwyer, J.R. (2003), A fundamental limit on electric fields in air, *Geophys. Res. Lett.* **30**, 20, 2055, DOI: 10.1029/2003GL017781.

Fierro, A.O., E.R. Mansell, D.R. MacGorman, and C.L. Ziegler (2013), The implementation of an explicit charging and discharge lightning scheme within the WRF-ARW model: Benchmark simulations of a continental squall line, a tropical cyclone, and a winter storm, *Mon. Weather Rev.* **141**, 7, 2390–2415, DOI: 10.1175/MWR-D-12-00278.1.

Hong, S.Y., and J.O.J. Lim (2006), The WRF single-moment 6-class microphysics scheme (WSM6), *J. Korean Meteor. Soc.* **42**, 2, 129–151.

Iacono, M.J., J.S. Delamere, E.J. Mlawer, M.W. Shephard, S.A. Clough, and W.D. Collins (2008), Radiative forcing by long-lived greenhouse gases: Calculations with the AER radiative transfer models, *J. Geophys. Res.: Atmos.* **113**, D13, D13103, DOI: 10.1029/2008JD009944.

Janjic, Z.I. (1996), The surface layer in the NCEP Eta Model. **In:** *11th Conference on Numerical Weather Prediction, August 19–23, Norfolk, VA*, American Meteorological Society, Boston, 354–355.

Krzyścin, J.W., J. Guzikowski, A. Pietruczuk, and P.S. Sobolewski (2020), Improvement of the 24 hr forecast of surface UV radiation using an ensemble approach, *Meteorol. Appl.* **27**, 1, 1350–4827, DOI: 10.1002/met.1865.

Mansell, E.R., and C.L. Ziegler (2013), Aerosol effects on simulated storm electrification and precipitation in a two-moment bulk microphysics model, *J. Atmos. Sci.* **70**, 7, 2032–2050, DOI: 10.1175/JAS-D-12-0264.1.

Mansell, E.R., D.R. MacGorman, C.L. Ziegler, and J.M. Straka (2005), Charge structure and lightning sensitivity in a simulated multicell thunderstorm, *J. Geophys. Res.: Atmos.* **110**, D12, D12101, DOI: 10.1029/2004JD005287.

Mansell, E.R., C.L. Ziegler, and E.C. Bruning (2010), Simulated electrification of a small thunderstorm with two-moment bulk microphysics, *J. Atmos. Sci.* **67**, 1, 171–194, DOI: 10.1175/2009JAS2965.1.

NCAR (2020), National Centers for Environmental Prediction/National Weather Service/NOAA/U.S. Department of Commerce: NCEP/NCAR Global Reanalysis Products, 1948-continuing, Research Data Archive at the National Center for Atmospheric Research, Computational and Information Systems Laboratory, available from: https://rda.ucar.edu/datasets/ds090.0/ (accessed: 30 September 2020).

Pleim, J.E., and A. Xiu (1995), Development and testing of a surface flux and planetary boundary layer model for application in mesoscale models, *J. Appl. Meteorol*. **34**, 1, 16-32.

Pleim J.E., and A. Xiu (2003), Development of a land surface model. Part II: Data assimilation, *J. Appl. Meteorol. Climatol*. **42**, 12, 1811–1822, DOI: 10.1175/1520-0450(2003)042<1811:DOALSM>2.0.CO;2.

Tiedtke, M. (1989), A comprehensive mass flux scheme for cumulus parameterization in large-scale models, *Mon. Weather Rev*. **117**, 8, 1779–1800, DOI: 10.1175/1520-0493(1989)117<1779:ACMFSF>2.0.CO;2.

Ziegler, C.L., D.R. MacGorman, J.E. Dye, and P.S. Ray (1991), A model evaluation of noninductive graupel-ice charging in the early electrification of a mountain thunderstorm, *J. Geophys. Res.: Atmos*. **96**, D7, 12833–12855, DOI: 10.1029/91JD01246.

Received 16 September 2022
Received in revised form 28 December 2022
Accepted 31 December 2022

Publications of the Institute of Geophysics, Polish Academy of Sciences
Geophysical Data Bases, Processing and Instrumentation
vol. 442 (D-77), 2022, pp. 19-40
DOI: 10.25171/InstGeoph_PAS_Publs-2022-023

Nimbostratus and Stratus Cloud Atmospheric Electricity Database and Analysis Methods for the Project "Research Studies on the Electricity of Low-Level Layer Clouds for the Purpose of Developments in Global Atmospheric Circuit Modelling (ELLEC)"

Anna ODZIMEK[1,✉], Piotr BARAŃSKI[1], Marek KUBICKI[1], Danuta JASINKIEWICZ[1*],
Jerzy BERLIŃSKI[2*], and Wojciech GAJDA[3]

[1]Institute of Geophysics, Polish Academy of Sciences, Warszawa, Poland
[2]Faculty of Electronics and Information Technology, Warsaw University of Technology, Warszawa, Poland
[3]Institute of Meteorology and Water Management – National Research Institute, Warszawa, Poland
*retired
✉ aodzimek@igf.edu.pl

Abstract

This paper provides details on meteorological and atmospheric electricity datasets and the methodology of analysis of the atmospheric electric data from the Polish Atmospheric Electricity Observation Network used for the purpose of research studies of the electricity of Nimbostratus and Stratus clouds and their role in the global atmospheric electric circuit.

Keywords: atmospheric electricity, clouds, Nimbostratus, Stratus, global atmospheric electric circuit.

1. INTRODUCTION

The view that not only thunderclouds but also other electrified clouds, such as shower clouds, can generate electricity in the atmosphere has been originally formulated by Wilson (1921), the author of the concept of the global atmospheric electric circuit (GEC). Observations have been indicating that the electrical activity of low-level precipitation-producing clouds, such as Nimbostratus, is manifested by more complex electrical structure and generation of conduction and

---

precipitation electric currents (Chalmers 1956, 1958; Reiter 1965; Anderson 1966; Magono and Orikasa 1966; Rust and Trapp 2002). Imyanitov et al. particularly observed vertical profiles of the electric field through all kinds of clouds and investigated the profile properties dependent on the cloud genus and thickness, revealing the complex electrical structure of Nimbostratus clouds observed in situ (e.g., Imyanitov and Shifrin 1962; Imyanitov et al. 1974). Reiter (1968, 1972) investigated the electric field and current density under various types of precipitating clouds, including Nimbostratus, in particular during the transition between cloud genera and the absence or presence of precipitation. Based on these results, Odzimek et al. (2010) have constructed a GEC model assuming the low-level Nimbostratus cloud to be a generator in the circuit, in addition to the main convective cloud generator, resulting in a preliminary estimate of the "Nimbostratus" cloud contribution[1] at 20% to the total global current, subsequently revised to about 10% in Odzimek et al. (2018).

In 2011 a scientific project "Research studies on the Electricity of Low-Level Layer Clouds for the purpose of developments in global atmospheric circuit modelling (ELLEC)" has been proposed at the Institute of Geophysics, Polish Academy of Sciences (PAS), subsequently approved and funded by Poland National Science Center (NCN), in order to initiate a comprehensive study on the electricity of low-level layer clouds and their potential role in the global circuit. The project took advantage of the long-term ground-based observations of atmospheric electricity and meteorology, including clouds, at Stanisław Kalinowski Geophysical Observatory of the Institute of Geophysics (IG) PAS in Otwock-Świder, Poland, and, as a supplement, data from two Polish polar stations creating, together with Świder, the Polish Atmospheric Electricity Observation Network (Table 1). Characterised by a large surface area and continuous precipitation (Houze 1993), both Nimbostratus (Ns) and Stratus (St) cloud cases have been investigated. The first results of the project and a framework for future research have been presented in Odzimek et al. (2014), based on data from the years 2005–2013. Over the next two years, the data collection for the project have been extended till 2015, and Odzimek et al. (2018) presented the statistics of the occurrences of Nimbostratus and Stratus in Świder in 2005–2015 and the average values of main atmospheric electricity parameters over 2012–2015.

Table 1

Atmospheric electricity stations contributing to ELLEC project
(Polish Atmospheric Electricity Observation Network)

Observatory name, location, and operating institution	Short name	Period of Ns and St analysis	Geographical coordinates		
			Latitude	Longitude	Altitude
Stanisław Kalinowski Geophysical Observatory, Świder, Poland (IG PAS)	SWI	2005–2015	52.00°N	21.25°E	100 m
Stanisław Siedlecki Polish Polar Station, Hornsund, Svalbard, Norway (IG PAS)	HRN	2005–2015*	77.00°N	15.50°E	20 m
Henryk Arctowski Polish Antarctic Station, King George Island, New Shetland Islands, Antarctica (IBB PAS)	ARC	2013–2015**	62.16°S	58.47°W	20 m

*only 2007–2010 analysed so far in Odzimek et al. (2014),
**not yet fully analysed.

---

[1] Not to be equated with the electrified shower cloud generator (e.g., Liu et al. 2010).

As the work on the various aspects of electricity of Ns and St clouds based on the archived data is in progress, in this paper we present the details of the cloud and atmospheric electricity database that has been created for the purpose of the project. The structure of the database is the subject of the next section (Section 2), and in another section (Section 3) we describe the details of the atmospheric electricity measurements and methodology behind the analysis performed on the atmospheric electricity data presented in Odzimek et al. (2018), and still applied in the current studies.

2. ATMOSPHERIC ELECTRICITY AND CLOUD DATASET

The ELLEC project database has been so far created mostly from the data gathered at the Geophysical Observatory of the Institute of Geophysics PAS in Świder, Poland (51.15°N, 21.23°E), taking advantage of the meteorological observations contributing to advanced atmospheric electricity monitoring present at the Observatory for several decades (Dziembowska 2009). Atmospheric electricity data from the other Institute – run atmospheric electricity station in Stanisław Siedlecki Polish Polar Station in Hornsund, Svalbard, Norway (77.00°N, 15.50°E) also contributed to the database of cloud cases. In addition, new electric field measurements have been set up and conducted in 2013–2015 at the Institute of Biochemistry and Biophysics (IBB) PAS Henryk Arctowski Polish Antarctic Station in King George Island, New Shetland Islands, Antarctica (62.16°S, 58.47°W), at the same time financed by another NCN grant project (Kubicki et al. 2016). At Hornsund, standard meteorological cloud observations are performed continuously (e.g., Matuszko and Soroka 2013). Therefore, the database has been relatively easily extended by cases from this polar station. An occurrence statistics of Ns and St clouds observed at Hornsund based on the 2007–2010 data has been already presented in Odzimek et al. (2014) and an analysis of the full period is a subject of future publication. Observations at the Arctowski Station were at the time very limited in this respect but some additional observations during and shortly after the project have been requested to be made by the expedition geophysicists conducting atmospheric electricity measurements. The lack of systematic meteorological observations at Arctowski limits the selection of relevant cases from the station, but overall the additional cases provide opportunities for an insight into latitudinal effects in the performed study – since the Świder observations can rather be representative of land and suburban, mid-latitude cases, and the global circuit modelling requires cloud models covering all latitudes.

2.1 Meteorological observations

Meteorological observations are continuously performed at Świder in order to monitor fair weather conditions necessary for the qualification of atmospheric electricity data. The observatory keeps records of standard meteorological parameters, cloud condensation nuclei concentrations, and the intensity and time of onset and ending of precipitation as well as the type and amount of cloud cover (cloudiness). Clouds are observed by visual observations by an observer, with a resolution of 1 hour. The cloud species or varieties are not recorded. More recently all-sky recordings with a colour camera have been used to support the observations, together with a Vaisala CL-31 ceilometer funded by the ELLEC project. The duration of rain, drizzle, and snow and their intensity are estimated from the recordings using a Vaisala Rain Detector DRD11A device, in addition to a standard (Hellmann) rain gauge of the observatory and the SEBA Hydrometrie RG-50 heated rain gauge of the Institute of Meteorology and Water Management – National Research Institute, measuring at Świder usually from spring to autumn. The latter allows estimating the rate of precipitation in mm per time unit. At Hornsund the observations of precipitation have been partly supported by OTT Messtechnik Parsivel weather sensor. Details of the instruments and related observed meteorological variables which are analysed in the project are summarised in Table 2.

Table 2

Summary of supporting meteorological observations

Element	Variables	Observations	Instrumentation	Unit	Range	Station
clouds	cloudiness genus	visual	–	1	0–9	SWI HRN ARC
		technical	all sky camera			SWI
	base altitude	technical	VAISALA ceilometer CL-31	m	0–7600	SWI
precipitation	type and duration	visual	–			SWI HRN ARC
		technical	VAISALA DRD11A Rain Detector OTT Parsivel	min	>= 1 min type recognition supported also by air temperature records	SWI HRN
	intensity	visual	-	1	0–2	SWI HRN ARC
		technical	VAISALA DRD11A rain detector SEBA RG-50 rain gauge OTT Parsivel	arbitrary units 0.1 mm		SWI HRN

2.2 The cloud database

The project's cloud database is based on the observatories' monthly reports of meteorological observations. For the analysis, the information retrieved from the reports on clouds, precipitation, mainly rain, snow, drizzle, granular snow, and other phenomena, e.g., mist, fog, hoar frost, etc., has been stored in binary files whose record variable structure is described in detail in Table 3. Files are named in relation to days of the year in the year-month-day digit format "YYYYMMDD" (YYYY – 4 digits for year, MM – 2 digits for the month of the year, and DD – 2 digits for the day of the month), preceded by the affix "pog" and followed by the station short abbreviation "STN" (SWI for the Świder Observatory, HRN for Hornsund Station, and ARC for Arctowski Station), separated by "_", and with the file extension ".dat". The variables encoded in the binary file created a digital record type consisting of three main fields: the date, clouds record, and phenomena record. The clouds record is also a record type variable of numbers and tables of numbers (integer and double real values), each encoding selected characteristics such as the number of cloud cases which have been observed on the day, the clouds genera, species and varieties, the cloud onset and end time for each genus (resolution of 1 h resulting from the time observations at Świder, 3 h for Hornsund), sky cover (cloudiness) in okta scale (0–8, 9 – sky not visible) by the cloud genus at the time of onset and the end time, and a special flag for the times, encoded by 0 or 1 or 2, meaning: 0 – time from observations at an hour, 1 – approximate hour of onset or end, 2 – time determined only by the climatological times: n, na, a, p, np (e.g., Chomicz 1962). Atmospheric precipitation and other types of meteorological phenomena have also been encoded in a similar way. The digit (integer) codes for cloud genera, species and variety, and phenomena types are outlined in the Appendix.

As an example we present the record for the day 24 May 2013, when St and Ns cases occurred (Odzimek et al. 2018, Figs. 9–10). Below we show the transcription of the record in symbols denoting variables from Table 3 and expressions used in the written language:

Table 3

Daily cloud dataset encoded into binary file “pog_date(YYYYMMDD)_STN.dat”

Variable	Type	Name*	Values or value range
	record Tpog	pog	record
Structure of daily record Tpog			
date	double	pog.d	date-time value**
clouds record	record Tcl	pog.c	record
phenomena record	record Tph	pog.p	record
Structure of clouds record Tcl			
number of cloud cases	integer	pog.c.count	0-10
table of cloud cases	table of Tcl1	pog.c.tab	indexed table
Structure of cloud record Tcl1			
cloud genus	integer	pog.c.tab[index].typ	see Appendix
cloud species and variety***	set of integer	pog.c.tab[index].gat	see Appendix
cloud time onset	double	pog.c.tab[index].t1	date-time value**
cloud time end	double	pog.c.tab[index].t2	date-time value**
cloud time onset flag	integer	pog.c.tab[index].f1	0, 1, 2
cloud time end flag	integer	pog.c.tab[index].f2	0, 1, 2
cloudiness at the cloud time onset	integer	pog.c.tab[index].c1	0-9
cloudiness at the cloud time end	integer	pog.c.tab[index].c2	0-9
Structure of phenomena record Tph			
number of phenomena	integer	pog.p.count	0-15
table of phenomena cases	table of Tph1	pog.p.tab	indexed table
Structure of phenomenon record Tph1			
phenomenon type	integer	pog.p.tab[index].typ	see Appendix
phenomenon time onset	double	pog.p.tab[index].t1	date-time value**
phenomenon time end	double	pog.p.tab[index].t2	date-time value**
phenomenon time onset flag	integer	pog.p.tab[index].f1	0, 1, 2
phenomenon time end flag	integer	pog.p tab[index].f2	0, 1, 2
phenomenon intensity at its onset	integer	pog.p.tab[index].z1	0-2
phenomenon intensity at its end	integer	pog.p.tab[index].z2	0-2

*suggested name to give an example of the variable reference in the computer code,
**double value such as 0.0 refers to 12/30/1899 12:00 am (as in Delphi programming language),
***only for the dataset of clouds observed at Hornsund (HRN).

Transcription of variable “pog” for 13 May 2013
Date: 2013/05/13
Cloud record:
Number of cloud cases: 2
Cloud 1: St, 2015/04/24 00:00 – 2015/04/24 09:00, flags: (0,0), cloudiness: 8-8
Cloud 2: Ns, 2015/04/24 09:00 – 2015/04/25 00:00, flags: (0,0), cloudiness: 8-8
Phenomena record:
Number of phenomena: 4
Phenomenon 1: Intermittent drizzle, 2013/05/24 01:11 – 2013/05/24 01:14, flags: (0,0), intensity: 0-0
Phenomenon 2: Drizzle, 2013/05/24 01:35 – 2013/05/24 01:56, (0,0), 0-0
Phenomenon 3: Drizzle, 2013/05/24 06:55 – 2013/05/24 09:20, (0,0), 0-0
Phenomenon 4: Rain, 2013/05/24 09:20 – 2013/05/25 00:00, (0,0), 0-2

2.3 Atmospheric electricity database

The atmospheric electricity part of the database includes results of measurements of the atmospheric electricity parameters at a station for the days with cloud events. Data are stored in the text format of a less complicated structure compared to the cloud dataset. The atmospheric electricity parameters measured at Świder are:

- vertical (z) component of the strength of the atmospheric electric field – later in the text called the electric field (measured by two independent sensors, one of which, the collector, measures actually the electric potential gradient),
- vertical (z) component of the strength of the atmospheric electric current density – later in the text called the electric current density,
- positive air conductivity,
- negative air conductivity.

For the purpose of most analyses, the parameters are stored into daily files of 1-minute average values, tabulated, and written in a text format. In one file there are 1440 tabulated values for each atmospheric electricity parameter that is available for the day, preceded by “one minute” introductory text informing about the time resolution and, in the following line, names of the variables in each column. The first column denotes the number of a sample (0..1439). The next columns are atmospheric parameter values, as listed in Table 4. Any missing value is denoted by “*”. The parameters includes atmospheric electric field (at Świder measured by two methods hence two data columns, see next section), atmospheric electric current density, and positive and negative air conductivity as numbers in units as shown in Table 4. The methods of how these parameters are measured and analysed for the purpose of the ELLEC project are described in Section 3. Additionally, in the first half of 2012, short-term measurements of the electric charge on droplets (e.g., Imyanitov 1957) have been performed on several occasions; however, these measurements have been abandoned due to a difficult interpretation of the data from the rarely used instrument.

Sign convention. The convention for the sign of the atmospheric electric field and current density used here is the so-called “fair-weather convention”, i.e., the *z* axis is directed downwards). In fair-weather conditions, the atmospheric electric field is directed downwards and in this convention considered positive. This also means the sign and value of the E_z is the same as that of the electric potential gradient. In regard to the atmospheric electric current density, positive charge transferred downwards (in the direction of fair-weather electric field) becomes positive atmospheric electric current.

Table 4

Daily atmospheric electricity datasets in output text files “date(YYYYMMDD)_STN.dat”*

Variable	Type	Name*	Unit	Range
negative air conductivity	real	cond–	fS/m	0.1–12.0
positive air conductivity	real	cond+	fS/m	0.1–12.0
vertical component of the atmospheric current density	real	J_z	pA/m^2	±20.0
vertical component of the strength of the atmospheric electric field (collector)	integer	Ez(COL)	V/m	±1390 V/m ±4960 V/m (since December 2012)
vertical component of the strength of the atmospheric electric field (field mill)	integer	Ez(FM)	V/m	±1390 V/m ±13.9 kV/m (since May 2013)**

*In the case of data from Hornsund (HRN) or Arctowski (ARC) where only the electric field is measured the columns with remaining variables in the file can be absent,
**Świder (SWI) only.

2.4 Auxiliary radar, satellite, and sounding data

In addition to the ceilometer observations at Świder, we have also obtained for the purpose of the project the meteorological radar, cloud satellite product data, and atmospheric sounding data (Figs. 1 and 2). These are auxiliary data so far used mainly in case studies. The atmospheric sounding data, both in the text and in graphical format such as the skew-T diagrams, have been downloaded from the University of Wyoming web pages at http://weather.uwyo.edu/upperair/sounding.html, for Legionowo (approximately 30 km NNW of Świder). Radar and satellite data have been processed at the Institute of Meteorology and Water Management – National Research Institute (IMWM-NRI) for the purpose of the ELLEC grant project. These datasets cover the selected Ns and St cases from 2012 to mid-2013 (Odzimek et al. 2017a,b).

The radar data come from ground-based meteorological radar observations at Legionowo and include products based on the radar volumetric data for both the classical scan with a range of 250 km, and the Doppler scan with a range of 125 km. As the area of special interest has been defined around the Świder Geophysical Observatory, all products had a range of 100 km (Gajda 2013). Types of generated products include:

- EHT radar echo height (range: 100 km, reflectivity threshold: –5 dBZ);
- EHT radar echo height (range: 100 km, reflectivity threshold: 0 dBZ);
- EHT radar echo height (range: 100 km, reflectivity threshold: 4 dBZ);
- PCAPPI reflectivity at a given altitude (range: 100 km, altitude: 1 km);
- PCAPPI reflectivity at a given altitude (range: 100 km, altitude: 2 km);
- PCAPPI reflectivity at a given altitude (range: 100 km, altitude: 3 km);
- VCUT vertical section for three variants:
  – along the radar beam towards the Świder station (1),
  – north-south direction passing through the Świder station (2),
  – east-west direction passing through the Świder station (3).

The satellite products are based on SEVIRI instrument data from the EUMETSAT Meteosat satellites and present a „cloud type” CT product at 15-min time resolution in the form of graphical information stored in .gif format images (Fig. 2) with an option of access to digital

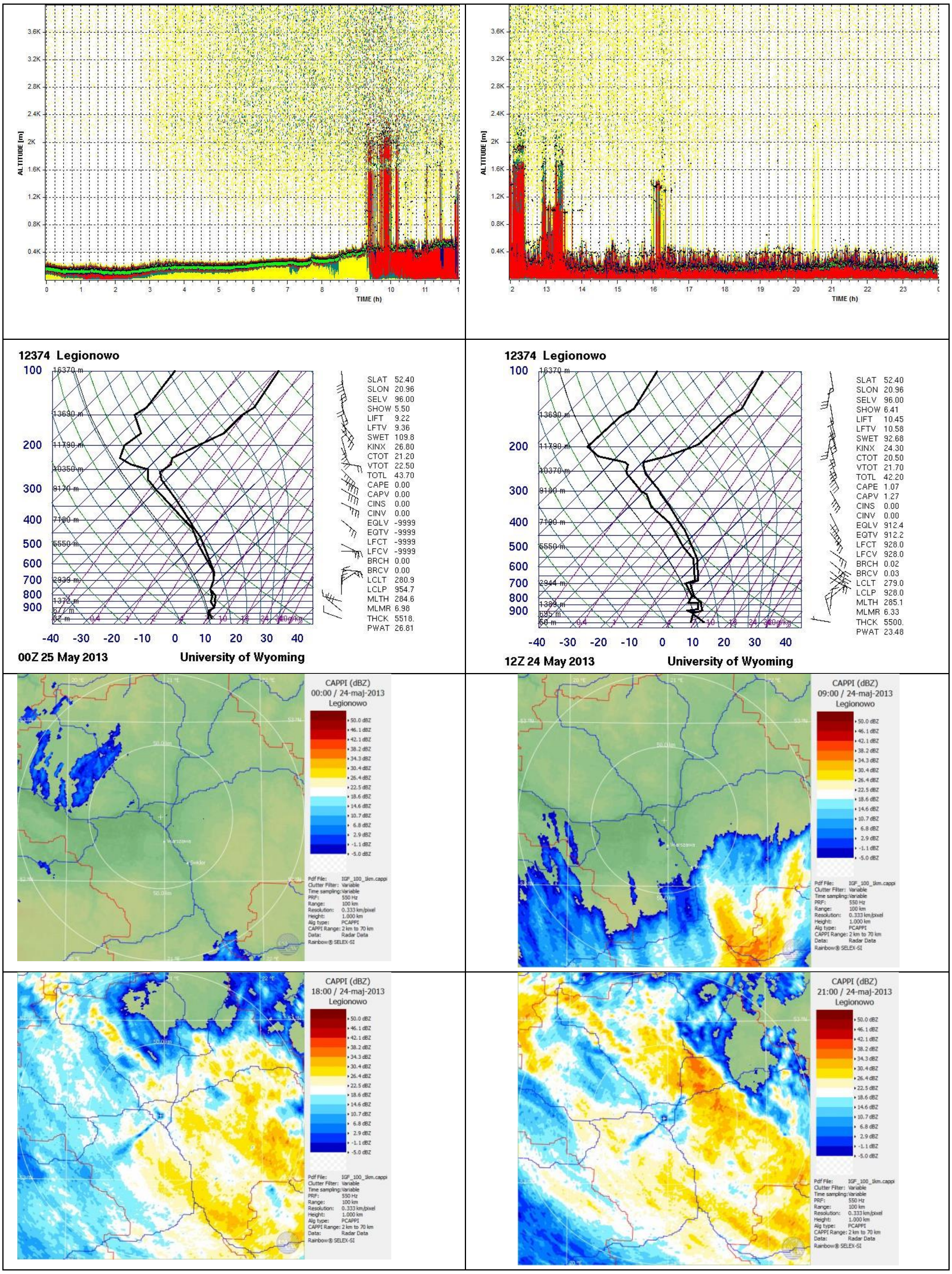

Fig. 1. Selected auxiliary data for 24 May 2013 during an occurrence of St with short drizzle and an Ns cloud with rain: left panel – 00–12 UT, right panel – 12–24 UT, upper panels: ceilometer reflectivity plots from the CL30 ceilometer, middle panels: skew-T diagrams for Legionowo soundings at 0 UT and 12 UT, four bottom panels: Legionowo radar reflectivity (1 km CAPPI) at 00, 09, 12, 21 UT.

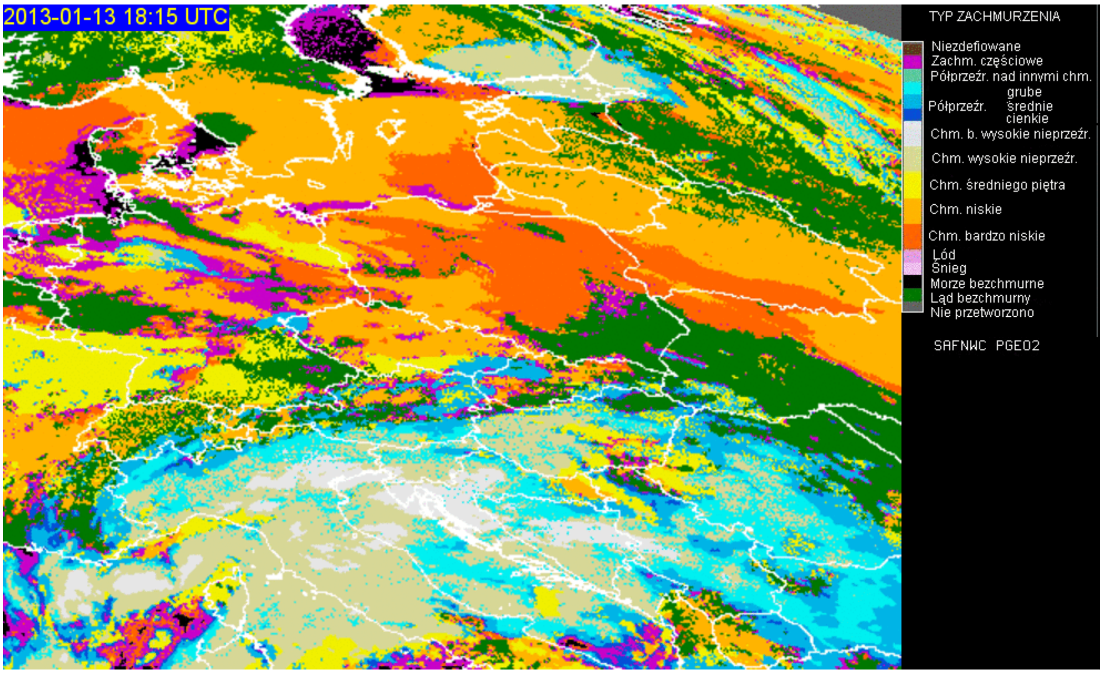

Fig. 2. An example of the EUMETSAT/NWCSAF-IMWM satellite cloud type product from 13 January 2013, 18:15 UTC. The legend on the right side lists possible features (types) of clouds and the cloudiness at the earth surface, as follows: brown – undefined; amaranth – partly cloudy; light green – translucent over other clouds; light-blue, blue, navy – translucent thick, medium, thin; yellow – middle-level clouds; dark yellow – low-level clouds; orange – very low clouds; pink – ice; light pink – snow; black – sea; green – cloudless land; dark grey – not processed.

output in other data formats. The spatial resolution is ~12 km. These data help to confirm the existence of relevant cloud types, and allow calculation of their surface area (Serafin-Rek 2013).

Ceilometer data have been stored in the graphical form as produced from the ceilometer commercial software CL-View, and they present the level of reflectivity and software-calculated values of the cloud base altitude. The images help for example to distinguish a Stratocumulus decay and the formation of Ns or St. During Ns or St with precipitation, the ceilometer allows only the determination of the height of the cloud base. The standard software-produced files which store information on the height of clouds' base in text form have also been preserved and used.

These auxiliary data helped to confirm the existence of low stratiform clouds and precipitation from the clouds at Świder as well as to deliver information on some spatial structure of the precipitation both in the horizontal and vertical direction.

3. ATMOSPHERIC ELECTRICITY MEASUREMENTS AND DATA ANALYSIS

3.1 Measurements

Descriptions of the apparatus used for the measurements of the electric field and conductivity at Świder station have been included in the yearly reports of the results of observations (e.g., Kubicki 2006). Below we enclose the schematic diagrams of the measurement set-up based on the reports.

The electric field strength at Świder station is measured with a radioactive collector method (Witkowski 1902) – these are values annotated in data files by "Ez(COL)", or by a rotating dipole-type field mill – values annotated in the data files by "Ez(FM)". At Hornsund a collector has also been in use but much more reliable measurements are performed simultaneously using a rotating dipole-type field mill constructed by Berliński et al. (2007). A rotating-dipole field mill of this type has also been used at Arctowski Station in 2013–2015. A schematic diagram of the measurement with the collector (K) is shown in Fig. 3a. The radioactive collector (K) at Świder has a radioactive source of 30 μC activity (Am). The collector is connected to an electrometer constructed in the observatory (e.g., Kubicki 2006), placed inside a metal case at 200 m above the ground level, mounted on a metal pipe. The electrometer has high input resistance $R_{\mathrm{in}} = 10^{14}\ \Omega$, compared with the collector's resistance $R_{\mathrm{coll}} = 7 \times 10^{10}\ \Omega$. Such use of resistances in the circuit eliminates the influence of wind on the electric field measurements. The time constant of the current circuit, including the capacitance of cables, is 7 s.

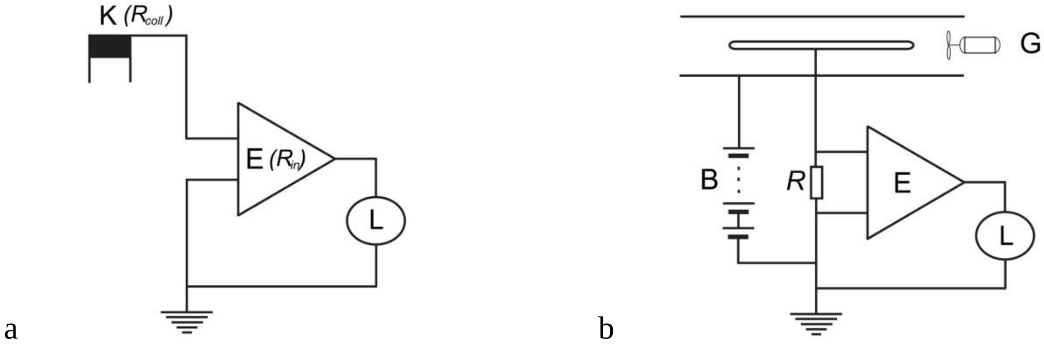

Fig. 3. Schematic diagram for electric field and conductivity measurements at the Geophysical Observatory in Świder (after Kubicki 2006). Apparatus: K – radioactive collector, G – Gerdien tube, L – logger, B – batteries, E – electrometer (of R_{in} input resistance), R_{coll} – collector resistance, R – other resistances (description in the text).

The conductivity is measured with a Gerdien tube (G), also called the Gerdien aspiration condenser (Gerdien 1905), the schematic diagram of which is shown in Fig 3b. It is placed in a hut 1 m above the ground level. One side of the tube is outside of the hut where the air is aspirated. The boundary mobility of the condenser is $2.6 \times 10^{-4}\ \mathrm{m^2/Vs}$. The outer electrode is connected to a series of batteries (B). The centre electrode of the tube is connected via a high resistance $R = 100\ \mathrm{G\Omega}$ to a Keithley 614 electrometer (E), which measures the current flowing through the resistance R, which is proportional to the conductivity of the air in the tube. The time constant of the circuit is 60 s. There are two separate tubes for the measurements of positive and negative ion polarities.

Analog data are transformed into digital using an Institute-developed data loggers (L) with an analog-to-digital converter and output data stored in .ddf format (e.g., Reda and Neska 2016). A file in a .ddf format is a text file describing the number of channels and time series in each data channel (start time, time shift, resolution, base value, name, units, etc.) and associated files for each channel in binary format. The sampling is usually set to 1 s time resolution. After upload to a data server, the data are numerically averaged to 1-minute values available on a password-protected WWW-based interface for visual inspection in 24-hour data plots, and for download.

Some atmospheric current density measurements from Świder have been available from 2005–2007, in part conducted for the study of fair-weather atmospheric electric convection current, and over 2011–2012 have been restarted as the station measurements of the atmospheric current density J_z. A block diagram of the atmospheric current measurement set-up is shown in Fig. 4. The sensor for the current density measurements is a "Wilson antenna" type (Wilson 1906), i.e., metal (aluminum) flat plate supported by isolators and levelled with the ground. The antenna is of a circular shape of a surface area of $0.5\ \mathrm{m}^2$. The antenna is

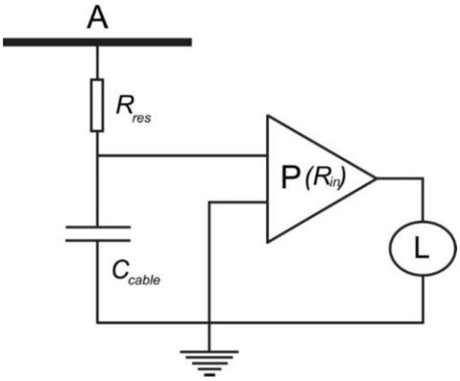

Fig. 4. Schematic diagram of the atmospheric current density measurement at the Geophysical Observatory in Świder. Apparatus: A – metal flat antenna, L – logger, P – picoammeter (of R_{in} input resistance), C_{cable} – cable capacitance, R_{res} – added resistance (description in the text).

connected to a Keithley 867 picoammeter (P) in series with a 10^{11} Ω resistor R_{res}. A cable from the antenna to the picoammeter in the building (300 m) has an estimated capacitance $C_{cable} = 300$ pF (1000 pF in other configurations used before 2012). The role of the $R_{res} = 10^{11}$ Ω resistance is to limit the amplitude of the displacement current received by the antenna. A numerical simulation of the schematics with the OrCAD PSpice A/D, an electronic circuit simulation software, has indicated that the average amplitude of the input signal decreased approximately to 0.8 of the input level. Therefore, the output values of the current have been multiplied by 1/0.8 = 1.25.

In general, such antenna detects all components of the atmospheric Maxwell current which includes conduction, precipitation, convection, corona, lightning, and the displacement current (e.g., MacGorman and Rust 1998, Chapter 1). In regard to the conduction component received by the antenna, it is important to take into account that it measures only part of the conduction current, that is carried by the ions which are able to reach the antenna in the direction of the electric field – this means they are the ions of an electric charge sign the same as the sign of the electric field. In the case of other components where electric charge is transferred gravitationally or mechanically, components of both signs are received.

3.2 Data analysis

Our study of the electricity of clouds from ground-level atmospheric electricity measurements is based on the analysis of the electric field, conductivity, and current density components which participate in the charge transfer in the air between the cloud and the ground. A similar approach was used by, e.g., Aspinall (1969). Because the considered cloud data span a larger period of time we have used only the electric field data measured by the radioactive collector method, i.e., the E_z values from the Ez(COL) records. As mentioned, the total Maxwell current density in the atmosphere consists of several components characteristic of the way of charge transfer in the process, e.g., conduction, lightning, or corona. In case of Stratus and isolated Nimbostratus, i.e., not in connection with a thunderstorm system such as the mesoscale convective system (Michnowski et al. 1987; Houze 1993), we assume that lightning, and related to it lightning current density component, is usually absent (this can also be confirmed by meteorological observations and is monitored in the electric field signal). We also neglect corona current density effects, taking into account that we work in a sufficiently low electric field range. The remaining current density components of the Maxwell current density J_M (Eq. 1) that are required to be taken into account are:

- vertical conduction field component J_E (in other publications denoted J_C), according to Ohm law equal to the product of air conductivity and the electric field strength E_z (Eq. 2);

- precipitation or convection current J_{PC} (in general representing the charge transfer by various mechanical processes, and not by conduction);
- the displacement current J_D, theoretically expressed by the time derivative of the electric field multiplied by the dielectric permittivity of free space $\varepsilon_0 = 8.854 \times 10^{12}$ F/m (Eq. 3).

$$J_M = J_E + J_{PC} + J_D = J_T \ , \tag{1}$$

$$J_E = (\lambda_+ + \lambda_-)\, E_z = \lambda\, E_z \ , \tag{2}$$

$$J_D = \varepsilon_0\, \partial E_z/\partial t \ , \tag{3}$$

$$J_T = J_E + J_{PC} \ . \tag{4}$$

After separating the displacement current density from the Maxwell current we obtain the current density component J_T (total) (Eq. 4), referring to the current density due to the total charge transfer under the cloud to the ground (Chalmers 1958). The total current J_T takes into account the charge transferred by both the conduction and precipitation or convection. These three current components, J_E, J_{PC}, and their sum J_T, are the major parameters we study. In the next paragraph, we describe how we determine these current density components from the ground-based atmospheric electricity measurements at Świder. The method has already been used in Odzimek et al. (2018) and would also be applied in future work.

In the analysis of the atmospheric electricity, we use 5-minute average values of the electric parameters which we calculate from already averaged 1-min text atmospheric electricity data. We therefore can rewrite the Eqs. 1–4 for the average values:

$$\langle J_M \rangle = \langle J_E \rangle + \langle J_{PC} \rangle + \langle J_D \rangle = \langle J_T \rangle + \langle J_D \rangle \ , \tag{5}$$

$$\langle J_E \rangle = \langle \lambda\, E_z \rangle \ , \tag{6}$$

$$\langle J_D \rangle = \langle \varepsilon_0\, \partial E_z/\partial t \rangle \cong 0 \ , \tag{7}$$

$$\langle J_T \rangle = \langle J_E \rangle + \langle J_{PC} \rangle \ . \tag{8}$$

Taking into account, that the displacement current component is reduced both by the current measurement set-up and by the time averaging of the 1-min data, we further assume that in the 5-min averages this component is negligible.

Conduction current J_E

The conduction current density J_E is determined from the Ohm law that relates the conduction current density to the total conductivity λ (the sum of the unipolar conductivities λ_+ and λ_-) multiplied by the electric field, E_z (Eq. 2). According to this definition, the sign of the component is in agreement with the sign convention for the electric field (transport of positive charge downwards is positive).

Precipitation-convection current J_{PC}

As indicated above, in theory, by subtracting from the Maxwell current density the values of the two other components, i.e., the displacement current J_D and conduction current J_E, both possible to be determined from the direct measurements of the electric field, E_z, and the conductivity, λ, we are able to evaluate the precipitation component J_{PC}. When measuring the Maxwell current density by the Wilson antenna, one should take into account in the subtraction only the polarity which agrees with the direction of the electric field, $J_{\lambda(E)}$:

$$J_{PC} = J_z - J_{\lambda(E)} \ , \tag{9}$$

$$J_{\lambda(E)} = \lambda_+ \; E_z \quad \text{if} \quad E_z > 0 \ , \tag{10}$$

$$J_{\lambda(E)} = \lambda_- \; E_z \quad \text{if} \quad E_z < 0 \ , \tag{11}$$

where J_z is the measured Maxwell current density, $J_{\lambda(E)}$ is the conduction current component related to the electric field and unipolar conductivity in agreement with the sign of the electric field, i.e., $J_{\lambda(E)} = \lambda_+ E_z$ when $E_z > 0$ or $J_{\lambda(E)} = \lambda_- E_z$ when $E_z < 0$.

The final set of equations for the determination of the current density components from measurements is:

$$<J_E> = <\lambda \, E_z> = < (\lambda_+ + \lambda_-) \, E_z> \ , \tag{12}$$

$$<J_{PC}> = <J_z> - <J_{\lambda(E)}> \ , \tag{13}$$

$$<J_T> = <J_E> + <J_{PC}> \ . \tag{14}$$

The above scheme of calculations has been used with the measurements collected for the purpose of the ELLEC project over 2012–2015. However, for a short period of time the measurements of the current density were performed with a screened antenna. The aim of this experiment was to measure the precipitation-convection current density J_{PC} directly. Such a measurement was arranged by covering the Maxwell current density sensor by a grounded cuboid metal mesh, made of 2 mm metal wire, mesh size 4 cm by 4 cm, with four rectangular sides and a square surface area of 1 m^2 placed 40 cm above the antenna level (Odzimek et al. 2018, Fig. 4). We have temporarily conducted such measurements over approximately one month in the spring of 2013 (May/June). The antenna surface area covered by the mesh was ≅4.4% of its total surface area. The screened antenna, in an ideal situation, should not receive the conduction current and other field-dependent current components, thus detecting only the current of the charge transferred by precipitation or convection. Monitoring the sign and value of J_{PC} component gives a possibility to evaluate the total amount of electric charge deposited on the ground by precipitation particles descending from different types of electrified clouds or the charged particles carried by convection. Although in the past other methods of measurement of the precipitation current have been used (Imyanitov 1957), the method of measurements using an antenna has also been in use (e.g., Ramsay and Chalmers 1960; Aspinall 1969). Unfortunately, it was impossible at the time of the project to conduct simultaneous measurements with exposed and screened antenna. Such an experiment would be very valuable for comparison and validation of results.

In the measurement set-up with the screened antenna, we equate the measured current J_z with the precipitation-convection current J_{PC}, and the calculations scheme for this period becomes as follows:

$$<J_z> = <J_{PC}> \ , \tag{15}$$

$$<J_E> = <\lambda \, E_z> = < (\lambda_+ + \lambda_-) \, E_z> \ , \tag{16}$$

$$<J_{T>} = <J_E> + <J_{PC}> \ . \tag{17}$$

Below we show some examples of the time series of the current components measured and derived in the way described above. The first is an example of a rain episode from 3 October 2012 in Fig. 5, and the second with a snowfall on 20 January 2015 in Fig. 6. These two examples are characterised by relatively small amplitudes of the electric field, $|E_z| < 1000$ V/m, and small variations of the conductivities. The other case with drizzle and rain is from 24 May 2013. In this case, the current antenna was screened. This is a case with rather high (negative) values of the electric field, as is the case with another snowfall event on 27 October 2012 (mostly positive

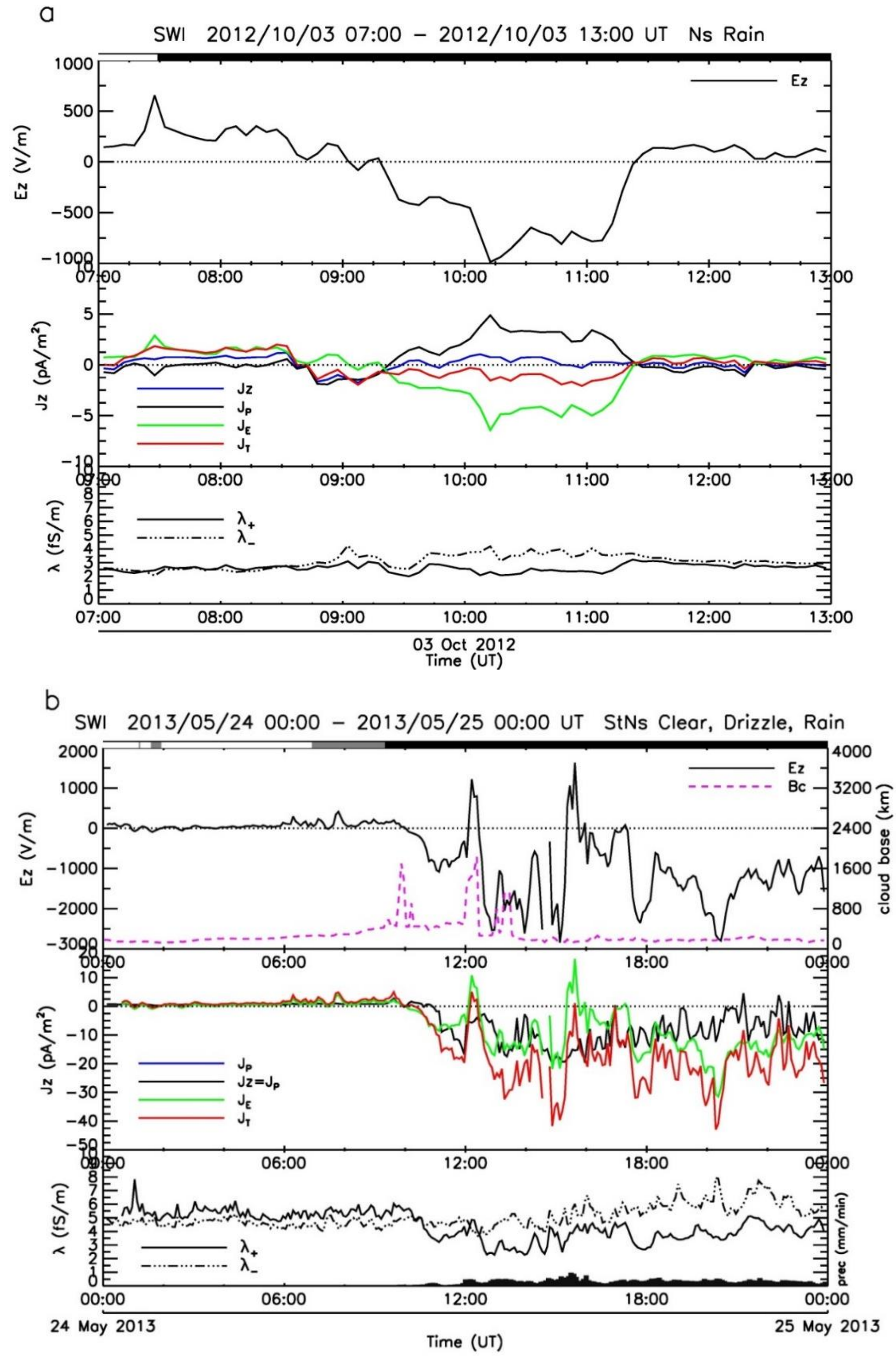

Fig. 5. Time series of 5-min average values of the electric field, current density, and air conductivity under Stratus and raining Nimbostratus clouds at Świder on: (a) 3 October 2013, 00:00–13:00 UT, Ns; (b) 24–25 May 2013, 00:00–00:00 UT, St till ~9:00 UT, then Ns. Upper panel – the electric field (E_z), cloud base (B_c) as determined by the ceilometer – when available; middle panel – variations of the measured and calculated components of vertical ground-level current density, i.e., the measured J_z component, precipitation current density J_{PC}, conduction current density J_E, and total current density J_T, bottom panel – positive and negative air conductivity. In cases (a) J_{PC} was calculated and in case (b) measured. Periods of precipitation are indicated by the coloured stripes above the upper panel: black for rain, and grey for periods of drizzle. In the bottom panel of (b) plotted are 5-min averaged G-50 rain gauge precipitation rates.

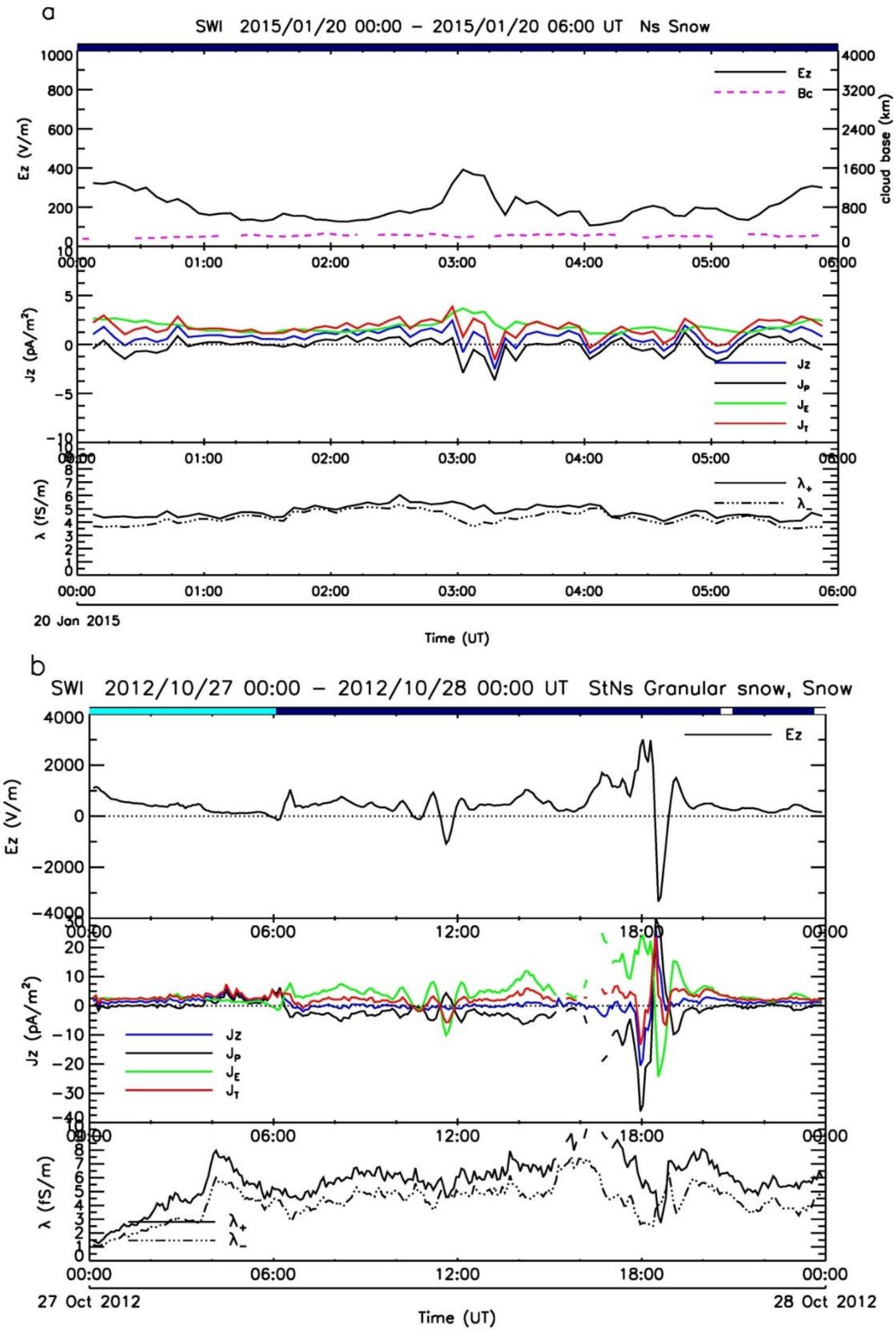

Fig. 6. Time series of 5-min average values of the electric field, current density, and air conductivity under snowing Stratus and Nimbostratus clouds at Świder on: (a) 20 January 2015, 00:00–06:00 UT, Ns; (b) 27–28 October 2012, 00:00–00:00 UT, St followed by Ns at ~6:00 UT. Upper panel – electric field (E_z), and cloud base (B_c) as determined by the ceilometer – when available; middle panel – time variations of the measured and calculated components of vertical ground-level current density, i.e., the measured J_z component, precipitation current density J_{PC}, conduction current density J_E, and total current density J_T, bottom panel – positive and negative air conductivity. In both cases, (a) and (b), J_{PC} component was calculated. Periods of precipitation are indicated by the coloured stripes above the upper panel: navy for snow, and turquoise for periods of granular snow.

but not so stable, e.g., Reiter has determined the stability conditions by the number of the field reversals per hour). The electric field during stable rainfall almost always gets and remains negative, as is the case in the first example, while during snowfall the field stays mostly positive (see, e.g., Odzimek et al. 2018). Note that the total current J_T during snow is mostly positive (i.e., downward, as in fair weather) and during rain it can become negative (i.e., upward). This has consequences for the charging of the global atmospheric electric circuit which we investigated in other publications.

Error analysis

The calculated values of the current density components have inevitably large errors since in addition to the measurement error (5–10% of the value, depending on the variable) there are large deviations related to averaging the values which can strongly vary in time. In such a case, often the median value and interquartile range are used as representative of average values and its error but we rather use an average mean value which seems more appropriate and also used by other researchers. The standard deviation of the mean is always relatively high due to the large time variability of the detected signals (up to 55%). In Table 5 we give a summary of the percentage errors.

Table 5

Summary of percentage errors of the electric measurements and calculated average mean values

Variable		Measurement error	Averages	Standard deviation of 5-min average value
E_z	100 V/m	5%	$<E_z>$	50%
λ_+, λ_-	5 fS/m	10%	$<\lambda_+>$	20%
J_z	5 pA/m^2	10%	$<J_z>$	50%

4. DATA AVAILABILITY

Datasets described in the paper are at present available on demand from the ELLEC project principal investigator Anna Odzimek (aodzimek@igf.edu.pl). The electric and cloud data will be submitted to the Institute of Geophysics PAS Data Portal at ELLEC-dedicated website https://dataportal.igf.edu.pl/group/ellec. Links to already created open-access datasets on Ns and St events from Świder, originally submitted to RePOD ICM UW repository, were added in 2021. More data and metadata of relevant datasets will be subsequently added, however, the binary files of cloud records are to be converted to open file formats and similar data structures. In regard to the ELLEC radar and satellite data, there are terms and conditions of reuse for other purposes as determined by the IMWM-NRI – IG PAS agreement concluded with the data order; more information can be obtained from the PI.

Figure 7 summarises the availability of each kind of data of the project, for the dates with cases of Ns and St clouds at Świder – 711 of individual Ns, St, or mixed St-Ns cases-dates of duration 4113 hours in total for years 2012–2015. These are the data that since mid-2012 could potentially be used for the full analysis that is presented in Section 3 (data from Hornsund and Arctowski do not present this opportunity since only the electric field is recorded). The existence of relevant data is indicated by the grey-coloured stripes: starting from the bottom: the described above “pog” cloud information files (Table 1), i.e., the basic 100%, auxiliary data files for the atmospheric sounding profiles from Legionowo at the term closest to the beginning of a case (00 or 12 UT) – usually of high availability where the atmospheric soundings are regular, the set of electric data (Table 3) for at least 50% duration of the case, necessary to

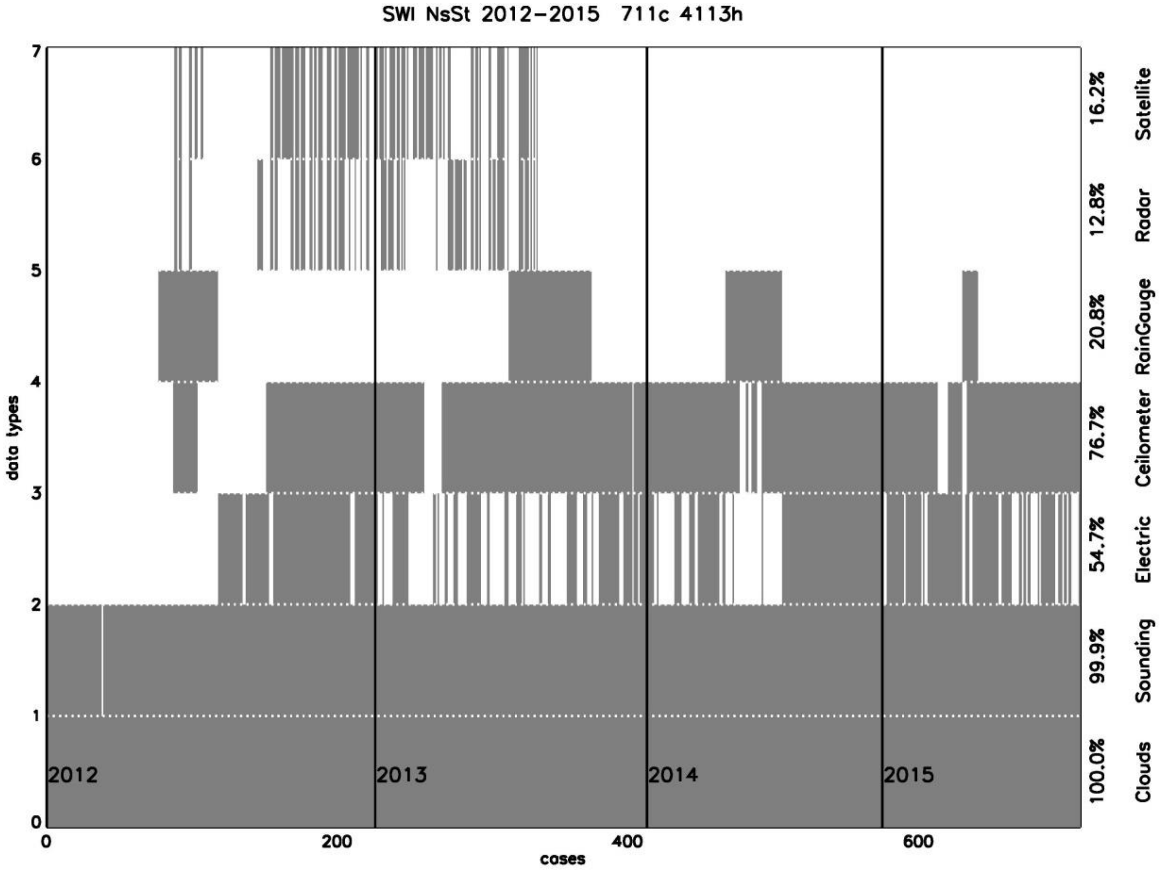

Fig. 7. Availability of the datasets relevant to the project and the identified St-Ns cases at Świder Station for the period 2012–2015. Here the cases are sorted by date, i.e., cases spanned over two or more days are split into several cases encoded in the date-related "pog" files (bottom row – clouds).

derive the total current (Eqs. 14 and 17), ceilometer recordings, rain gauge recordings, radar data, and satellite data. The availability of the electrical data is limited mainly by the absence of technically correct recordings of the current density, and, to a much less degree, of conductivity and the electric field. The availability of the ceilometer recordings is mainly limited by technical breaks in operation at the observatory. The technical breaks and failures decreased the usefulness of the data for the project aims significantly. For example, the full electric set data are usable for ~55% of cases. The rain gauge recordings allowing calculations of the precipitation rates are available mainly in warm seasons, and together with a full electric set the data are available for only ~30 cases, i.e., ~4%. The satellite and Legionowo radar datasets have been obtained for the identified then St and Ns cases at the end of the ELLEC grant project in late spring 2013, and do not cover the later cases. Nevertheless, the data and knowledge gathered during the project provide opportunities for extended research. The current and future studies concern the electricity of precipitation, and further investigation on the electrical structure of clouds and their role in the global circuit.

Acknowledgments. This work was financed by the Institute of Geophysics of the Polish Academy of Sciences with a subsidy from Poland's Ministry of Education and Science.

The scientific research and creation of the database have been supported by Polish National Science Centre grant NCN-2011/01/B/ST10/07188 (2011–2013) and grants of Poland's Ministry of Science and Higher Education (now Ministry of Education and Science) for the statutory activities of the Institute of Geophysics, Polish Academy of Sciences, Nos. 3841/E-

41/S/2014, 3841/E-41/S/2015, 3841/E-41/S/2016, 3841/E-41/S/2017, and 3841/E-41/S/2018. Observations at Hornsund and Arctowski Station have been particularly supported by the Polish National Science Centre grant NCN-2011/01/B/ST10/07118 (2011–2014).

Anna Odzimek expresses gratitude to Andrzej Kułak of AGH University of Technology for very helpful discussions on the atmospheric current measurement methods and the performance of the atmospheric current measurement apparatus at Świder. Anna Odzimek also thanks Magdalena Mielniczek for her voluntary help in uploading Legionowo atmospheric sounding data available from the University of Wyoming atmospheric sounding data website.

Appendix

INTEGER CODES FOR CLOUD GENERA, SPECIES AND VARIETY, AND PHENOMENA TYPES

Cloud genera

Code	Cloud genus
1	Ci
2	Cc
3	Cu
4	Cb
5	As
6	Ac
7	Cs
8	Sc
9	Ns
10	St

Cloud species and varieties

Code	Species or variety
0	None
1	Fibratus
2	Uncinus
3	Spissatus
4	Castellanus
5	Intortus
6	Vertebratus
7	Radiatus
8	Duplicatus
9	Mamma
10	Floccus
11	Stratiformis
12	Lenticularis
13	Undulatus

14	Lacunosus
15	Virga
16	Fractus
17	Humilis
18	Mediocris
19	Congestus
20	Praecipitatio
21	Arcus
22	Tuba
23	Pileus
24	Velum
25	Pannus
26	Calvus
27	Capillatus
28	Incus
29	Translucidus
30	Nebulosus
31	Opacus
32	Perlucidus

Phenomena

Code	Phenomenon
1	Rain
2	Intermittent rain
3	Drizzle
4	Intermittent drizzle
5	Freezing rain
6	Freezing drizzle
7	Snow
8	Intermittent snow
9	Granular snow
10	Sleet
11	Intermittent sleet
12	Intermittent granular snow
13	Hail
14	Soft hail
15	Small hail
16	Grains of ice
17	Ice needles
18	Snow-storm
19	Drifting snow near the ground
20	Drifting snow high up
21	Hoar frost
22	Soft rime

23	Glazed frost
24	Glazed frost on the ground
25	Fog
26	Ground fog
27	Mist
28	Ground mist
29	Ice mist
30	Layer mist
31	Haze
32	Dust haze
33	Dew
34	White frost
35	Water dust
36	Thunderstorm
37	Distant thunderstorm
38	Lightning
39	Tornado
40	Solar halo
41	Lunar halo
42	Rainbow
43	Aurora
44	Drizzle and rain
45	Intermittent drizzle and rain
46	Wind gusts
47	Freezing drizzle and snow
48	Intermittent freezing drizzle and snow
49	Intermittent freezing rain
50	Intermittent freezing drizzle
51	Solar corona
52	Lunar corona

References

Anderson, R.V. (1966), Measurements of total current density above active snowstorms, *J. Atmos. Terr. Phys.* **28**, 8, 789-790, DOI: 10.1016/0021-9169(66)90026-2.

Aspinall, W.P. (1969), Atmospheric Electric Charge Transfer in Precipitation and Associated Synoptic Conditions, PhD Thesis, Durham University.

Berlinski, J., G. Pankanin, and M. Kubicki (2007), Large scale monitoring of troposphere electric field, **In:** *Proc. 13th International Conference on Atmospheric Electricity, 13–17 August 2007, Beijing, China*, Vol. I, 124–126.

Chalmers, J.A. (1956), The vertical electric current during continuous rain and snow, *J. Atmos. Terr. Phys.* **9**, 5–6, 311–321, DOI: 10.1016/0021-9169(56)90149-0.

Chalmers, J.A. (1958), The electricity of Nimbo-Stratus clouds. **In:** L.G. Smith (ed.), Recent Advances in Atmospheric Electricity, Proceedings of the 2nd Conference on Atmospheric Electricity, New Hampshire, 20–23 May 1958, Pergamon Press, New York, 309–315.

Chomicz, W. (ed.) (1962), *Instrukcja dla Stacji Meteorologicznych*, Państwowy Instytut Hydrologiczno-Meteorologiczny. Seria A, Instrukcje i Podręczniki, Wydawnictwa Komunikacji i Łączności, Warszawa (in Polish).

Dziembowska, A. (2009), Eighty years of fair-weather atmospheric electricity monitoring in Poland, *Publs. Inst. Geoph. PAS* **D-73 (412)**, 9–14.

Gajda, W. (2013), Opracowanie danych radarowych poświęcone elektryczności chmur Nimbostratus i Stratus, digital document prepared for the purpose of ELLEC project, 15 pp. (in Polish).

Gerdien, H. (1905), Demonstration eines Apparates zur absoluten Messung der elektrischen Leitfähigkeit der Luft, *Phys. Z.* **6**, 800–801 (in German).

Houze, R.A., Jr. (1993), *Cloud Dynamics*, Academic Press Inc., New York.

Imyanitov, I.M. (1957), *Instruments and Techniques for Investigating the Electricity of the Atmosphere* [Pribory i metody dlya izucheniya elektrichestva atmosfery], Gostekhizdat, Moscow (in Russian).

Imyanitov, I.M., and K.S. Shifrin (1962), Present state of research on atmospheric electricity, *Sov. Phys. Usp.* **5**, 2, 292–322, DOI: 10.1070/PU1962v005n02ABEH003413.

Imyanitov, I.M., Ye.V. Chubarina, and Ya.M. Shvarts (1974), *Cloud Electricity* [Elektryczność Chmur], Państwowe Wydawnictwo Naukowe, Warszawa, 139 pp. (in Polish).

Kubicki, M., (2006), Results of Atmospheric Electricity and Meteorological Observations, S. Kalinowski Geophysical Observatory at Świder, 2005, *Publs. Inst. Geoph. PAS* **D-71 (391)**.

Kubicki, M., A. Odzimek, M. Neska, J. Berliński, and S. Michnowski (2016), First measurements of the Earth's electric field at the Arctowski Antarctic Station, King George Island, by the new Polish atmospheric electricity observation network, *Acta Geophys.* **64**, 6, 2630–2649, DOI: 10.1515/acgeo-2016-0096.

Liu, C., E.R. Williams, E.J. Zipser, and G. Burns (2010), Diurnal variations of global thunderstorms and electrified shower clouds and their contribution to the global electrical circuit, *J. Atmos. Sci.* **67**, 2, 309–323, DOI: 10.1175/2009JAS3248.1.

MacGorman, D., and W.D. Rust (1998), *The Electrical Nature of Storms*, Oxford University Press, New York, 422 pp.

Magono, C., and K. Orikasa (1966), On the disturbance of surface electric field caused by snowfall, *J. Meteorol. Soc. Japan Ser. II*, **44**, 260–278, DOI: 10.2151/jmsj1965.44.5_260.

Matuszko, D., and J. Soroka (2013*), Zachmurzenie Spitsbergenu na Podstawie Obserwacji w Polskiej Stacji Polarnej w Hornsundzie. Cloudiness over Spitsbergen Based on Observations Made at the Polish Polar Station in Hornsund*, Instytut Geografii i Gospodarki Przestrzennej UJ, Kraków, 96 pp.

Michnowski, S., S. Israelsson, J. Parfiniewicz, M.A. Enaytollah, and E. Pisler (1987), A case of thunderstorm system development inferred from lightning distribution. **In:** *Publs. Inst. Geoph. PAS* **D-26 (198)**, 3–57.

Odzimek, A., M. Lester, and M. Kubicki (2010), EGATEC: A new high-resolution engineering model of the global atmospheric electric circuit—Currents in the lower atmosphere, *J. Geophys. Res.: Atmos.* **115**, D18, D18207, DOI: 10.1029/2009JD013341.

Odzimek, A., M. Kubicki, and P. Barański (2014), Ground-level atmospheric electricity under low-level stratiform clouds. **In:** *Proc. 15th International Conference on Atmospheric Electricity, 15-20 June 2014, Norman, USA*, 7 pp.

Odzimek, A., M. Kubicki, P. Barański, and D. Jasinkiewicz (2017a), Nimbostratus cloud cases at Geophysical Observatory IG PAS in Świder in 2005–2015, RepOD, V1, DOI: 10.18150/repod.2362097.

Odzimek, A., M. Kubicki, P. Barański, and D. Jasinkiewicz (2017b), Stratus cloud cases at Geophysical Observatory IG PAS in Świder in 2005–2015, RepOD, V1, DOI: 10.18150/repod.8954639.

Odzimek, A., P. Barański, M. Kubicki, and D. Jasinkiewicz (2018), Electrical signatures of Nimbostratus and Stratus clouds in ground-level vertical atmospheric electric field and current density at mid-latitude station Świder, Poland, *Atmos. Res.* **209**, 188–203, DOI: 10.1016/j.atmosres.2018.03.018.

Ramsay, M.W., and J.A. Chalmers (1960), Measurements on the electricity of precipitation, *Q. J. Roy. Meteorol. Soc.* **86**, 370, 530–539, DOI: 10.1002/qj.49708637010.

Reda, J., and M. Neska (2016), The One Second data collection system in Polish geomagnetic observatories, *J. Ind. Geophys. Union, Sp. Vol.* **2**, 62–66.

Reiter, R. (1965), Precipitation and cloud electricity, *Q. J. Roy. Meteorol. Soc.* **91**, 387, 60–72, DOI: 10.1002/qj.49709138709.

Reiter, R. (1968), Results of investigation on precipitation and cloud electricity based on 15 years of observation, *Arch. Met. Geoph. Biokl. Ser. A* **17**, 17–29, DOI: 10.1007/BF02250790.

Reiter, R. (1972), Contribution to the problem of precipitation electricity, *Arch. Met. Geoph. Biokl. Ser. A* **21**, 247–272, DOI: 10.1007/BF02247975.

Rust, W.D., and R.J. Trapp (2002), Initial balloon soundings of the electric field in winter nimbostratus clouds in the USA, *Geophys. Res. Lett.* **29**, 20, 20-1–20-4, DOI: 10.1029/2002GL015278.

Serafin-Rek, D. (2013), Opis SAFNWC-Seviri, digital document prepared for the purpose of ELLEC project, 3 pp.

Wilson, C.T.R. (1906), On the measurement of the earth-air current and on the origin of atmospheric electricity, *Proc. Cambridge Philos. Soc.* **13**, 6, 363–382.

Wilson, C.T.R. (1921), Investigations on lightning discharges and on the electric field of thunderstorms, *Phil. Trans. Roy. Soc. London A* **211**, 73–115, DOI: 10.1098/rsta.1921.0003.

Witkowski, M.-A. (1902), Note sur l'électricité atmosphérique á Zakopane dans les Tatras [Spostrzeżenia nad elektrycznością atmosferyczną w Zakopanem], *Bull. Int. Acad. Sci. Cracovie* **1**, 7-10.

Received 16 September 2022
Received in revised form 30 December 2022
Accepted 31 December 2022

Publications of the Institute of Geophysics, Polish Academy of Sciences
Geophysical Data Bases, Processing and Instrumentation
vol. 442 (D-77), 2022, pp. 41-54
DOI: 10.25171/InstGeoph_PAS_Publs-2022-024

Red Sprites over Thunderstorms in Czech Republic, Germany and Poland Observed from Gliwice in 2011–2013

Anna ODZIMEK[1,✉], Magdalena MIELNICZEK[2], Monika PAJEK[3], and Petr NOVÁK[4]

[1]Institute of Geophysics, Polish Academy of Sciences, Warszawa, Poland

[2]Gliwice, Poland

[3]Institute of Meteorology and Water Management – National Research Institute, Kraków, Poland

[4]Czech Hydrometeorological Institute, Prague, Czech Republic

✉ aodzimek@igf.edu.pl

Abstract

Nigh-time observations of red sprites phenomena over thunderstorm seasons of 2011–2013 from Gliwice (52.116°N, 21.238°E) resulted in 45 events observed above convective storm system in the Czech Republic, Germany, and south-western Poland. This paper gives details of the observed events along with the correlation of optical data with cloud-to-ground and in-cloud lightning recorded by the CELDN lightning detection system. We also analyse the time sequence and locations of parent lightning in dancing sprites events produced at various stages of the thundercloud development and sprite production using visualisation of their locations mapped onto the "overshooting-tops" satellite images derived from Meteosat SEVIRI instrument data.

Keywords: TLEs, lightning, sprites, CELDN, OST, satellite imagery, dancing sprites.

1. INTRODUCTION

The red, milliseconds-long optical emissions observed high above thunderstorm systems usually come from upper-atmosphere lightning, or Transient Luminous Events, called "red sprites", in short "sprites". Early observations established that sprites are associated with positive cloud-to-ground (+CG) lightning discharges, accompanied by in-cloud (IC) lightning, and are able to discharge a substantial portion of positive charge accumulated in thunderclouds which can result in the dielectric breakdown in the stressed atmosphere above (e.g., Lyons 2006).

Sprites have been observed in Central Europe since at least 2003 (Bór et al. 2009; Bór 2013; Iwański et al. 2009; Arnone et al. 2020). In this work we summarise the results of observations of sprites from Gliwice, Poland, where the possible directions of optical observations of sprites span from the South to North-West, giving the possibility of observations of sprite activity of distant (~500 km) thunderstorms over the Czech Republic, Austria, southern Germany, and south-western Poland. The first part of the paper is aimed at providing detailed information on the number and types of observed sprites as well as providing corrected times of the events. In the second part we analyse positions of sprite parent lightning, selected from detections by the CELDN system, overlaid on satellite imagery-based mappings processed from the EUMETSAT Meteosat data and displaying the "overshooting tops" (OST) cloud features. Our focus is especially directed toward dancing sprites, i.e., the sprite formations being a series of sprites occurring one after another and in some spatial distance from the previous (Lyons 1994).

2. OPTICAL OBSERVATIONS OF SPRITES FROM GLIWICE

Observations have been run from a private flat in the Sikornik area of Gliwice (52.116°N, 21.238°E). The view from the western side allowed successful observations at azimuth range from approximately 180 (South) to 280 (West-N-West). The observational set-up consisted of a monochrome Watec 902H2 Supreme 1/2" low-light TV camera of the frame rate of 50 frames per second, CBC Computar lens (16 mm, F1/4 or 6 mm, F1/2), a time overlay – on-screen display (OSD) unit called KIWI-OSD[1] equipped with a Garmin GPS[2] antenna. The TV signal was analysed by the UFOCapture V2 programme from SonotaCo.com[3] installed on a personal computer. The software saved the video signal of detected objects in .avi and .jpg (such as in Fig. 1b) formats. Observational settings followed the UFOCapture programme settings recommended for the detection of TLEs. The camera was pointed manually using supporting information on the location of storm and lightning activity from meteorological radar maps and satellite

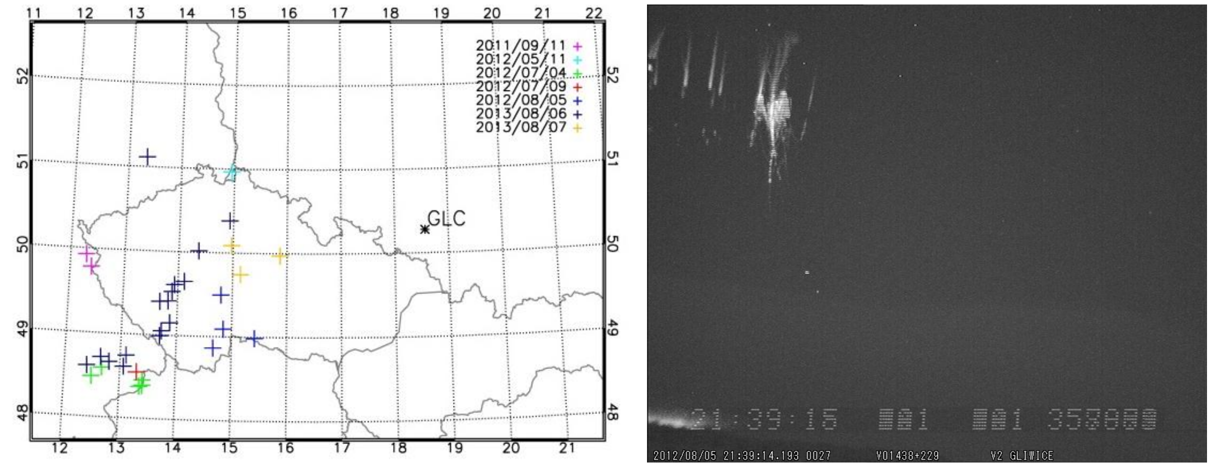
a)

b)

Fig. 1: a) Map of locations of assigned CG parent lightning of sprite events observed on subsequent dates of observations (see Tables 1 and 2); b) example of multiple-sprite event recorded from Gliwice on 5 August 2012, ~21:39:15 UTC (peak-hold image). The event (No. 19 in Table 2) consists of two sprite clusters visible on the left side of the image. They are displaced in space but happening partly simultaneously. One is a cluster of column sprites possibly arranged in a ring. The other is a lone angel or developing carrot sprite. Cloud lightning is visible left at the bottom of the image.

---

[1] Online at http://sites.google.com/site/kiwiosd

[2] Global Positioning System, https://www.gps.gov

[3] Online at http://sonotaco.com/e_index.html

imagery and maps of lightning detection available online. Initial azimuth has been usually calculated using PanTiltCalc software written by Lasse Clausen (Odzimek et al. 2008). The system was manually switched on and operated in favourable viewing conditions. The usage of lens with ~60° in the horizontal field of view (FOV) in 2013, compared with ~20° FOV in previous years has limited correct identification of the sprite species and, on the other hand, enabled capturing sprites over a wider area, including several dancing sprites events.

Sprites analysed here were observed over May–September in 2011–2013 with the majority of events observed in July and August. Observational logs indicate there were at least 27 nights of observations in total: 11 in 2011, 14 in 2012, and 2 in 2013 – one of the last two, on 6–7 August 2013, was one of the most successful nights of observations in terms of sprite production, in addition to 4 July 2012 and 5 August 2012. In 29 video recordings, 48 events have been recorded, including 7 cases of dancing sprites on the night of 6–7 August 2013, at ~21:27:53 UTC, ~21:33:27 UTC, ~21:45:27 UTC, ~22:38:31 UTC, ~22:42:27 UTC, ~22:59:38 UTC, and ~00:19:49 UTC. In the selection of these events we relied on the visual effect received from the video rather than by measurements of the time separation between sprites and locations. Other interesting events observed at Gliwice include column sprites that proceeded one after another in the same location, in cases considered as rebrightening (e.g., Bór et al. 2018). These are cases of 11 May 2012 at ~21:48:08 UTC and 7 August 2013 at ~23:02:22 UTC. The first sprite observed on 9 September 2011 was preceded by a sprite halo. The two events of 9 September 2011 have been subjected by Odzimek et al. (2013) to detailed analysis of their total, i.e., IC+CG, parent lightning, and the sprites' locations obtained from the triangulation of observations of these events from Gliwice and from Sopron in Hungary

Tables 1 and 2 provide details of the observed events. Table 1 gives information on the dates, and whether the recordings were time-stamped with the GPS, commonly used for precise positioning in time and space. In case the GPS times are absent, constant corrections to PC time are given rounded to the nearest multiple of 50 ms, valid for the whole time of observations or a limited period. These time shifts have been determined by comparison of a series of times of the observed sprites and a series of lightning detections from lightning detection systems over the area. The methodology of calculation of the time shifts as well as of the final estimate of the event times and their errors are described in Odzimek and Mielniczek (2022). Times listed in Table 2 are already given with the time corrections applied. Table 2 provides information on the number of events and subevents captured in each video recording, listed chrono-

Table 1

Summary of sprite observations from Gliwice over 2011–2013

No. nights	Dates	Direction from Gliwice	Time UTC (sprites observed)	Event count	GPS stamp	Time shift (intervals) [s]
1	2011/09/11	NW	20:18–20:23	2	No	+22.85
2	2012/05/11	W	21:48	2	No	–1.35
3	2012/07/04	SW	21:54–22:40	5	No	+0.50
4	2012/07/09	SW	00:44	1	Yes	0
5	2012/08/05	SW	20:47–21:53	8	Yes	0
6	2013/06/08-07	WSW	20:06–00:19	13	GPS missing from 20:30 UTC	+0.35 (21:30–22:05) +0.55 (22:35–23:00) +0.70 (23:55–00:20)
7	2013/08/07	W	23:02	1	Yes	0

Table 2

Details of sprite cases observed from Gliwice in 2011–2013

Count	No. date	No. video	No. event	Sub-event count	Estimated time	Error[4] [ms]	Event description	CELDN parent lightning stroke type and time	CELDN parent CG RS current [kA]
1	#1	#1	#1	2	2011/09/11 20:18:27.404-584 20:18:27.585-645	50	Cluster of columns preceded by a halo Cluster of carrots	+CG 20:18:27.396 20:18:27.399	+5 +11
2		#2	#1	1	2011/09/11 20:22:16.435-475 20:22:16.603-663	50	Multiple columns	IC+CG 20:22:16.499	+6
3	#2	#1	#1	1	2012/05/11 21:48:07.899-959	26	Single column	IC+CG 21:48:07.945	+151
4			#2	1	2012/05/11 21:48:08.019-039	26	Single column repeated in same place as #1	IC+CG 21:48:08.024	+21
5	#3	#1	#1	1	2012/07/04 21:54:08.172-212	21	Cluster of columns	IC+CG 21:54:08.023	+57
6		#2	#1	1	2012/07/04 22:12:33.091-131	21	Cluster of wishbones with dots	IC+CG 22:12:33.097 22:12:33.147 22:12:33.197	+10 +89 +8
7		#3	#1	1	2012/07/04 22:18:17.672-712	21	Cluster of wishbones with an angel	IC+CG 22:18:17.742 22:18:17.742	+96 +17
8		#4	#1	1	2012/07/04 22:21:26.938-978	29	Cluster of carrots	IC+CG 22:21:26.954	+6
9		#5	#1	1	2012/07/04 22:39:43.017-077	24	Cluster of carrots with an angel	IC+CG 22:39:43.006	+188
10	#4	#1	#1	1	2012/07/09 00:44:25.328-368	19	Cluster of carrots	IC+CG 00:44:25.300	+39
11	#5	#1	#1	1	2012/08/05 20:47:18.395-555	0	Cluster of columns with dots	IC, no CG	
12			#2	1	2012/08/05 20:47:18.495-575	0	Cluster of columns with a carrot	IC, no CG	
13		#2	#1	1	2012/08/05 20:51:36.481-581	0	Cluster of columns	IC, no CG	
14		#3	#1	1	2012/08/05 20:54:08.926-09.046	0	Cluster of trees and angels with dots and tendrils	+CG 20:54:08.917	+41

to be continued

---

[4] This is inividual error due to time corrections within the recording. Additional 50 ms are to be added in case timing of whole series of events has been corrected with a constant calculated translation in time as detailed in the last column of Table 1.

Table 2 (continuation)

Details of sprite cases observed from Gliwice in 2011–2013

15			#2	1	2012/08/05 20:54:09.066-146	0	Cluster of columns with dots and tendrils		IC+CG 20:54:09.079	+26
16		#4	#1	1	2012/08/05 20:58:07.433-453	0	Cluster of columns with dots and tendrils jellyfish		no IC or CG	
17		#5	#1	1	2012/08/05 20:59:55.856-896	0	Cluster of wishbones with dots		no IC or CG	
18		#6	#1	1	2012/08/05 21:06:00.106-126	0	Cluster of carrots		no IC or CG	
19		#7	#1	2	2012/08/05 21:39:15.881-961 21:39:15.921-16.001	0	Cluster of columns with dots Single angel with dots and tendrils		IC+CG 21:39:15.846 21:39:15.860 21:39:15.866	+99 +8 +11
21		#8	#1	1	2012/08/05 21:52:51.404-484	37	Multiple columns with dots		IC+CG 21:52:50.353	+46
22	#6	#1	#1	1	2013/08/06 20:06:58.705-725	0	Cluster of columns		no IC or CG*	
23		#2	#1	1	2013/08/06 20:24:14.276-296	0	Single carrot		IC+CG 20:24:14.279	+78
24		#3	#1	1	2013/08/06 21:27:52.932-952	29	Double carrot	dancing	no IC or CG	
25			#2	1	2013/08/06 21:27:53.112-152	29	Cluster of carrots		IC+CG 21:27:53.111	+95
26			#3	1	2013/08/06 21:27:53.332-352	29	Double carrot		IC+CG 21:27:53.208	+42
27			#4	1	2013/08/06 21:27:53.492-512	29	Cluster of columns		no IC or CG	
28		#4	#1	1	2013/08/06 21:33:21.777-797	20	Cluster of columns with tendrils jellyfish		+CG 21:24:14.607	+186
28		#5	#1	1	2013/08/06 21:36:49.001-021	18	Cluster of carrots		+CG 21:36:48.832	+127
29		#6	#1	1	2013/08/06 21:45:27.964-28.004	18	Cluster of unrecognised sprites	dancing	IC+CG 21:45:27.941	+53
30			#2	1	2013/08/06 21:45:28.144-164	18	Single carrot		IC+CG 21:45:28.080 21:45:28.094 21:45:28.171 21:45:28.171	+19 +10 +73 +167
31			#3	2	2013/08/06 21:45:28.164-204 21:45:28.184-204	18	Double carrots Cluster of carrots		+CG 21:45:28.094 21:45:28.171 21:45:28.171	+10 +73 +167

to be continued

Table 2 (continuation)

Details of sprite cases observed from Gliwice in 2011–2013

32		#7	#1	1	2013/08/06 22:01:45.025-065	29	Cluster of carrots in circle		IC+CG 22:01:45.120	+37
33			#2	1	2013/08/06 22:01:45.582-602	29	Cluster of columns with tendrils		IC+CG 22:01:45.641	+156
34		#8	#1	1	2013/08/06 22:38:31.740-780	18	Multiple columns with tendrils, jellyfish	dancing	IC+CG 22:38:31.717 22:38:31.718	+18 +184
35			#2	1	2013/08/06 22:38:31.560-680	18	Multiple carrots		IC+CG 22:38:31.846 22:38:31.846	+65 +89
36		#9	#1	1	2013/08/06 22:42:27.580-640	21	Cluster of unknown	dancing	IC+CG 22:42:27.559 22:42:27.644	+77 +15
37			#2	1	2013/08/06 22:42:27.620-660	21	Cluster of unknown		IC+CG 22:42:27.559 22:42:27.644	+77 +15
38			#3	1	2013/08/06 22:42:27.660-740	21	Multiple unknown		+CG 22:42:27.559 22:42:27.644 22:42:27.806	+77 +15 +146
39			#4	1	2013/08/06 22:42:27.820-840	21	Cluster of columns with tendrils, jellyfish		+CG 22:42:27.806 22:42:27.899	+146 +12
40		#10	#1	1	2013/08/06 22:52:17.167-187	17	Cluster of columns with tendrils, jellyfish		IC+CG 22:52:17.099 22:52:17.153	+21 +165
41		#11	#1	1	2013/08/06 22:59:38.969-39.009	17	Cluster of carrots	dancing	+CG 22:59:38.962	+106
42			#2	1	2013/08/06 22:59:38.089-129	17	Double carrots		+CG 22:59:39.135	+125
43			#3	1	2013/08/06 22:59:39.149-169	17	Cluster of columns and wishbones		+CG 22:59:39.135	+125
44		#12	#1	1	2013/08/06 23:58:40.883-923	17	Cluster of carrots or trees	dancing	+CG 23:58:40.797	+53
45			#2	1	2013/08/06 23:58:41.243-283	17	Cluster of columns with tendrils		+CG 23:58:41.102 23:58:41.221 23:58:41.221	+11 +26 +61

to be continued

Table 2 (continuation)
Details of sprite cases observed from Gliwice in 2011–2013

46	#7	#1	#1	1	2013/08/07 00:19:49.861-921	17	Cluster of columns and wishbones	dancing	+CG 00:19:49.868	+35
47			#2	1	2013/08/07 00:19:50.201-241	17	Cluster of carrots in circle		IC+CG 00:19:50.096 00:19:50.230	+19 +53
48		#2	#1	2	2013/08/07 23:02:22.448-488 23:02:22.488-548	0	Single column Single column repeated		+CG 23:02:22.457 23:02:22.491	+158 +51
Total				52						

*Indications of parent lightning confirmed in lightning dataset used for Eurosprite campaigns (e.g., Arnone et al. 2020).

logically, and calculated time errors resulting for the corrections of the timing within video recordings. An additional 50 ms error is to be applied for events with the time correction performed on series of events without GPS timing (see Table 1). The total number of subevents, i.e., sprites which may be of different types or be spatially displaced but captured in the same video field sequence (starting in intervals not exceeding one frame lasting 40 ms) amounts to 52.

3. SUPPORTING OST SATELLITE PRODUCTS

A thundercloud’s overshooting top (Glickman 2000), the cloud’s part protruding high beyond the troposphere, indicates a high degree of its vertical development and activity which may be associated with severe weather phenomena. The need for detecting such features with remote sensing methods resulted in the development of OST nowcasting products (e.g., Pajek et al. 2008, Bedka et al. 2010). An OST product is generally based on the difference of brightness temperatures in two infrared spectral channels, and the highest differences of these temperatures are related to the occurrence of the overshooting tops.

In the case of sprite observations, we rather look for periods when the activity decreases (Odzimek and Pajek 2016), and the OST maps help to identify locations of the stratiform precipitation area (characterised by lower brightness temperature gradients) over which the most intense sprite production may occur. For confirmation we have also checked the Czech meteorological radar data published at the Czech Hydrometeorological Institute website[5]. The observations have been supported by the display OST images in near-real-time at 15-min frequency (Odzimek et al. 2014). These OST products were processed from the EUMETSAT Meteosat imagery data of the SEVIRI instrument channels at 6.2 μm and 10.8 μm, at the Institute of Meteorology and Water Management – National Research Institute (IMWM-NRI) in Kraków. The images have been prepared in two formats: one covering whole Europe and another focused on the locations of observations sites in Poland and the neighbourhood. Examples of such OST images from the four most active nights of observations are shown in Fig. 2.

---

[5] Online at https://www.chmi.cz/

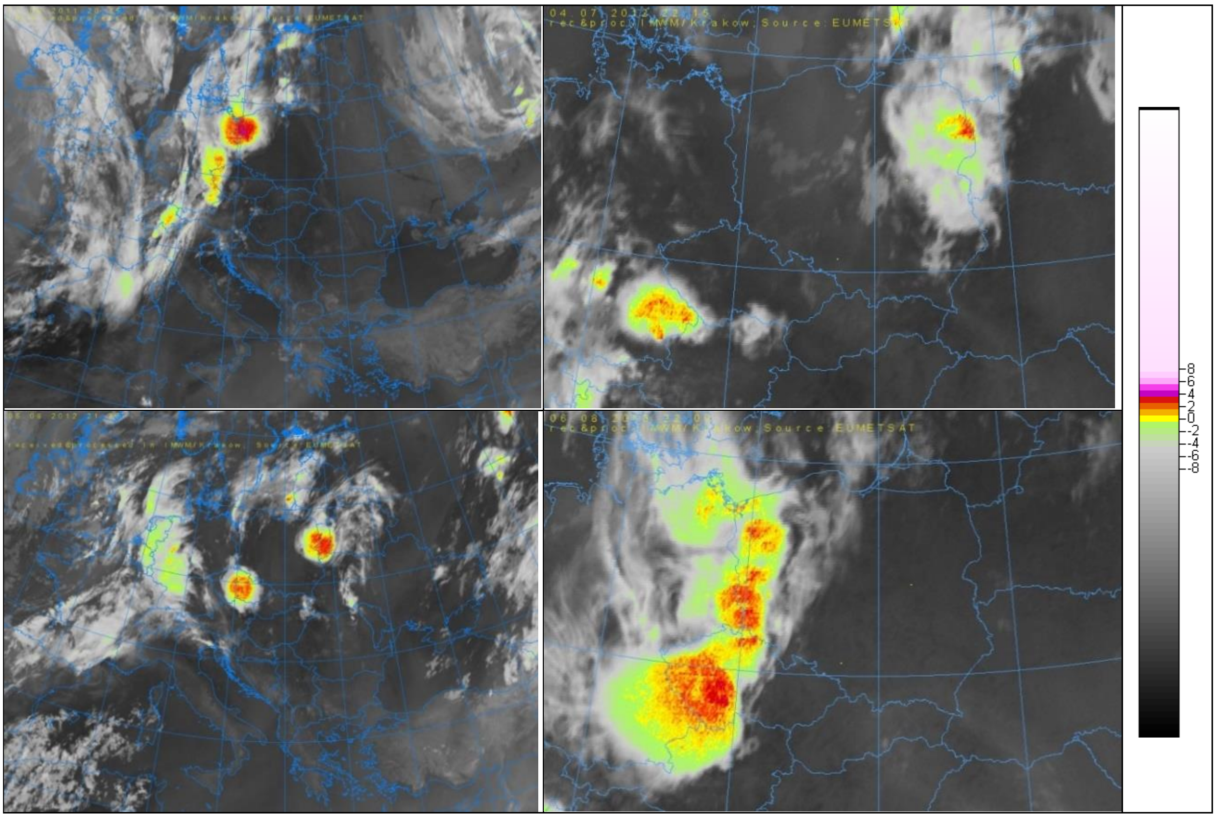

Fig. 2. The "overshooting tops" images of the sprite-producing thunderstorms in Central Europe, processed at IMWM-NRI in Kraków from Meteosat SEVIRI imagery. Top left: 11 September 2011, 20:15 UTC; top right: 4 July 2012, 22:15 UTC; bottom left: 5 August 2012, 21:30 UTC; bottom right: 6 August 2013, 22:00 UTC. The selected moment is approximately in the middle of the sprite production period by a storm. Rightmost: the scale for the OST brightness temperature gradient.

4. PARENT THUNDERSTORMS AND PARENT LIGHTNING OF SPRITES

Table 2 includes also information on parent lightning identified in the detections of cloud-to-ground and in-cloud lightning by the CELDN (Central European Lightning Detection Network) system used in the Czech Republic (e.g., Novák and Kyznarová 2011). CELDN differentiates between cloud-to-ground and in-cloud lightning and provides the location and polarity of both types of lightning. In many sprite cases, positive CG parent lightning, SP+CG, have been identified among CELDN detections. Also, many positive ICs (not listed) have been associated as parent. The positive in-cloud lightning strokes prevail as associated parent lightning approximately at the ratio 2:1 with respect to negative IC lightning. Association as a parent lightning was considered positive in case the lightning occurred in the vicinity of aimed location and within the time range of 100 ms from the start of the first video field till the ending of last field containing the event, including errors. In cases when the time shift was applied, the duration of the range was prolonged by 50 ms from both ends.

4.1 Post-analysis of combined OST and CELDN lightning data

In this section we use information resulting from combining OST and lightning data in regard to parent lightning of sprite events. By mapping the lightning positions onto the OST products we obtain the relative position of lightning in the convective or stratiform area of the parent

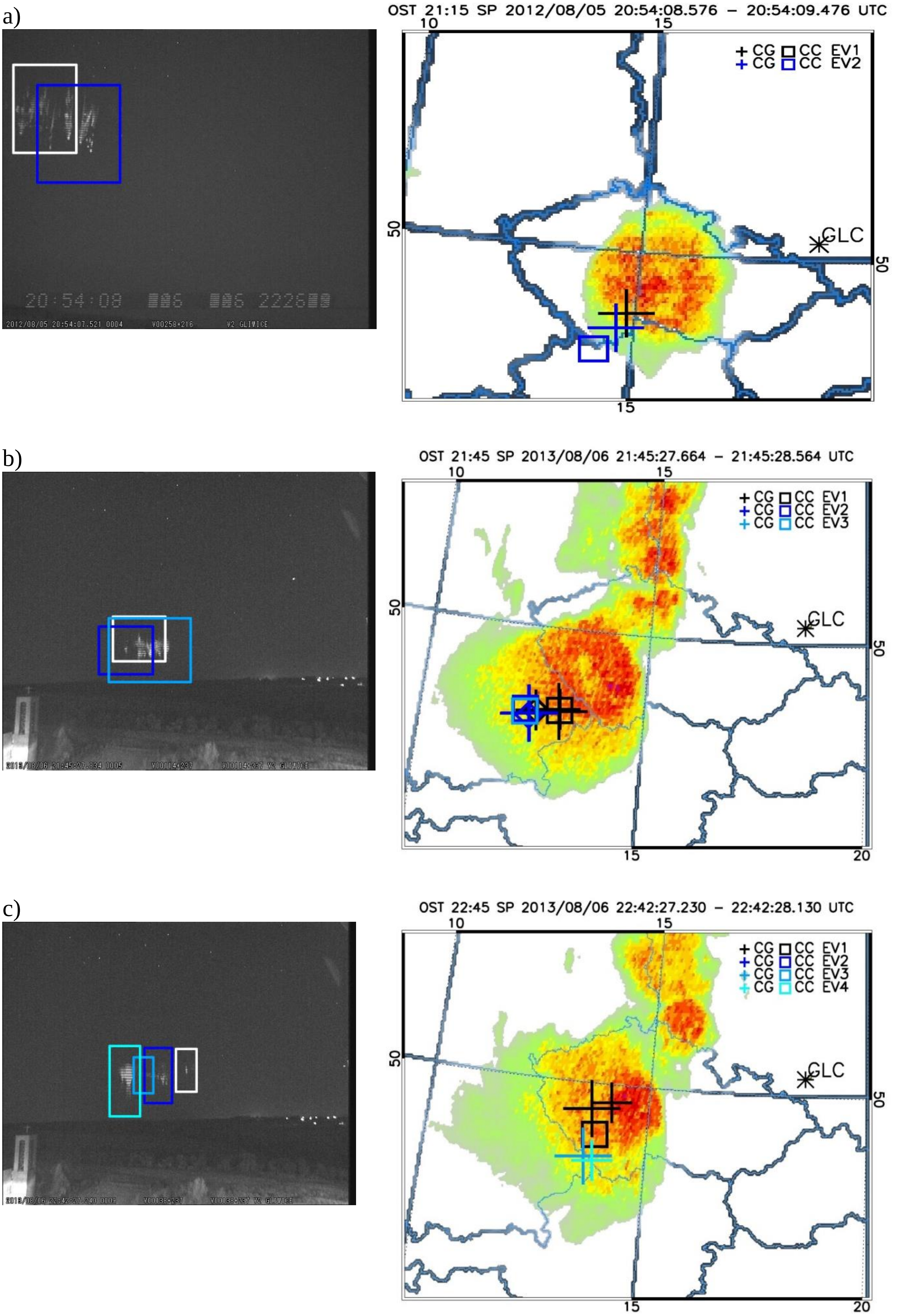

Fig. 3. Continuation on the next page.

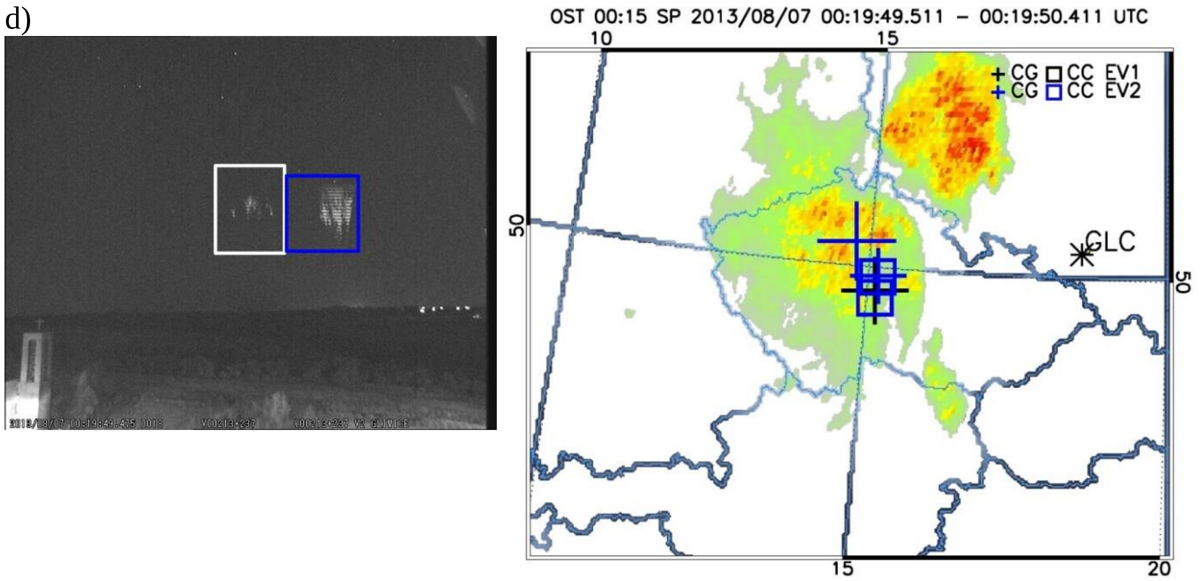

Fig. 3. Peak-hold images (left) of sprites and the map of parent lightning (right) of subsequent events (EV) coloured black (or white), blue, light blue, turquoise from oldest to latest in cases of: a) 5 August 2012, 20:54:08 UTC, events 14–15; b) 6 August 2013, 21:45:27 UTC, events 29–31; c) 6 August 2013, 22:42:27 UTC, events 36–39; d) 7 August 2013, 00:19:49 UTC, events 46–47. Legend: crosses mark locations of +CGs, squares mark locations of +CCs, diamonds mark locations of –CCs.

storm, and, in the case of multiple-sprite events, the position of subsequent parent strokes. Results of such analysis are presented in Fig. 3. In four multiple-sprite events, we show the position and sequence of parent lightning associated with a consecutive event mapped on the OST image reflecting also the stage of the thundercloud development. The grey "background" around the active clouds, visible in examples in Fig. 2, has been erased to white in order to make the images more clear.

The first example in Fig. 3a is a two-event case of 5 August 2012 starting at ~20:54:08 UTC when a cluster of tree and angel sprites with tendrils was followed by a cluster of column sprites. In Fig. 3b-d similar mappings are presented for the three cases of dancing sprites on 6–7 August 2013, at ~21:45:27 UTC, ~22:42:27 UTC, and ~00:19:49 UTC. Each example is represented in Fig. 3 by a peak-hold image of an event (panels on the left) and an OST map (panels on the right). The locations of parent lightning associated with subsequent events are mapped on the OST image and coloured differently, depending on which subsequent event it was associated with. Locations of the subsequent events are also marked by colour frames in the peak-hold images (black is replaced by white).

The three selected dancing events occurred at various stages of the thundercloud development. The first one (Fig. 3b) belongs to a still active phase, although some signs of decay of the vertical size can also be noticed. The second one (Fig. 3c) happens in the continuing decay phase, and the third (Fig. 3d) in the latest stages of this thunderstorm and production of sprites.

5. DISCUSSION

Among sprites recorded from Gliwice there are events recognised as column, carrot, wishbone, tree, and angel sprites. Sprite types in four events were not recognised. Compared with sprites observed from Świder (SWI) in the north (Odzimek et al. 2022, this issue), carrot sprites are more numerous (44% at GLC vs. 23% at SWI) and column sprites are less prevalent, although still most common (46% at GLC vs. 72% at SWI). Jellyfish formations, familiar from other

Central European sprite observational campaigns (e.g., Bór 2013) are on a comparable level (11% at GLC vs. 13% at SWI). In addition, compared with one dancing event observed in 2012 from Świder here we have recordings of 7 dancing sprites events; albeit they have been products of rather exceptional situation on the night of 6–7 August 2013 (Fig. 2d) when several long-lived mesoscale thunderstorms developed west of the Germany-Czech Republic and Germany-Poland border, at times merging their cells into one system. Approximately 20% of the events are mixed events comprising different types of sprites in different organisation, i.e. single sprites or groups of sprites in less or more organised groups and clusters such as that in Fig. 1b. The longest sprite sequences comprising up to 2 sprite subevents have been captured in a sequence of video frames lasting up to 6 video fields equivalent to 120 ms. A dancing event is composed of a series of single or mixed-sprite events, and its duration may be several hundred milliseconds.

Bór et al. (2018) have analysed the location of the sequence of lightning in five dancing events of 6/7 August 2013 in detail, including events at ~21:45:27 UTC and ~22:42:27 UTC analysed here. They also determined triangulated positions of events observed simultaneously from two observational stations, and studied their relation to the parent of next sprite events in the dancing sequence. Similarly to previous observations (e.g., Lang et al. 2010; Soula et al. 2017; Tomicic et al. 2021, and references therein) it emerged that the sequence was such that the next sprite and its parent lightning SP+CG occurred each time farther away from the convective core of the thunderstorm, and closer to the rear of the thunderstorm and its stratiform part. This is in agreement with general positive lightning activity in an active MCS system (e.g., Carey et al. 2005). The maps in Fig. 3a-c support such a scenario, as also does the sequence of parent lightning in the dancing events at ~22:01:44 UTC and ~22:59:38 UTC (not shown). In a smaller thunderstorm system, like the one of 5 August 2012, the edge-of-core-to-rear progression of SP+CG seems also valid, as the first example at ~20:54:08 UTC shows. The events in Fig. 3d at ~00:19:49 UTC on 7 August 2013 show the opposite behaviour. They happened in the latest stages of this thunderstorm system and the OST map from 00:15 UTC reflects the already devolved structure of the thunderstorm. The division into leading convective and trailing part is no longer so clear – the whole structure collapses, and perhaps therefore the path of consecutive lightning produced by the decaying thunderstorm is different. This event would also support the postulate that the distribution of positive charge producing different potential difference received by the negative leader of propagating lightning helps to maintain or stop the development of this lightning.

It has been also previously hypothesised that in the case of dancing sprites the series of +CG parent lightning together with in-cloud lightning are part of one complex lightning discharge, recently called a megaflash (Lyons et al. 2020). The second dancing event at ~22:42:37 UTC (and a very similar at ~22:38:31 UTC, not shown), may potentially be the product of a parent megaflash – an extended lightning that produces a series of positive CGs and sprites along – resulting in such multi-event dancing sprites. The thunderstorm system of 6/7 August 2013 had sufficiently large surface area (covering more than half of the Czech Republic) with an extensive stratiform part where such lightning could develop, discharging the vast reservoir of positive charge along and producing dancing sprites. Looking at the maps displaying the types and locations of lightning by CELDN we find intra-cloud detections along SP+CG but the interpretation of the total lightning path is not possible. On the other hand, parent lightning of the dancing sprites at ~21:27:53 UTC occurred no later than the end of the first event, so the other events might have been rather associated with resurges in the +CG continuing currents – such occurrences were reported by Lu et al. (2013). In the two-sprite event shown in Fig. 3a no in-cloud lightning has been detected but each sprite has its probable parent +CG.

6. SUMMARY

The total of 52 TLEs of the red sprite type TLE events have been recorded optically between September 2011 and August 2015 from Gliwice. The ratio of column and carrot sprites, observed over the area of the Czech Republic and parts of Germany and Poland, is higher than that based on observations in the north of Poland. Some long-lived storms, such as those on the nights of 11 September 2011, 4 July 2012, 5 August 2013, and 6–7 August 2013, have been prolific in the production of sprite-lightning, especially the last one which produced several dancing sprite events. There were also observed two events of column sprite rebrightening. We have utilised Meteosat satellite imagery used for detection of thunderclouds' overshooting tops (OST) for analysing the sequence of the sprites' parent lightning locations in some multiple-sprite events, on the background of the thunderclouds structure as denoted by the OST. The products provide another valuable opportunity for the investigation of the relationships between parent lightning and dancing sprite events. The observed rule that subsequent SP+CGs proceed away from the verge of convective parts towards the stratiform rear holds in the active phase of the parent thunderstorm system but in the latest stage of decay the progression may become disorganised.

Acknowledgments. This work is supported by subsidies from Poland's Ministry of Education and Science to the Institute of Geophysics, Polish Academy of Sciences (IG PAS).

The system for sprite observations at Gliwice has been provided from the private resources of authors A. Odzimek and M. Mielniczek.

We acknowledge that the Meteosat satellite images used during observations have been processed at IMWM-NRI in Kraków in agreement with the EUMETSAT licence IMWM/LIC/MSG/10/06 (50002869), and uploaded to a server at IG PAS. We thank Mariusz Neska of IG PAS for his support in organising this upload.

We thank Torsten Neubert and National Space Institute, Technical University of Denmark for the access to cloud-to-ground lightning data from the Eurosprite campaigns 2012–2014.

References

Arnone, E., J. Bór, O. Chanrion, V. Barta, S. Dietrich, C.-F. Enell, T. Farges, M. Füllekrug, A. Kero, R. Labanti, A. Mäkelä, K. Mezuman, A. Odzimek, M. Popek, M. Prevedelli, M. Ridolfi, S. Soula, D. Valeri, O. van der Velde, Y. Yair, F. Zanotti, P. Zoladek, and T. Neubert (2020), Climatology of Transient Luminous Events and lightning observed above Europe and the Mediterranean Sea, *Surv. Geophys*. **41**, 2, 167–199, DOI: 10.1007/s10712-019-09573-5.

Bedka, K., J. Brunner, R. Dworak, W. Feltz, J. Otkin, and T. Greenwald (2010), Objective satellite-based detection of overshooting tops using infrared window channel brightness temperature gradients, *J. Appl. Meteorol. Clim.* **49**, 2, 181–202, DOI: 10.1175/2009JAMC2286.1.

Bór, J. (2013), Optically perceptible characteristics of sprites observed in Central Europe in 2007–2009, *J. Atmos. Sol.-Terr. Phys*. **92**, 151–177, DOI: 10.1016/j.jastp.2012.10.008.

Bór, J., G. Sátori, and H.D. Betz (2009), Observation of TLEs in Central Europe from Hungary supported by LINET, *AIP Conf. Proc*. **1118**, 1, 73–83, DOI: 10.1063/1.3137716.

Bór, J., Z. Zelkó, T. Hegedüs, Z. Jäger, J. Mlynarczyk, M. Popek, and H.D. Betz (2018), On the series of +CG lightning strokes in dancing sprite events, *J. Geophys. Res.: Atmos*. **123**, 19, 11030–11047, DOI: 10.1029/2017JD028251.

Carey, L.D., M.J. Murphy, T.L. McCormick, and N.W.S. Demetriades (2005), Lightning location relative to storm structure in a leading-line, trailing-stratiform mesoscale convective system, *J. Geophys. Res.: Atmos*. **110**, D3, D03105, DOI: 10.1029/2003JD004371.

Glickman, T. (2000), *Glossary of Meteorology*, 2nd ed., American Meteorological Society, Boston.

Iwański, R., A. Odzimek, L.B.N. Clausen, V. Kanawade, I. Cnossen, and N.J.T. Edberg (2009), Meteorological study of the first observation of red sprites from Poland, *Acta Geophys*. **57**, 3, 760–777, DOI: 10.2478/s11600-009-0008-7.

Lang, T.J., W.A. Lyons, S.A. Rutledge, J.D. Meyer, D.R. MacGorman, and S.A. Cummer (2010), Transient luminous events above two mesoscale convective systems: Storm structure and evolution, *J. Geophys. Res.: Space Phys*. **115**, A5, A00E22, DOI: 10.1029/2009JA014500.

Lu, G., S.A. Cummer, J. Li, L. Zigoneanu, W.A. Lyons, M.A. Stanley, W. Rison, P.R. Krehbiel, H.E. Edens, R.J. Thomas, W.H. Beasley, S.A. Weiss, R.J. Blakeslee, E.C. Bruning, D.R. MacGorman, T.C. Meyer, K. Palivec, T. Ashcraft, and T. Samaras (2013), Coordinated observations of sprites and in-cloud lightning flash structure, *J. Geophys. Res.: Atmos*. **118**, 12, 6607–6632, DOI: 10.1002/jgrd.50459.

Lyons, W.A. (1994), Characteristics of luminous structures in the stratosphere above thunderstorms as imaged by low-light video, *Geophys. Res. Lett*. **21**, 10, 875–878, DOI: 10.1029/94GL00560.

Lyons, W.A. (2006), The meteorology of Transient Luminous Events – an introduction and overview. **In:** M. Füllekrug, E.A. Mareev, and M.J. Rycroft (eds.), *Sprites, Elves and Intense Lightning Discharges*, NATO Science Series II, Vol. 225, Springer, Dordrecht, 19–56.

Lyons, W.A., E.C. Bruning, T.A. Warner, D.R. MacGorman, S. Edgington, C. Tillier, and J. Mlynarczyk (2020), Megaflashes: Just how long can a lightning discharge get?, *Bull. Am. Meteorol. Soc.* **101**, 1, E73-E86, DOI: 10.1175/BAMS-D-19-0033.1.

Novák, P., and H. Kyznarová (2011), Climatology of lightning in the Czech Republic, *Atmos. Res*. **100**, 4, 318–333, DOI: 10.1016/j.atmosres.2010.08.022.

Odzimek, A., and M. Mielniczek (2022), Methodology of estimating time accuracy in TV recordings of sprite lightning observed from Gliwice and Świder 2011–2015, *Publs. Inst. Geoph. PAS* **D-77 (442)**, 71-83, DOI: 10.25171/InstGeoph_PAS_Publs-2022-026 (this issue).

Odzimek, A., and M. Pajek (2016), Support for sprite optical observations by near real-time analysis of thunderstorm development from satellite overshooting tops images. **In:** *Book of Abstracts: TEA-IS Conference Thunderstorm Effects on the Atmosphere-Ionosphere System, 27–29 June 2016, Copenhagen, Denmark*, Technical University of Denmark, p. 45.

Odzimek, A., L.B.N. Clausen, V. Kanawade, I. Cnossen, N. Edberg, F. Faedi, A. Del Moro, U. Ural, K. Byckling, P. Krzaczkowski, R. Iwanski, P. Struzik, M. Pajek, and W. Gajda (2008), SPARTAN Sprite-Watch Campaign 2007. **In:** V.Ya. Choliy, H. Ivashchenko, and V.N. Ivchenko (eds.), *Proceedings of Contributed Papers, 15th Young Scientists Conference on Astronomy and Space Physics*, Kyivskyi Universytet, Kyiv, 64–67.

Odzimek A., J. Bór, M. Mielniczek, M. Pajek, P. Struzik, and P. Novak (2013), A case study of two sprite events recorded over western Europe. **In:** *EGU General Assembly 2013, 7-12 April 2013, Vienna, Austria*, Geophysical Research Abstracts, Vol. 15, EGU2013-8775-2.

Odzimek A., M. Pajek, J. Bór, P. Struzik, P. Novak, M. Mielniczek, and M. Popek (2014), Optical observations of sprites supported by OST images. **In:** *Book of Abstracts, 22nd Cartographic School "Geoinformatics and Atmospheric Science", 6–9 May 2014, Wałbrzych-Książ, Poland*, University of Wroclaw, p. 47.

Odzimek, A., W. Gajda, M. Pajek, and M. Kubicki (2022), Red sprites over northwest Poland and the southern Baltic coast observed from Świder Geophysical Observatory, *Publs. Inst. Geoph. PAS* **D-77 (442)**, 55–70, DOI: 10.25171/InstGeoph_PAS_Publs-2022-025 (this issue).

Pajek, M., R. Iwanski, M. König, and P. Struzik (2008), Extreme convective cases – the use of satellite products for storm nowcasting and monitoring. **In:** *Proc. 2008 EUMETSAT Meteorological Satellite Conference, Darmstadt, Germany*, 8 pp.

Soula, S., J. Mlynarczyk, M. Füllekrug, N. Pineda, J.-F. Georgis, O. van der Velde, J. Montanyá, and F. Fabró (2017), Dancing sprites: Detailed analysis of two case studies, *J. Geophys. Res.: Atmos.* **122**, 6, 3173–3192, DOI: 10.1002/2016JD025548.

Tomicic, M., S. Soula, E. Defer, S. Prieur, J. Mlynarczyk, T. Farges, O. Chanrion, C. Köhn, and T. Neubert (2021), Dancing sprites above a Lightning Mapping Array – An analysis of the storm and flash/sprite developments, *J. Geophys. Res.: Atmos.* **126**, 20, e2021JD035059, DOI: 10.1029/2021JD035059.

Received 16 September 2022
Received in revised form 30 December 2022
Accepted 31 December 2022

Publications of the Institute of Geophysics, Polish Academy of Sciences
Geophysical Data Bases, Processing and Instrumentation
vol. 442 (D-77), 2022, pp. 55-70
DOI: 10.25171/InstGeoph_PAS_Publs-2022-025

Red Sprites over Northwest Poland and the Southern Baltic Coast Observed from Świder Geophysical Observatory

Anna ODZIMEK[1,✉], Wojciech GAJDA[2], Monika PAJEK[3], and Marek KUBICKI[1]

[1]Institute of Geophysics, Polish Academy of Sciences, Warszawa, Poland

[2]Institute of Meteorology and Water Management – National Research Institute, Warszawa, Poland

[3]Institute of Meteorology and Water Management – National Research Institute, Kraków, Poland

✉ aodzimek@igf.edu.pl

Abstract

In 2012–2015, during the peak of thunderstorm season (June–August), night-time optical observations of lightning discharges above storm clouds, called sprites, were conducted from the Geophysical Observatory of the Institute of Geophysics of the Polish Academy of Sciences in Świder (52.115°N, 21.238°E). Dozens of phenomena were recorded above mesoscale convective storm systems located in western and northern Poland, the Baltic Sea, Russia, and Lithuania. Details of the observed events are presented, along with the correlation of optical data with cloud-to-ground and in-cloud lightning recorded by the IMWM-NRI PERUN lightning detection and location system. The analysis concludes with statistics of the observed sprite forms in relation to the associated parent lightning.

Keywords: TLEs, sprites, lightning, PERUN, lightning detection.

1. INTRODUCTION

The phenomena called “red sprites” or in short “sprites” belong to the family of Transient Luminous Events (TLEs) or upper atmosphere lightning. Optically they are short-lived emissions (microseconds to milliseconds) observed during night time. Sprites are mainly produced above stratiform parts of Mesoscale Convective Systems during the mature and decay phase of storm development (e.g., Lyons 2006). Individual events are triggered by the quasi-static electric fields produced in the mesosphere following positive cloud-to-ground (+CG) lightning discharges, sometimes preceded or accompanied by in-cloud (IC) lightning. Extensive or particu-

---

lar IC activity accompanying sprite production has been detected and investigated by, e.g., Lyons (1996), Pineda et al. (2008), Van der Velde et al. (2010, and references therein). The duration, amplitude and waveform of the current of sprite parent lightning play an essential role in the formation of the favourable conditions of sprite onset and development of its streamers through the atmosphere. Different shapes of sprites, such as column or carrot, may be formed (e.g., Stenbaek-Nielsen et al. 2010), with the most simple columnar sprites usually associated with a return stroke current of a +CG, while the more delayed, long-lived, and complex carrot sprites could be related to +CGs with long continuing currents of +CGs (Cummer and Füllekrug 2001; Williams and Yair 2006; Rycroft and Odzimek 2010).

In Europe, first 40 sprites have been scientifically observed in 2000 in the region of the Mediterranean Sea (Neubert et al. 2001). More such observations have been confirmed in the decade from Israel (Ganot et al. 2007), the south of France (e.g., Neubert et al. 2008), at middle latitudes in Central Europe, and as far as from Finland (e.g., Bór et al. 2009; Iwański et al. 2009; Mäkelä et al. 2010). Observations and climatology of the TLEs in Western and Central Europe in 2011–2013 have been recently reviewed by Arnone et al. (2020).

Here we summarise the results of sprite observations from the Geophysical Observatory of the Institute of Geophysics, Polish Academy of Sciences, in Świder, Poland (51.1155°N, 21.2377°E). The most useful directions of optical observations of such phenomena at Świder span from the West to East, giving the possibility of observations of sprite activity of distant (~500 km) storms over western and northern Poland, southern Baltic Sea, and to a lesser extent other Baltic states or Belarus. The main aim of this work is to present details on the collection of the observed events, classify them, identify possible parent lightning and to provide links to where the data will be available for further analysis. Our focus is also on using PERUN, a LF/VHF[1] lightning detection system operated by the Institute of Meteorology and Water Management – National Research Institute (Bodzak 2004; Konarski 2014), and its capabilities in providing lightning data for research investigations of sprites.

2. OPTICAL SPRITE OBSERVATIONS FROM ŚWIDER

The Stanisław Kalinowski Geophysical Observatory of the Institute of Geophysics, Polish Academy of Sciences, is located in Otwock-Świder, about 25 km SE of Warsaw. The observatory was used as a TLE observation site during the thunderstorm seasons of 2012–2015. The view from the main observatory building allowed observations at azimuth range from approximately 270 (West) to 45 (N-East). The mature pine trees surrounding the observatory as well as some observatory instruments are the main obstacles in the field of view. The system was manually switched on and operated when it was technically possible at times when thunderstorms in relevant regions of Poland were occurring and the viewing conditions were favourable.

The observational set-up was similar to those used previously at other locations, as described in, e.g., Odzimek et al. (2008) using a low-light CCD[2] television camera Watec 902H2 Ultimate ½” model, CBC Computar lens H1214FICS model (12 mm, F1/4, ~30° horizontal FOV[3]), except for the latest observations in 2015 when the Computar H0512 model (5 mm, F1/2, ~65° horizontal FOV) was also used. From 2013 onwards a time video overlay unit GPSBOXSPRITE2, equipped with a GPS receiver from The BlackBoxCamera Co Ltd[4] was used for the timing of video fields. The camera was installed on a tripod on the roof of the main

---

[1] Low Frequency/Very High Frequency

[2] Charge-Coupled Device

[3] Field of view (in degrees)

[4] Online at http://www.blackboxcamera.com/pic-osd/pic-osd.htm

observatory building, and it was pointed manually using supporting information on the location of storms from satellite imagery of thunderstorms. For the initial calculation of the azimuth, we have often used the "PanTiltCalc" software created by Lasse Clausen for the observational campaign at Śnieżka Mount (Odzimek et al. 2008), although the azimuth and especially the tilt of the camera had sometimes to be modified because of the obstacles in the field of view. At a change of the position of the camera, the new azimuth has been noted in an auxiliary text file, referred to here as the "camera log". The video signal was analysed by the UFOCapture V2 software from SonotaCo.com[5]. Recommended settings of the UFOCapture programme for the detection of TLEs have been used. The programme recorded detected objects as "peak hold" .jpg images (Fig. 1), video files in .avi format, and other auxiliary files for the use with the UFOAnalysis programme, including selected settings in .xml format. The UFOAnalysis software allows estimation of viewing azimuth from the recorded star field, although such analyses have not been yet completed. TLE detections were approved by visual inspection of peak hold images and movies using the observers' experience. A list of the observed events has been added to the record of observations in an online database at http://private.igf.edu.pl/~aodzimek/tles/database.html.

The events analysed here were observed in the thunderstorm seasons of 2012 to 2015 over June-August. Taking into account information from the observational logs there have been 22 nights of active observations, i.e., not cancelled because of bad weather conditions or other technical obstacles: 7 nights in 2012, 11 nights in 2013, 3 nights in 2014, and 1 night in 2015. Only sprite events have been observed. The results of observations have been summarised in Tables 1 and 2. Table 1 lists the dates of successful observations, viewing directions, time period of sprite occurrence and a number of recorded phenomena counted as the number of events captured (detailed in Table 2). In 29 video recordings 36 events have been recorded. Each event

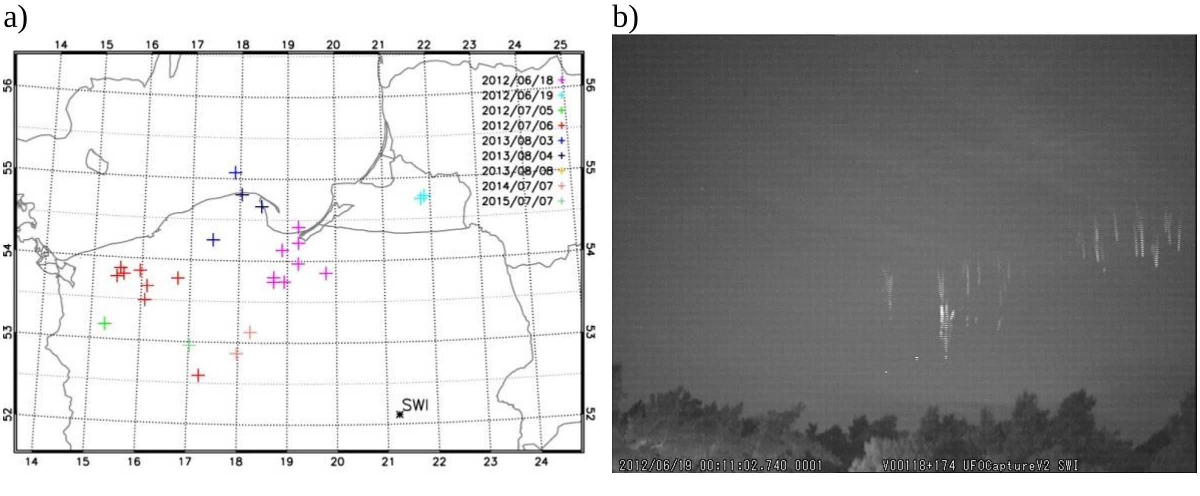

Fig. 1: a) Map of locations of assigned CG parent lightning of sprite events observed on subsequent dates (Table 2); b) example of recorded sprite clusters in Świder on 19 June 2012, ~00:11:03 UTC (peak-hold image). They (Nos. 11–12 in Table 2) consist of two events: one in the centre of the image and one on the right side. The groups are displaced both in space and in time. The sprite group to the right which happened ~300 ms earlier is a cluster of column sprites arranged in what resembles a circle. The event in the middle consists of multiple column sprites and one outstanding carrot or tree sprite.

---

[5] Online at http://sonotaco.com/e_index.html

Table 1

Summary of sprite-lightning observations from Świder over 2012–2015

No.	Date	Main direction of camera view from Świder	Time UTC (sprites observed)	Total event number	Storm location regions	GPS stamp	Time correction [s]
1	2012/06/18-19	NW-N	22:20–00:35	14	Pomerania/Żuławy/ Baltic Sea/Russia	No	+1.00
2	2012/07/05-06	NW	23:25–01:10	11	Pomerania/ Greater Poland	No	–12.60
3	2013/08/03-04	NW-N	23:10–00:30	7	Pomerania/Żuławy/ Baltic Sea	Yes	0
4	2013/08/08	NNE	21:35	1	Lithuania	Yes	0
5	2014/07/07	NWW-W	23:20–23:30	2	Greater Poland	Yes	0
6	2015/07/07	W	22:00	1	Greater Poland	Yes	0

is composed of up to three sprite subevents[6] – single sprites or sprite clusters separated in time or spatially, and within a continuous sequence of frames. In a video recording, a new sequence of sprites, separated from the previous by at least one field, sets a new event.

Most of the sprites have been captured in July, although a relatively small number of events and irregularity of observations prevent us from formulating any firm conclusions on the seasonal occurrence of sprites over the area. The most successful nights of observations were 18–19 June 2012, 4–5 July 2012, and 3–4 August 2013, each characterised by a long-lived MCS in the north or north-west of Poland moving approximately north-east. In order to present the spatial coverage of observations we mapped locations of parent lightning assigned to the observed sprites (see details in next section) in Fig. 1. There were no simultaneous observations of TLEs allowing any triangulation, at least when comparing with observations from the European database (Arnone et al. 2020).

At Świder, sprites could best be observed over regions such as northern Wielkopolska (Greater Poland), Pomorze (Pomerania), Żuławy (Vistula delta), the Bay of Gdańsk, and as far as the Kaliningrad Oblast in the Russian Federation, and parts of Lithuania. The west-northern and northern part of Poland where the sprite-lightning producing storms were located is characterised by a relatively low number of „thunderstorm days" but long-living thunderstorms, such as Mesoscale Convective Systems, occur there resulting in higher thunderstorm activity quantified by, e.g., their duration (Odzimek 2019). In Fig. 2 we show selected satellite observation-based images called „overshooting tops" which map the location of such storms, colour-coded by the brightness temperature differences as measured by the SEVIRI infrared spectral channels at 6.2 μm (water-vapour) and 10.8 μm. These values relatively reflect the vertical development of thunderstorm clouds and such maps have been used in support of sprite observations from Poland (Iwański et al. 2009; Pajek et al. 2008; Odzimek et al. 2014). Sprites are very often observed when the actual overshooting tops diminish or disappear, the storm is mature, or begins to decay. This is reflected in the satellite products when the green and yellow regions of the imaged storm increase their surface area compared with the red and orange regions (Odzimek and Pajek 2016).

---

[6] The subevent sprites can sometimes be of different types, which slightly differs from the definition of sprite entities in Bór (2013).

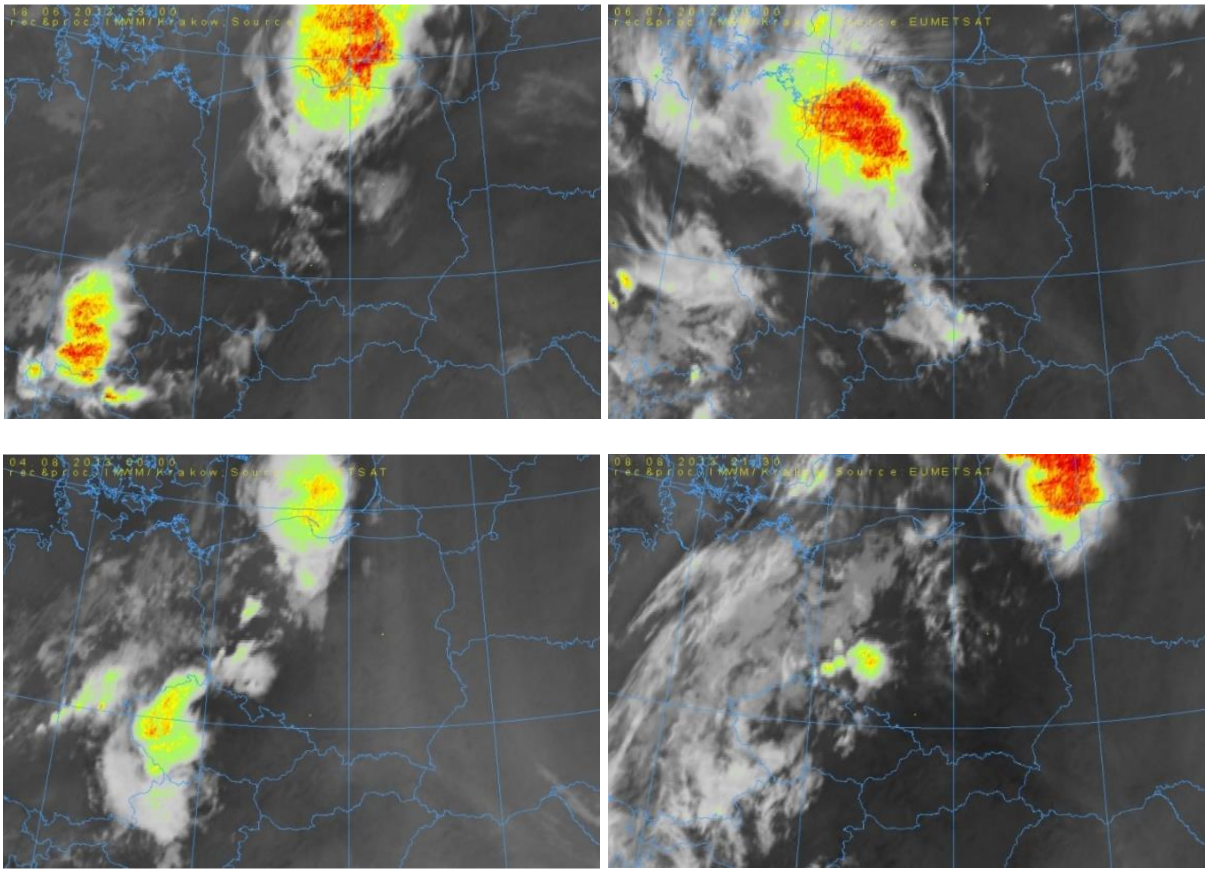

Fig. 2. The “overshooting tops” images of the sprite-producing thunderstorms in northern Poland and Baltic Sea region. Top left: 18 June 2012, 23:00 UTC; top right: 5 July 2012, 00:00 UTC; bottom left: 4 August 2013, 00:00 UTC; bottom right: 8 August 2013, 22:00 UTC (if many sprites observed this is approximately in the middle of the sprite production period by the storm).

Table 2 shows the details of the observed sprites such as time, duration, and the sprite type, as well as assigned parent lightning from detections by the Polish national lightning detection system PERUN. The timing and necessary time corrections have been determined according to the rules described in Odzimek and Mielniczek (2022, this issue). In the case of the recordings from two nights (18–19 June 2012 and 5–6 July 2012), when GPS timing was not available, a time correction has been found, based on PERUN data, in cases supported by detections from the Eurosprite lightning database (courtesy of Torsten Neubert). The correction values rounded to 0.05 s are indicated in the last column of Table 1.

Lightning occurrences have been studied compared to the corrected times of sprite events. In many cases, the occurrence of parent positive +CG lightning has been confirmed, and in many more cases the events were preceded by a more complex lightning sequence, including IC lightning. For any event, a parent lightning has been assigned from those detected in the time range of 100 ms before the first field of the event till the end of last field of the event plus the error of the time of the first (last) field resulting from the timing calculations, individual for an event, ranging between 7 and 50 ms (see Table 2). In case when the timing did not come from GPS and a calculated time shift was applied, additional ±50 ms of uncertainty is added to this range from both ends. Especially in cases when the location of thunderstorms where the probability of detection is decreased near the borders of Poland, PERUN used to miss some detections of CG lightning (e.g., Iwański et al. 2009). Therefore, we have also checked CG lightning detections provided by the Météorage/Euclid to support the Eurosprite campaigns (Neubert et

Table 2

Listing of observed sprite events from Świder and their parent lightning recorded by PERUN system (IMWM-NRI)

No.	No. date	No. video	No. event	Sprite sub-event count	Estimated time	Error[7] [ms]	Event description	PERUN Parent IC+CG Information with +CG RS time	PERUN Parent +CG RS current [kA]
1	#1	#1	#1	3	2012/06/18 22:22:32.077-217	50	Cluster of columns Cluster of carrots Cluster of columns in circle	IC, no +CG*	
2		#2	#1	2	2012/06/18 22:24:43.772-872	50	Cluster of columns Single carrot	IC, no CG*	
3			#2	2	2012/06/18 22:24:43.972-44.072	50	Cluster of columns with tendrils Cluster of wishbones with tendrils and spots, jellyfish	IC+CG 22:24:43.937	+92
4		#3	#1	1	2012/06/18 22:26:30.382-422	8	Cluster of columns with tendrils and spots, jellyfish	IC+CG 22:26:30.307	+74
5		#4	#1	1	2012/06/18 22:37:48.916-996	8	Single carrot Cluster of columns	IC+CG 22:37:48.812 22:37:49.001	+9 +12
6		#5	#1	3	2012/06/18 22:53:53.742-842	8	Multiple columns with spots Multiple columns with spots Cluster of columns	no IC or CG*	
7		#6	#1	1	2012/06/18 23:03:12.063-123	8	Multiple columns	IC+CG 23:03:12.132	+125
8			#2	1	2012/06/18 23:03:12.223-263	8	Multiple columns with unrecognized sprite type	+CG 23:03:12.132 23:03:12.289	+125 +92
9		#7	#1	1	2012/06/18 23:13:51.134-154	8	Multiple columns with tendrils	IC, no +CG*	
10	#2	#1	#1	1	2012/06/19 00:05:44.809-869	11	Cluster of carrots in circle	no IC or CG**	

to be continued

---

[7] This is individual error due to time corrections within a recording. Additional 50 ms is to be added in case timing of whole series of events was corrected as detailed in Table 1.

.

Table 2 (continuation)

Listing of observed sprite events from Świder and their parent lightning recorded by PERUN system (IMWM-NRI)

11		#2	#1	1	2012/06/19 00:11:03.318-378	8	Cluster of columns in circle	no IC or CG*,**	
12			#2	2	2012/06/19 00:11:03.678-698	8	Multiple columns with tendrils and spots Single tree	no IC or CG*,**	
13		#3	#1	1	2012/06/19 00:31:15.368-408	8	Cluster of wishbones with tendrils and spots, jellyfish	no IC or CG*	
14		#4	#1	1	2012/06/19 00:37:24.129-169	8	Cluster of carrots in circle	IC, no CG*	
15	#3	#1	#1	2	2012/07/05 23:27:39.653-733	8	Cluster of columns Wishbone sprite with a cluster of columns in circle	IC, no CG*	
16	#4	#1	#1	1	2012/07/06 00:20:27.533-593	8	Cluster of columns and wishbones with tendrils and spots in circle	IC and CG 00:20:27.528	+114
17		#2	#1	1	2012/07/06 00:29:11.622-662	7	Cluster of columns with tendrils	IC, no CG	
18		#3	#1	1	2012/07/06 00:32:41.347-387	8	Cluster of columns with tendrils and spots, jellyfish	IC and CG 00:20:27.528	+169
19			#2	1	2012/07/06 00:32:41.467-507	8	Cluster of sprites of unrecognised type	IC and CG 00:20:27.528	+169
20		#4	#1	1	2012/07/06 00:39:38.994-034	7	Multiple columns with tendrils and spots	IC, no CG*	
21			#2	1	2012/07/06 00:39:38.114-134	7	Cluster of columns	IC, no CG*	
22		#5	#1	1	2012/07/06 00:48:49.488-508	8	Single carrot dancing	no IC, CG* 00:48:49.606	+37
23			#2	2	2012/07/06 00:48:49.608-668	8	Cluster of carrots Cluster of columns	no IC, CG* 00:48:49.785	+18
24		#6	#1	1	2012/07/06 00:58:27.905-925	8	Multiple columns with spots	no IC or CG	

to be continued

Table 2 (continuation)

Listing of observed sprite events from Świder and their parent lightning recorded by PERUN system (IMWM-NRI

25		#7	#1	1	2012/07/06 01:10:16.435-475	7	Cluster of columns	IC+CGs 01:10:16.423 00:10:16.455	+12 +111
26	#5	#1	#1	1	2013/08/03 23:13:55.843-863	0	Cluster of columns and wishbone	no IC, +CG 23:13:55.837	+36
27		#2	#1	1	2013/08/03 23:25:14.157-197	0	Cluster of wishbone and columns	no IC or CG*	
28		#3	#1	1	2013/08/03 23:52:18.242-262	0	Cluster of wishbone and columns	IC, no CG*	
29	#6	#1	#1	1	2013/08/04 00:19:25.707-767	0	Double carrots	IC+CG* 00:19:25.719	+27
30		#2	#1	1	2013/08/04 00:24:18.305-325	0	Multiple columns with spots	IC, no CG*	
31		#3	#1	1	2013/08/04 00:30:38.361-401	0	Double unrecognised types	IC, no CG	
32			#2	1	2013/08/04 00:30:38.441-501	0	Single unrecognised type	IC, no CG	
33	#7	#1	#1	1	2013/08/08 21:38:34.991-35.031	0	Single carrot	no IC or CG**	
34	#8	#1	#1	1	2014/07/07 23:25:23.503-543	0	Cluster of columns with tendrils	IC, no CG*	
35		#2	#1	1	2014/07/07 23:34:29.297-337	0	Cluster of columns with tendrils jellyfish	IC, no CG*	
36	#9	#1	#1	1	2015/07/07 22:01:33.445-465	0	Cluster of columns with tendrils	IC+CG 22:01:33.455	+137
Total				45					

*CG lightning was detected; **Most probably out of the PERUN range.

al. 2008; Arnone et al. 2020). If a +CG was missed by PERUN, but the other was detected, this is indicated by a star note (*). The last column shows amplitudes of the return stroke current of the detected positive CGs. Negative CGs have been excluded from the procedure as being not efficient in sprite lightning production – see, e.g., Lyons (1996), Pineda et al. (2008), Rycroft et al. (2007).

3. PARENT LIGHTNING OF OBSERVED SPRITE EVENTS INCLUDING PERUN INCLOUD DETECTIONS

Since the PERUN system has the ability of detecting the cloud-to-cloud lightning, we have focused our analysis on the properties of the total lightning activity associated with sprite events.

Figures 3a–d show the peak-hold image of selected events and the analysis of position and time sequence of their nominated parent lightning strokes, including CG and IC lightning (here

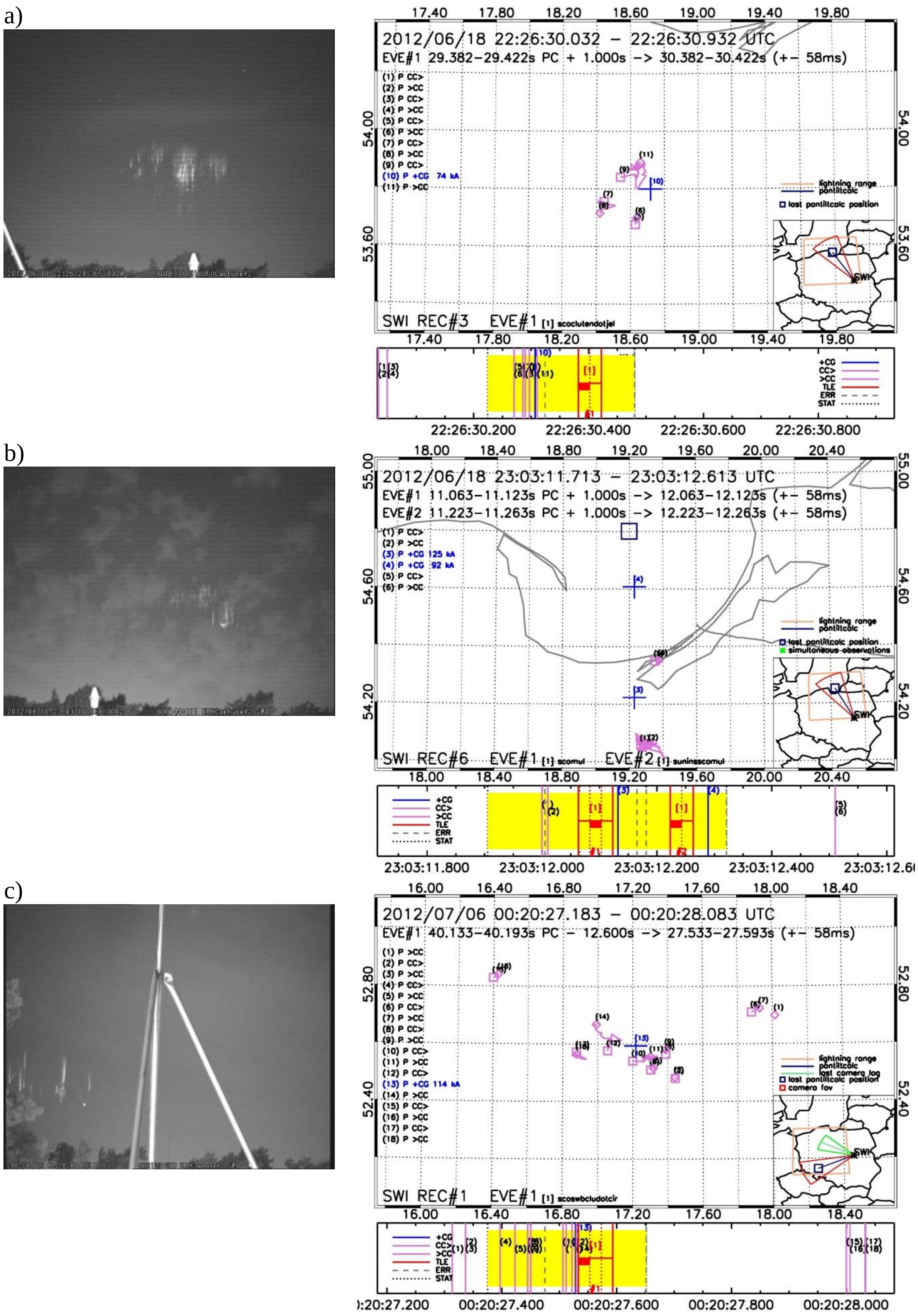

Fig. 3. Continuation on the next page.

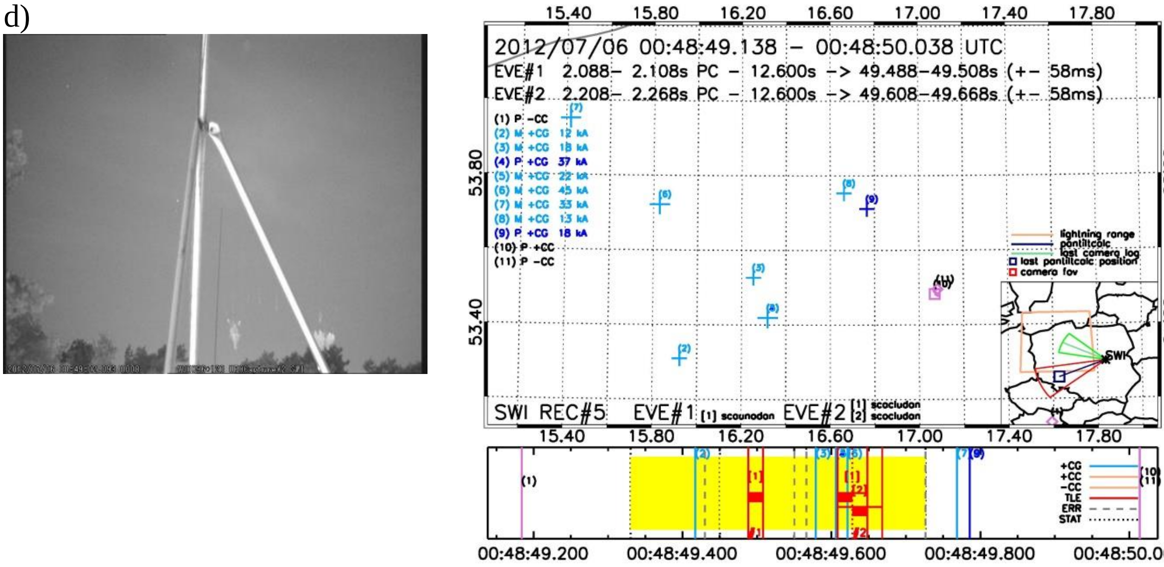

Fig. 3. Peak-hold images (left) of sprites and the mapping and time sequence of lightning (right) at the events: a) 18 June 2012, 22:26:30 UTC, event 4; b) 18 June 2012, 23:03:12 UTC, event 8; c) 6 July 2012, 00:20:27 UTC, event 16; d) 6 July 2012, 00:48:49 UTC, events 22–23. See description in the text.

also denoted by CC – cloud-to-cloud). Each "analysis" figure (panels on the right) consists of the upper and bottom panel. The larger, upper panel shows the map of lightning positions in geographical coordinates near the moment of a sprite capture. The lightning flashes are marked schematically according to their classification by the PERUN system, i.e.: "+" for positive CG lightning, "CC>" outgoing IC lightning, ">CC" incoming IC lightning. The lilac line connects the starting (CC>), intermediate (0CC, not explicitly shown), and final (>CC) points. Since geographical coordinates of all these points were available it was also possible to calculate the distance between the starting and final points of IC lightning along their path, i.e., by following consecutive "0CC" points from a starting point till the final point was encountered. There has been also a category of isolated points; however, these have not been analysed. A statistical count of displayed discharge types is shown in the legend. The detected lightning strokes are also listed chronologically (numbered) on the left side together with all positive CGs highlighted by blue colour (P denotes PERUN detection, M – detection provided by Météorage; CG detections by both systems at the same time (to 10 μs accuracy) are considered as one, and denoted by "<>").

The small map in the bottom right corner includes schematic countries borders, position of the camera (Świder – SWI), the latest used azimuth calculated with PanTiltCalc tool and the field of view of the camera (only the horizontal distance is correct). The last calculated or aimed position (although not always indicating the true direction – see remarks above) is marked by a navy square. This square is also plotted in the big map. A similar direction and "field of view" indication in green colour is the direction as noted in camera logs. The orange contour indicates the spatial cover range of the large map.

The bottom panel shows the time sequence of lightning mapped in the upper panel in the corresponding colour code. In red colour the time range of TV fields (each 20 ms-long) of the recorded sprite events (numbered by #) and their subevents (numbered in []) has been shown. Thick red stripe marks the field of maximum brightness (determined by eye) in the subevent. The dashed grey lines indicate the time error applied before the first field and after the last field, resulting from the inaccuracy of recorded timing. The dotted lines and yellow colour indicates the time interval in which any found lightning can be assigned as parent. The events are also described in the big map, including information on timing, number of recording, event and subevents count with a short description encoded by patchwork messages built from 3-letter codes describing types and features of sprites (explained in Appendix 1).

Results combined from the analysis of each event such as that presented in Fig. 3 allowed to take a closer look at some individual events as well as to make statistics of the events' types and the sprites' most frequent features, dependent on characteristics of their parent lightning. The studied features are related to:

- multiplicity and organisation, e.g., single or dual, multiple, including more organised clusters, specific organised clusters such as in the circle formation (referred to as single, multi or circle in Fig. 4),
- complexity of sprite events defined by having tendrils or being most complex types such as carrot sprites (referred to as complex in Fig. 5).

These are studied against the following parent lightning characteristics:

- CG and IC count,
- mean amplitude of parent CG return strokes,
- the maximum amplitude of parent CG return strokes,
- IC lightning extent (span) measured by the radius of a circle inscribed in the rectangle determined by the most distant points of lightning path from the centre calculated as mean average of geographical coordinates of the lightning,
- IC lightning length measured as the sum of distances between points along a lightning path. If more IC lightning is detected, their lengths are summed up.

Events with no assigned parent lightning have been excluded from the analysis. Statistics of the considered sprite features against parent lightning characteristics are presented in Figs. 4

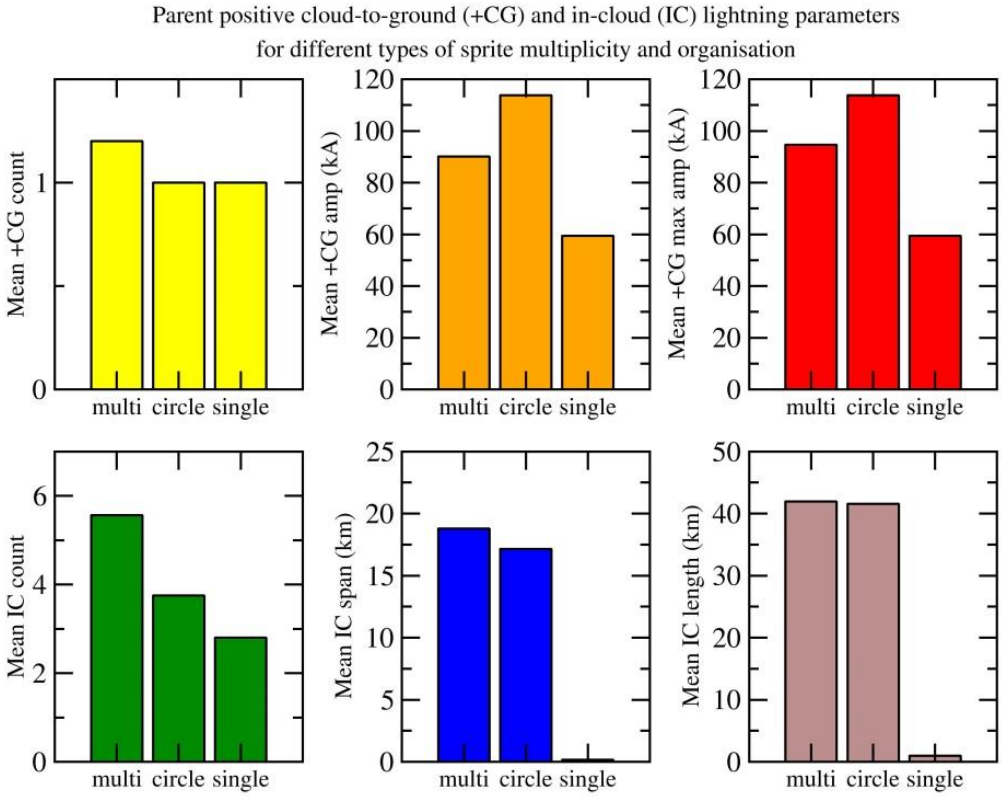

Fig. 4. Statistics of CG and IC parent lightning in relation to sprite multiplicity and organisation.

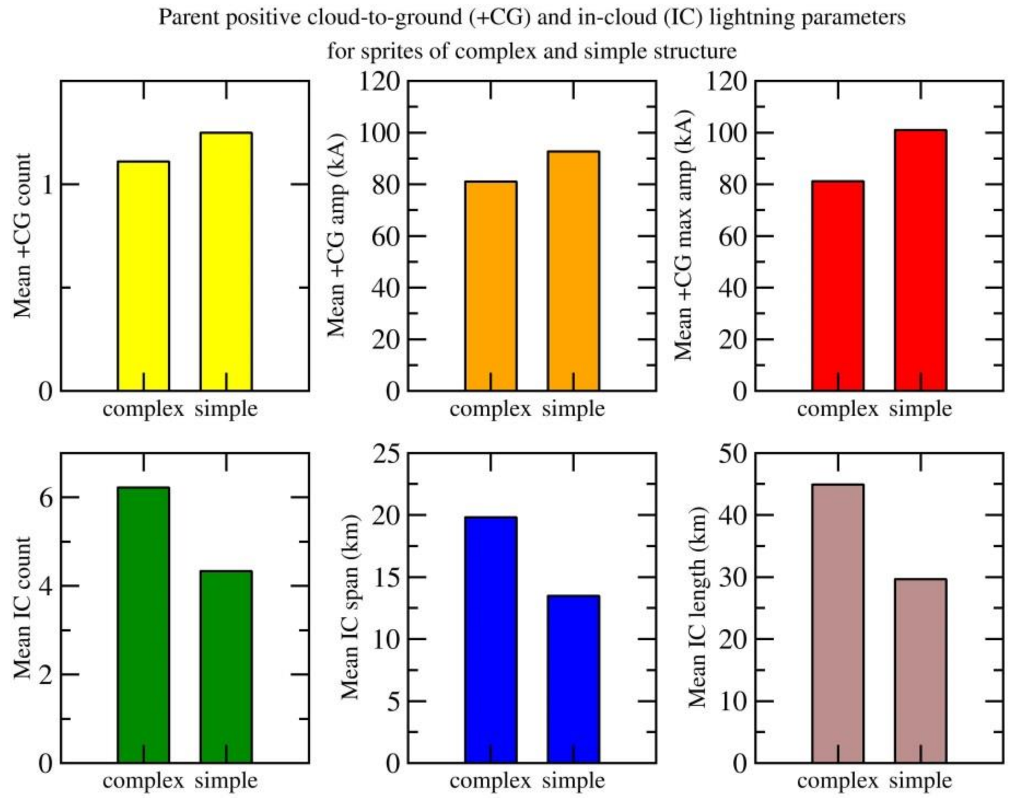

Fig. 5 Statistics of CG and CC parent lightning in relation to complexity of sprite morphology.

and 5, respectively. We do not show statistical errors but the standard deviations are high since the population of events is not very large. The CG statistics are based on PERUN detections only.

4. DISCUSSION

The majority of sprites observed from Świder in northern Poland and beyond over 2012–2015 are column sprites, also named columniform or c-sprites. There is also a significant number of carrot and wishbone sprites. In about 16% of events, sprites are assembled into jellyfish formations[8]. Bór (2013) indicated jellyfish as a common form of sprites over Central Europe as well. One case of dancing sprites event was recorded (6 July 2012, 00:49:02.088-268, Fig. 3d). Approximately 30% of events are mixed events comprising different types of sprites in different organisation, i.e., single sprites or groups of sprites in less or more organised groups and clusters (see Fig. 1). Cluster of different types of sprites may appear simultaneously in the time period equivalent to a single TV frame field, i.e., 20 ms. Multiple-sprite events comprising 2 to 3 sprite subevents can be captured in one sequence of video frames – up to 9 fields equivalent to 180 ms.

Some column sprite clusters seem to be arranged in a circle: about 13% of events. It has been anticipated that this happens around or close to the axis pointing at the parent return stroke position. Optical observations of sprites in Israel during the winters of 2006–2008 have brought a number of such events when the elements of columniform sprites were organised in spaced intervals on the circumference of a circle centred above, or in small offset to the vertical direc-

---

[8] An effect of jellyfish sprite is created by a large cluster of column or wishbone sprites with diffuse tops and long tendrils below.

tion from a positive parent lightning. Furthermore, the time and spatial range of conditions of such geometry, favourable for sprite initiation, has been shown to be possible using the observations and modelling of quasi-static fields following a positive return stroke (Vadislavsky et al. 2009). In our observations, such column sprites ensembles have been observed on 18 June 2012 and 5 July 2012 – events Nos. 1, 11, 16, and 18 (see also Fig. 1). It has to be noted that the circular symmetry of sprite clusters is also observed in case of other sprite type shapes, for example carrots, as in events Nos. 10 and 14. Approximately in 50% of events, sprites are more developed vertically and have tendrils – that includes all jellyfish formations and carrot sprites. Many sprites also produced spots – the bright points over their bodies.

In regard to the statistics made over the sprite morphology and multiplicity characteristics depending on parent lightning, although some parent strokes may have been missed, we note that PERUN provides an opportunity of comparing the sprite features with characteristics of total lightning. As far as sprite multiplicity is concerned, the results from Świder imply that groups or multiple sprites and sprite clusters require more extended IC lightning. In the cases of single sprites, the extent or length of ICs was not such a factor. In addition, for circle-arranged clusters, the large amplitude of the return stroke of parent CG may have been a significant factor. Even though the amplitude of the current flowing in the return stroke (RS max) is not linearly proportional to the total charge moment change, CMC (e.g., Nieckarz et al. 2011), the lightning parameter important for sprite generation (e.g., Huang et al. 1999), the strokes with high RS amplitude and not necessarily large CMC can produce strong quasi-static fields at high altitudes and initiate organised clusters of morphologically developed sprites. Such a dependence of sprites on RS amplitude was observed very early (Wescott et al. 1998). In regard to sprite morphological complexity, more spatially extended IC lightning was associated with more developed sprites such as carrot and jellyfish sprites which have tendrils. However, the appearance of tendrils and spots (analysis not shown), was also a matter of more powerful RSs of parent CG lightning. The results of these simple statistics are generally consistent with both previous observations (e.g., Wescott et al. 1998; Pineda et al. 2008; Van der Velde et al. 2010), and modelling results, including those by Rycroft and Odzimek (2009, 2010). Although column sprites have initially been not associated with large IC activity, in contrast to carrot sprites (Van der Velde et al. 2006), clusters and their jellyfish formations which involve more complicated morphologies may well be. We also note that some IC activity happens within the duration of sprites (i.e., the video fields); however, since many of our observation have no GPS stamps, we refrain from further kind of analyses on the time coincidence or delays between parent IC and CG lightning and sprites, although such analyses are potentially possible. A larger collection of observations with correctly timed events, preferably at higher time resolution, is required to perform more detailed analysis.

5. SUMMARY

The total of 36 TLEs of the “red sprite” type events have been recorded optically between 2012 and 2015 over north-western and northern Poland and the southern Baltic region, from Świder Geophysical Observatory, Poland. Some long-lived storms, such as that on the night of 18–19 June, 5–6 July 2012, and 4–5 July 2013, have been prolific in the production of sprite-lightning. The majority of sprites are of columniform type, with a smaller number of carrot and even fewer sprites of other types. Jellyfish sprite formations are not rare. At least one event of dancing sprites was recorded. PERUN, the Polish lightning detection system operated by IMWM-NRI, provides a valuable opportunity for the investigation of relationships between parent lightning and sprite events, including an analysis of total lightning.

Acknowledgments. This work is supported by subsidies from Poland’s Ministry of Education and Science to the Institute of Geophysics, Polish Academy of Sciences (IG PAS). TLE observations in Świder in 2012–2015 have been supported by earlier Grants of Poland’s Ministry of Science and Higher Education to the Institute of Geophysics, Polish Academy of Sciences, No. 3841/E-41/S/2012, 3841/E-41/S/2013, 3841/E-41/S/2014, and 3841/E-41/S/2015. The camera has been provided for observations from private resources of Anna Odzimek.

We thank Torsten Neubert and the National Space Institute, Technical University of Denmark, for access to lightning data provided by the Météorage and collaborators, used during the Eurosprite campaigns 2012–2014. Anna Odzimek also thanks Mariusz Cieluch SP9HSQ for a consultation on possible sprite parent lightning detection by the Blitzortung.org[9] system in northern Poland.

We acknowledge that the satellite images used during observations have been processed at IMWM-NRI in Kraków branch, in agreement with the EUMETSAT license IMWM/LIC/MSG/10/06 (50002869), and uploaded to a server at the IG PAS. We thank Mariusz Neska of IG PAS for his assistance with making available to us a space on the IG PAS server for this purpose and setting up the upload which continued through the years of observations.

Appendix 1

ABBREVIATIONS OF SPRITE EVENT DESCRIPTIONS IN FIG. 3A–D

sco – column sprite
sca – carrot sprite
swb – wishbone sprite
sun – unrecognised sprite
mul – multiple
clu – cluster
uno – single
cir – circle
ins – inside or next to
ten – tendrils
dot – spots
dan – dancing

References

Arnone, E., J. Bór, O. Chanrion, V. Barta, S. Dietrich, C.-F. Enell, T. Farges, M. Füllekrug, A. Kero, R. Labanti, A. Mäkelä, K. Mezuman, A. Odzimek, M. Popek, M. Prevedelli, M. Ridolfi, S. Soula, D. Valeri, O. van der Velde, Y. Yair, F. Zanotti, P. Zoladek, and T. Neubert (2020), Climatology of Transient Luminous Events and lightning observed above Europe and the Mediterranean Sea, *Surv. Geophys.* **41**, 2, 167–199, DOI: 10.1007/s10712-019-09573-5.

Bodzak, P. (2004), System detekcji i lokalizacji wyładowań atmosferycznych, *Gazeta Obserwatora IMGW* **5**, 11–15.

Bór, J. (2013), Optically perceptible characteristics of sprites observed in Central Europe in 2007–2009, *J. Atmos. Sol.-Terr. Phys.* **92**, 151–177, DOI: 10.1016/j.jastp.2012.10.008.

Bór, J., G. Sátori, and H.D. Betz (2009), Observation of TLEs in Central Europe from Hungary supported by LINET, *AIP Conf. Proc.* **1118**, 1, 73–83, DOI: 10.1063/1.3137716.

---

[9] https://www.blitzortung.org/

Cummer, S.A., and M. Füllekrug (2001), Unusually intense continuing current in lightning produces delayed mesospheric breakdown, *Geophys. Res. Lett.* **28**, 3, 495–498, DOI: 10.1029/2000GL012214.

Ganot, M., Y. Yair, C. Price, B. Ziv, Y. Sherez, E. Greenberg, A. Devir, and R. Yaniv (2007), First detection of transient luminous events associated with winter thunderstorms in the eastern Mediterranean, *Geophys. Res. Lett*. **34**, 12, L12801, DOI: 10.1029/2007GL029258.

Huang, E., E. Williams, R. Boldi, S. Heckman, W. Lyons, M. Taylor, T. Nelson, and C. Wong (1999), Criteria for sprites and elves based on Schumann resonance observations, *J. Geophys. Res.: Atmos*. **104**, D14, 16943–16964, DOI: 10.1029/1999JD900139.

Iwański, R., A. Odzimek, L.B.N. Clausen, V. Kanawade, I. Cnossen, and N.J.T. Edberg (2009), Meteorological study of the first observation of red sprites from Poland, *Acta Geophys*. **57**, 3, 760–777, DOI: 10.2478/s11600-009-0008-7.

Konarski, J. (2014), Validation of cloud-to-ground (CG) lightning flash discriminations obtained from two different lightning data processing programs by the reference E-field recordings. **In:** *Proc. 15th International Conference on Atmospheric Electricity, 15–20 June 2014, Norman, Oklahoma, USA*, 11 pp.

Lyons, W.A. (1996), Sprite observations above the U.S. High Plains in relation to their parent thunderstorm systems, *J. Geophys. Res.: Atmos*. **101**, D23, 29641–29652, DOI: 10.1029/96JD01866.

Lyons, W.A. (2006), The meteorology of Transient Luminous Events – an introduction and overview. **In:** M. Füllekrug, E.A. Mareev, and M.J. Rycroft (eds.), *Sprites, Elves and Intense Lightning Discharges*, NATO Science Series II, Vol. 225, Springer, Dordrecht, 19–56.

Mäkelä, A., T. Kantola, Y. Yair, and T. Raita (2010), Observations of TLEs above the Baltic sea on Oct 9 2009, *Geophysica* **46**, 1–2, 79–90.

Neubert, T., M. Rycroft, T. Farges, E. Blanc, O. Chanrion, E. Arnone, A. Odzimek, N. Arnold, C.-F. Enell, E. Turunen, T. Bösinger, Á. Mika, C. Haldoupis, R.J. Steiner, O. van der Velde, S. Soula, P. Berg, F. Boberg, P. Thejll, B. Christiansen, M. Ignaccolo, M. Füllekrug, P.T. Verronen, J. Montanya, and N. Crosby (2008), Recent results from studies of electric discharges in the mesosphere, *Surv. Geophys*. **29**, 2, 71–137, DOI: 10.1007/s10712-008-9043-1.

Neubert, T., T.H. Allin, H. Stenbaek-Nielsen, and E. Blanc (2001), Sprites over Europe, *Geophys. Res. Lett*. **28**, 18, 3585–3588, DOI: 10.1029/2001GL013427.

Nieckarz, Z., A. Kulak, S. Zieba, and A. Odzimek (2011), Cloud-to-ground lightning dipole moment from simultaneous observations by ELF receiver and combined direction finding and time-of-arrival lightning detection system, *J. Geophys. Res.: Atmos*. **116**, D8, D08107, DOI: 10.1029/2010JD014736.

Odzimek, A. (2019), Spostrzeżenia z obserwacji i modelowania wyładowań elektrycznych nad chmurami burzowymi typu Red Sprite. **In:** J. Ćwiklak (ed.), *Wybrane Aspekty Zabezpieczenia Nawigacji Lotniczej*, Wydawnictwo Lotniczej Akademii Wojskowej (LAW), Dęblin, 49–60 (in Polish).

Odzimek, A., and M. Mielniczek (2022), Methodology of estimating time accuracy in TV recordings of sprite lightning observed from Gliwice and Świder 2011–2015, *Publs. Inst. Geoph. PAS* **D-77 (442)**, 71–83, DOI: 10.25171/InstGeoph_PAS_Publs-2022-026 (this issue).

Odzimek, A., and M. Pajek (2016), Support for sprite optical observations by near real-time analysis of thunderstorm development from satellite overshooting tops images. **In:** *Book of Abstracts: TEA-IS Conference Thunderstorm Effects on the Atmosphere-Ionosphere System, 27–29 June 2016, Copenhagen, Denmark*, Technical University of Denmark, p. 45.

Odzimek, A., L.B.N. Clausen, V. Kanawade, I. Cnossen, N. Edberg, F. Faedi, A. Del Moro, U. Ural, K. Byckling, P. Krzaczkowski, R. Iwanski, P. Struzik, M. Pajek, and W. Gajda (2008), SPARTAN Sprite-Watch Campaign 2007. **In:** V.Ya. Choliy, H. Ivashchenko, and V.N. Ivchenko (eds.), *Proceedings of Contributed Papers, 15th Young Scientists Conference on Astronomy and Space Physics*, Kyivskyi Universytet, Kyiv, 64–67.

Odzimek, A., M. Pajek, J. Bór, P. Struzik, P. Novak, M. Mielniczek, and M. Popek (2014), Optical observations of sprites supported by OST images. **In:** *Book of Abstracts, 22nd Cartographic School "Geoinformatics and Atmospheric Science", 6–9 May 2014, Wałbrzych-Książ, Poland,* University of Wroclaw, p. 47.

Pajek, M., R. Iwanski, M. König, and P. Struzik (2008), Extreme convective cases – the use of satellite products for storm nowcasting and monitoring. **In:** *Proc. 2008 EUMETSAT Meteorological Satellite Conference, Darmstadt, Germany,* 8 pp.

Pineda, N., J. Montanya, O. Van der Velde, and S. Soula (2008), Total lightning in a TLE-bearing winter thunderstorm over the western Mediterranean. **In:** *20th International Lightning Detection Conference, 21–23 April 2008, 2nd International Lightning Meteorology Conference, 24–25 April 2008, Tucson AZ, USA,* 10 pp.

Rycroft, M.J., A. Odzimek, N.F. Arnold, M. Füllekrug, A. Kułak, and T. Neubert (2007), New model simulations of the global atmospheric electric circuit driven by thunderstorms and electrified shower clouds: The roles of lightning and sprites, *J. Atmos. Sol.-Terr. Phys.* **69**, 17–18, 2485–2509, DOI: 10.1016/j.jastp.2007.09.004.

Rycroft, M.J., and A. Odzimek (2009), The impact of lightning flashes and sprites on the earth's global electric circuit: An overview of recent modeling results, *AIP Conf. Proc.* **1118**, 1, 124–135, DOI: 10.1063/1.3137704.

Rycroft, M.J., and A. Odzimek (2010), Effects of lightning and sprites on the ionospheric potential, and threshold effects on sprite initiation, obtained using an analog model of the global atmospheric electric circuit, *J. Geophys. Res.: Space Phys.* **115**, A6, A00E37, DOI: 10.1029/2009JA014758.

Stenbaek-Nielsen, H.C., R. Haaland, M.G. McHarg, B.A. Hensley, and T. Kanmae (2010), Sprite initiation altitude measured by triangulation, *J. Geophys. Res.: Space Phys.* **115**, A3, A00E12, DOI: 10.1029/2009JA014543.

Vadislavsky, E., Y. Yair, C. Erlick, C. Price, E. Greenberg, R. Yaniv, B. Ziv, N. Reicher, and A. Devir (2009), Indication for circular organization of column sprite elements associated with Eastern Mediterranean winter thunderstorms, *J. Atmos. Sol.-Terr. Phys.* **71**, 17–18, 1835–1839, DOI: 10.1016/j.jastp.2009.07.001.

Van der Velde, O.A., Á. Mika, S. Soula, C. Haldoupis, T. Neubert, and U.S. Inan (2006), Observations of the relationship between sprite morphology and in-cloud lightning processes, *J. Geophys. Res.: Atmos.* **111**, D15, D15203, DOI: 10.1029/2005JD006879.

Van der Velde, O.A., J. Montanyà, S. Soula, N. Pineda, and J. Bech (2010), Spatial and temporal evolution of horizontally extensive lightning discharges associated with sprite-producing positive cloud-to-ground flashes in northeastern Spain, *J. Geophys. Res.: Space Phys.* **115**, A9, A00E56, DOI: 10.1029/2009JA014773.

Wescott, E.M., D.D. Sentman, M.J. Heavner, D.L. Hampton, W.A. Lyons, and T. Nelson (1998), Observations of 'columniform' sprites, *J. Atmos. Sol.-Terr. Phys.* **60**, 7–9, 733–740, DOI: 10.1016/S1364-6826(98)00029-7

Williams, E., and Y. Yair (2006), The microphysical and electrical properties of sprite-producing thunderstorms. **In:** M. Füllekrug, E.A. Mareev, and M.J. Rycroft (eds.), *Sprites, Elves and Intense Lightning Discharges,* NATO Science Series II: Mathematics, Physics and Chemistry, Vol. 225, Springer, Dordrecht, 57–83, DOI: 10.1007/1-4020-4629-4_3.

Received 16 September 2022
Received in revised form 30 December 2022
Accepted 31 December 2022

Publications of the Institute of Geophysics, Polish Academy of Sciences
Geophysical Data Bases, Processing and Instrumentation
vol. 442 (D-77), 2022, pp. 71-83
DOI: 10.25171/InstGeoph_PAS_Publs-2022-026

Methodology of Estimating Time Accuracy in TV Recordings of Sprite Lightning Observed from Gliwice and Świder 2011–2015

Anna ODZIMEK[1,✉] and Magdalena MIELNICZEK[2]

[1]Institute of Geophysics, Polish Academy of Sciences, Warszawa, Poland

[2]Gliwice, Poland

✉ aodzimek@igf.edu.pl

Abstract

We present technical details of the TV observations of sprite lightning phenomena made from Gliwice and Świder in 2011–2015, and propose methods of verification and corrections to the recorded timing of individual cases and series of events.

Keywords: TLEs, sprites, observations, timing, GPS, TV.

1. INTRODUCTION

The upper atmospheric lightning, called Transient Luminous Events (TLEs), are effectively observed optically from air and space (Boeck et al. 1998; Mende et al. 2006). Optical methods have also been used in ground-based observations since the first recording by Franz et al. (1990). Low-light television CCD[1] cameras have been employed in various observational systems operated manually or semi-automatically in the US, Japan, France, and other locations all over the world (e.g., Lyons 1994; Allin et al. 2006). Such observations have been made by both researchers, educators, and enthusiasts of TLEs observations, and over the years provided valuable scientific input (e.g., Yamamoto et al. 2010; Arnone et al. 2020; and references therein). High-speed imaging of TLEs emerged also very early (Stanley et al. 1999). In the television (TV) imaging by recording at the standard rate[2], the duration of an event is limited

---

[1] Charge Coupled Device.

[2] The standard rate of televison fields is 1/50 s for CCIR systems and 1/60 s in EIA systems (e.g., Damjanovski 2005). CCIR stands for Committée Consultatif des Radiotelecommuniqué, and EIA stands for Electronics Industry Association. In these standards, two subsequent fields are interlaced producing one frame at the rate equal to twice the field rate.

and bound by the length of one video field (20 ms in a CCIR system). Except when other technical solutions allowed (e.g., Rairden and Mende 1995) the standard rate allows capturing of instances of TLEs, but it is usually not sufficient to image the subsequent phases of the development of these events, which is available through the high-speed imaging. The timing for fields or frames is usually provided by video overlay units cooperating with a timing system supported by global satellite navigation, such as the Global Positioning System (GPS). In the absence of GPS timing, it often relies on the support by Network Time Protocol (NTP) servers.

Accurate timing of the TLE frames imaging is important from the scientific point of view, in order to be able to identify the events' parent lightning (in case of sprites) or, more generally, their absolute or relative position in the sequence of the lightning activity of a thunderstorm, or in relation to other natural or superficial signals, e.g. infrasound or VLF or ELF fields. This kind of research investigations begin very early in TLE research (e.g., Cummer et al. 1998; Rodger 1999; Huang et al. 1999; Neubert et al. 2005; and many others). In the scientific literature, the TLE time moments from TV observations are given most frequently at the resolution of 1 ms as the OSD-GPS devices usually nominally allow, and these times are often devoid of additional information or comment on the timing accuracy and estimation of potential errors. One of the reasons why these issues are not discussed could be that such remarks are considered trivial, or because the scientific infrastructure and recordings are of high quality, and no such problems were detected. Errors may result from failures of the timing system and the satellite navigation, accidental failures of the elements and the recording systems, software, and communication between these elements. Most serious timing issues arise from not using the support of precise timing such as GPS or of dedicated NTP servers, relying on standard PC timing which limits their usefulness in research.

In order to estimate the timing errors for the events recorded from Poland in 2011–2015, performed with and without GPS support, we have recently applied procedures that we describe in this paper in order to give a basis for the understanding of the events' times and errors used in further analysis of the recorded sprite events (Odzimek et al. 2022a,b; this issue). Specifically, based on the information from the timestamps on the recorded video we present a methodology of calculations of the errors in a single recording and a numerical method which can be used to correct the timing of events in case the GPS timing was not working properly. The described timing issues and error calculations are general for TV recordings of any other objects of such short duration.

2. TLE OBSERVATIONAL HARDWARE AND SOFTWARE

An observational hardware set-up for TV observations of TLEs usually consists of a low-light camera and lens, a time overlay unit with a GPS antenna, and a recording computer. The camera used at Gliwice was a monochrome 1/2-inch CCD Watec 902H2 Supreme, and at Świder a Watec 902H2 Ultimate model was used, both with 0.0003 lux sensitivity at F-number 1.4 and 570 horizontal lines resolution. The optical signal was recorded and analysed by the motion capture software UFOCapture (V2) from SonotaCo.com (http://sonotaco.com/e_index.html) which become widely used for TLE observations first in Japan, then in Europe (e.g., Ganot et al. 2007; Yaniv et al. 2009; Bór et al. 2009; Iwański et al. 2009; and others). Video frames were saved at 720×562 pixel resolution.

For the timing, the KIWI-OSD (https://sites.google.com/site/kiwiosd/) on-screen time display unit, equipped with a Garmin GPS antenna, was available for Gliwice observations, and a GPSBOXSPRITE2 unit (https://www.blackboxcamera.com/pic-osd/sprite_faq.htm) was used in observations at Świder from 2013. In Figs. 1 and 2 we show examples of the timestamps on the TV frames from selected sprite recordings from either system. Panels aligned vertically

a) GLC 2012/08/05 20:58:07.413–453 Frame 11

b) SWI 2014/07/07 23:29:33.483–523 Frame 11

GLC 2012:08:05 20:58:07.413–433 field 1 (even)

SWI 2014/07/07 23:29:33.483–503 field 1

GLC 2012:08:05 20:58:07.433–453 field 2 (odd)

SWI 2014/07/07 23:29:33.503–523 field 2

Fig. 1. Examples of TV frames consising of two fields and their relevant on-screen display of PC time by UFOCapture (in the bottom line) and overlaid GPS timing by: a) KIWI-OSD at Gliwice and b) GPSBOXSPRITE-PIC-OSD at Świder. Note that the PC time label is illegible in the video fields due to interlacing.

show one recorded interlaced television frame integrated over 40 ms in total and its two corresponding deinterlaced fields lasting 20 ms each. The example from Gliwice is an event of jellyfish-like sprite which, according to the GPS, occurred on 5 August 2012, between 20:58:07.433 and 20:58:07.453 UTC; the sprite is visible in the second field. Field count is displayed on the right side. The PC time, 20:58:05.818 UTC, is readable only from the frame, and indicates a ~1.5 s time difference from the GPS time. At Świder, the GPS time display used was different – only the time of the field end was indicated. In the example shown in Fig. 1, a cluster of sprites with tendrils is visible in the 11th frame of the video recording from 7 July 2014. The frame was time-stamped with 23:22:26.859 UTC, and its total GPS time range including both fields can be read as 23:29:33.483-523 UTC. The sprites are visible also only in the second, odd field, 23:29:33.503-523 UTC (Fig. 1).

3. ACCURACY AND CORRECTIONS OF TIMING

During the observations over 2011–2015 we have experienced situations when the status of timing of the recorded events varied from unsatisfactory to correct. Below we describe further procedures for the timing verification and corrections depending on whether only PC timing or GPS timing was available. In case there is no GPS timing, a procedure from Section 3.3 can be applied in order to obtain any estimate of the time difference.

3.1 GPS timing

The operating manuals of time overlay units working with GPS signals indicate a maximum of 0.1 ms accuracy of the displayed time, provided the GPS receiver reported the correct fix over several seconds. Most of TLE recordings, however, do not last longer than a second because such longer recordings deliver additional load for the recording system, and because other events may be missed. After any recording, a check on the whole timing of the video fields in a video file, at least prior to an interesting event, is always recommended to verify the timing consistency. Fatal errors are usually also signalled by the device in a specified way described in the manual, and visible in the time-stamps. The KIWI-OSD unit has also a useful feature of displaying a label showing the field count. It is advisable to follow the GPS field count in order to check if any of the fields or whole frames have not been dropped from the recording, as in the example analysed in Section 3.2.2.

3.2 PC timing

When the recording is not timed with the GPS there are ways to assess the time inaccuracy and provide corrections, especially when a series of events is recorded. In such cases, one can relate them to a series of other events whose timing is known, and try to determine the time difference – assuming it may fluctuate but not be changing fast in a monotonic way which would make such correlation impossible or of little use. In the case of sprites, good candidates are events from parallel observations or detections of positive cloud-to-ground (+CG) parent lightning. The observed coincidence of a sprite and its parent lightning which is the critical source of the quasi-static fields required for the sprite initiation is usually high (Boccippio et al. 1995), e.g., in 72 subevents (discrete sprites) recorded by Arnone et al. (2008), only 7 in 38 sprites timed with GPS have not been associated with a parent +CG. Aside from the issue that the efficiency of CG detection may be below 100%, some sprites may be delayed and their relationship with a parent +CG not so evident. Conditions suitable for the initiation of column sprites and sprite halos may appear in just a few milliseconds after parent lightning, and for more spatially developed sprites these are delayed by dozens of milliseconds (e.g., Rycroft and Odzimek 2010). Li et al. (2008; Fig. 3) have determined that between 60% and 70% of discrete events were delayed by less than 20 ms, and 37% by less than 10 ms. In the case of several events, there should be still a few ones on average shortly following their parent lightning in the next 10–20 ms.

Below, in Subsection 3.2.2, we describe a simplified method of estimating a constant value of a time difference, usually valid for a limited period if the departure of the PC time from GPS changes monotonically or irregularly. It is important that before calculating the time shift one needs to verify the consistency of timing in the recording in every single frame or field event, and calculate the corrected timing of the event frames, for example, in the way we propose below, and which we further applied to all recording from Świder and Gliwice.

3.2.1 *Verification of timing and determination of the error of discrete event times*

In a TV recording, the time range of an i-th subsequent frame can be expressed by $<T_i;\ T_i + 1/\mathrm{fps}>$, where T_i is the start time of the video frame, i is the number of the frame in the recording, and fps is the number of frames produced by the camera per second (in PAL system, i.e., with 50 fields per second, fps = 25, so 1/fps = 0.04 s or 40 ms). An event can appear in either both fields of this frame or only the first or second field, further limiting the duration to $<T_i;\ T_i + 1/(2\ \mathrm{fps})>$ or $<T_i + 1/(2\ \mathrm{fps});\ T_i + 1/(\mathrm{fps})>$, as shown in Fig. 1. Thus in a video recording the time (beginning or end of integration) of each frame $\{T_i\}$ can be also expressed by:

$$T_i = T_0 + i/\mathrm{fps},\ i = 1..\mathrm{N}\ . \tag{1}$$

Here we assume that T_0 is defined as such when the set of $\{T_i\}$ refers to the frame beginning. Equation 1 is a linear dependency with the linear coefficient equal to 1/fps. In the UFOCapture programme, each frame has its own timing provided by the PC, e.g., supported by NTP service which denotes a time moment within the frame, depending on the programme settings[3]. In order not to rely on this single value (similarly as in timing with GPS) we recommend to determine a general formula to describe all frames within the recording, i.e., find such a time moment T_0 to which the times of subsequent frames $\{\underline{T}_i\}$ can be related by Eq. 1. Having the whole set of $\{\underline{T}_i\}$ rewritten from the time-stamps displayed on the video frames (such as in the bottom label shown in the uppermost panels of Fig. 1) we can determine T_0 and its error ΔT_0 by the linear regression of pairs $(i,\ \underline{T}_i)$. An example of the regression is shown in Fig. 2. For the estimate of the maximum error of T_0 we find the constants of upper and bottom parallel lines that create a range in which all "PC" time values lie within. Half of this range can be considered as a maximum error and be used instead of the standard deviation of the constant from the regression.

$$\Delta T_0 = 0.5\ |\ \max(\{\underline{T}_i - i/\mathrm{fps}\}_{i\,=\,1..\mathrm{N}}) - \min(\{\underline{T}_i - i/\mathrm{fps}\}_{i\,=\,1..\mathrm{N}})\ . \tag{2}$$

After calculating T_0 from the results of regression using Eq. 1, and its error from Eq. 2, we calculate the start and ending of the i-th frame in the time range $(T_i = T_0 + i/\mathrm{fps},\ T_0 + (i + 1)/\mathrm{fps}) \pm \Delta T_0$.

In the example from Fig. 2, the linear coefficient is 0.0405 s and the constant $T_0 = 20.706$ s. Half of the absolute difference between constants for the upper and bottom boundary lines, 20.703 and 20.710, respectively, i.e., 0.014 s, is set by us as the error of the constant, instead of the standard deviation taken from the regression analysis which in this case is equal to 0.0023 s. An event occurs within frames 11.5–14, which, according to the PC time recalculation by Eq. 1, occur within 23:02:21.166 s and 23:02:21.266 s, ±0.014 s. It is worth noting that when the times $\{T_i\}$ are calculated from Eq. 1, we used the standard rate of fps, independent of what the linear coefficient resulted from the regression, and whether the real rate of the camera slightly differs

---

[3] In the UFOCapture program, the parameter "msec" denotes the offset to the superimposed time.

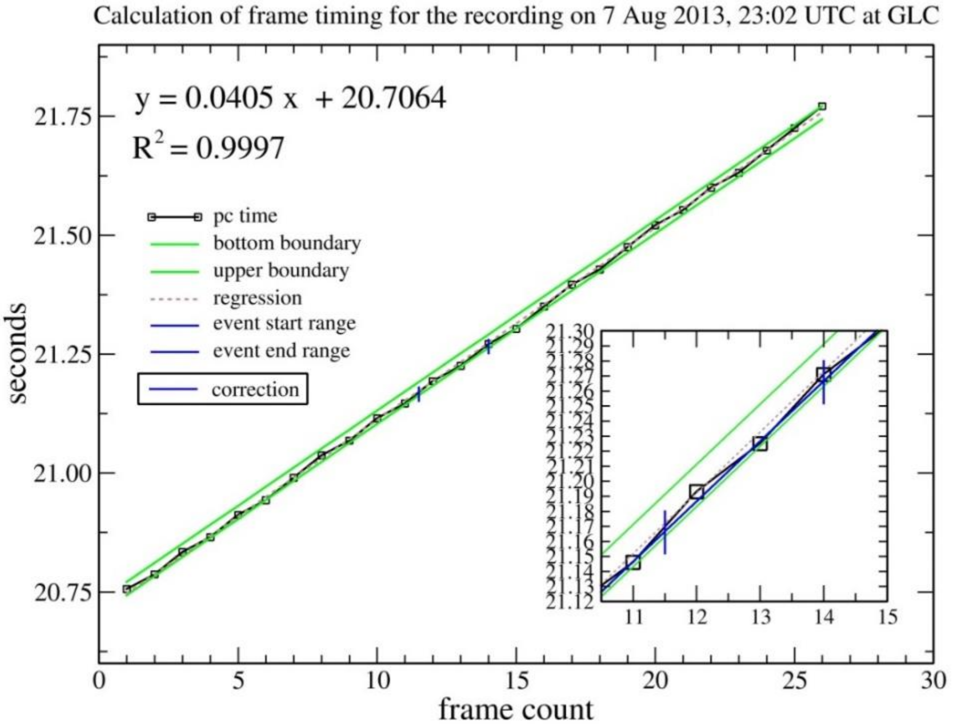

Fig. 2. Results of PC timing recalculation for the video recording from Gliwice on 7 August 2013, ~23:02:22 UTC: a linear regression of PC time records according to Eq. 1, bottom and upper boundary of T_0 error (Eq. 2), regression line, error calculation, and correction with standard fps.

from the standard CCIR fps = 25. For example, the real rate depends on temperature but these changes are rather negligible compared to those we need to take into account when dealing with such time inaccuracy. In the legend to Fig. 2, such calculated series is referred to as the correction.

3.2.2 Missing frames

The above method can be useful providing the numbering of the frames is correct. In order to overcome the issue of missing frames, an examination of any video recording is required, which is an extension to the above procedure and an effective check for missing frames.

Initially, while copying the label values $\{\underline{T}_i\}$, we use counting $\{i\}$ of the frames in the video available from the UFOCapture timestamps (here shown in column 5 in the PC time label), numbered 0001, 0002, 0003, etc. In many recordings, the series of corresponding time labels $\{\underline{T}_i\}$ is a series of time moments separated by ~0.032 s or ~0.047 s, or close to ~0.04 s[4]. If there are no missing frames, a linear regression of these values gives a linear coefficient approximately equal to the value of the fps, ~0.04 s. If this is not the case, we can expect that some frames in the recorded video have been lost. This seems more likely to happen when the recordings are longer or when there are problems with the performance of the system. In case we have a parallel GPS timing, this problem would show also in the GPS timestamps when the receiver updates its timing from the 1PPS[5] signal, not immediately, though. Therefore it is still advisable to check the whole timing of the video frame by frame. Missing frames or fields can easily be revealed by: 1) a linear regression of $\{\underline{T}_\mathrm{i}\}$ giving the linear coefficient larger

---

[4] It happens with the UFOCapture programme when some settings remain that are related to NTSC (default) instead of PAL, such as the time shift of a frame “msec”.

[5] Pulse per second.

Table 1

Example of PC and (KIWI-OSD) GPS timing from the time labels
of the recording on 5 August 2012, ~20:58:07 UTC

	PC timing							GPS timing						
1	2	3	4	5	6	7	8	9	10	11	12	13	14	15
Count	hh	nn	ss	diff	1+ t/fps	New count	Frame diff	hh	nn	ss f1 start	ss f2 end	Field count	Frame diff	Frame count
1	20	58	5.443	0.000	1	**1**	1	20	58	7.013	7.053	234536	1	1
2	20	58	5.490	0.047	2.2	**2**	1	20	58	7.053	7.093	234538	1	2
3	20	58	5.521	0.031	3.0	**3**	1	20	58	7.093	7.133	234540	1	3
4	20	58	5.553	0.032	3.8	**4**	1	20	58	7.133	7.173	234542	1	4
5	20	58	5.600	0.047	4.9	**5**	1	20	58	7.173	7.213	234544	1	5
6	20	58	5.631	0.031	5.7	**6**	1	20	58	7.213	7.253	234546	1	6
7	20	58	5.662	0.031	6.5	**7**	1	20	58	7.253	7.293	234548	1	7
8	20	58	5.709	0.047	7.7	**8**	1	20	58	7.293	7.333	234550	1	8
9	20	58	5.740	0.031	8.4	**9**	1	20	58	7.333	7.373	234552	1	9
10	20	58	5.787	0.047	9.6	**10**	1	20	58	7.373	7.413	234554	1	10
11	**20**	**58**	**5.818**	**0.031**	**10.4**	**11**	**1**	**20**	**58**	**7.413**	**7.453**	**234556**	**1**	**11**
12	20	58	5.850	0.032	11.2	**12**	1	20	58	7.453	7.493	234558	1	12
13	20	58	5.896	0.046	12.3	**13**	1	20	58	7.493	7.533	234560	1	13
14	20	58	5.943	0.047	13.5	**14**	1	20	58	7.533	7.573	234562	1	14
15	20	58	5.975	0.032	14.3	**15**	1	20	58	7.573	7.613	234564	1	15
16	20	58	6.021	0.046	15.5	**16**	1	20	58	7.613	7.653	234566	1	16
17	20	58	6.068	0.047	16.6	**17**	1	20	58	7.653	7.693	234568	1	17
18	20	58	6.131	0.063	18.2	**18**	1	20	58	7.693	7.733	234570	1	18
19	20	58	6.193	0.062	19.8	**20**	2	20	58	7.733	7.773	234572	1	19
20	20	58	6.240	0.047	20.9	**21**	1	20	58	7.773	7.813	234574	1	20
21	20	58	6.287	0.047	22.1	**22**	1	20	58	7.813	7.853	234576	1	21
22	20	58	6.334	0.047	23.3	**23**	1	20	58	7.853	7.893	234578	1	22
23	20	58	6.381	0.047	24.5	**24**	1	20	58	7.933	7.973	234582	2	24
24	20	58	6.428	0.047	25.6	**26**	2	20	58	7.973	8.013	234584	1	25
25	20	58	6.475	0.047	26.8	**27**	1	20	58	8.013	8.053	234586	1	26
26	20	58	6.537	0.062	28.4	**28**	1	20	58	8.053	8.093	234588	1	27
	Frames total 26 \ New frames total 28							**Frames total 27**						

Note: hh – hour, nn – minute, ss – seconds, diff – difference, fps – frames per second, f1 – first (odd) field 1, f2 – second (even) field (frame = two fields). Green colour in PC timing indicates results of enumerating the frames based on elapsed time 1+ t/fps. Incorrect GPS timings and frame counts are indicated in violet colour.

than 1/fps; 2) calculating time passed measured in “1/fps” units, i.e., $t/\text{fps} = 1/\text{fps} \cdot ((\underline{T}_2 - \underline{T}_1) + (\underline{T}_3 - \underline{T}_2) + \ldots + \{\underline{T}_{i+1} - \underline{T}_i\} + \ldots)$; the integer parts of $\{t/\text{fps} + 1\}$ values then indicate to which frame $\{\underline{T}_i\}$ moments theoretically could belong to; 3) by inspection of subsequent $\{\underline{T}_{i+2} - \underline{T}_{i+1}\}$, $\{\underline{T}_{i+1} - \underline{T}_i\}$ and occurrences being greater than 2/fps (in practice, a sequence of several values exceeding 1/fps).

Let us analyse as an example the video recording from Gliwice made on 5 August 2012, at 20:58:07 UTC, shown in Table 1. This video has been timed by both the PC and GPS. The first column, 1, shows the count of frames in this video. Columns 2–3–4 show hour, minute, and second with the fraction of the second extracted from the subsequent PC timestamps. Columns 5-6 show the time difference between the time in timestamps and the time passed, expressed in theoretical frames count equal to $1 + t/\text{fps}$. In frame “18” we encounter the first excess of frame time difference of 0.062, followed by another, 0.063, in frame “19”, next followed by several 0.047 differences, and ending with 0.062. The theoretical frames count ($1 + t/\text{fps}$) clearly indicates that at row “21” there should be frame “22” and the sequence should finish with frame “28”, not “26”. The GPS timing (columns 9–15) also indicated a jump in time at frame “23”, and none at the end of the video, as probably the time has not been updated yet. In such a situation (even if there is no GPS time), we introduce new, corrected count of frames which is entered in column 7. Next, a regression made with the corrected count gives a linear coefficient close to 1/fps, as shown in Fig. 5. In this example there is only one event appearing in frame “11” and by this moment the frame count is correct. The GPS timestamps are present and, in addition to indications by the device, this analysis can be considered as an additional check.

3.2.3 Calculation of time correction using a relation to external events

Finally, we can try to improve the timing by estimating the difference between the current timing of events and events from other, related processes or other recordings. The time shift, Δt, of a series of N (sprite or other) events at times $T_{i\,=\,1..\mathrm{N}}$, in relation to the set of M events at times $T_{j\,=\,1...\mathrm{M}}$, can be estimated numerically using a method of minimisation of the departures of shifted times from the times of the related events. For instance, we may seek such Δt_k, for which the sum of differences between $\{T_i + \Delta t_k\}$ and $\{T_j\}$ is minimal. Let $\Delta t_{k\,=\,-K...K}$ be a set of temporary time shifts over a range between $-K\Delta$ and $K\Delta$ seconds, ±25 s in our case, at a resolution of the order of $\Delta = 10$ ms. Calculations may follow the three steps:

1) For each Δt_k, and $i = 1..\mathrm{N}$, create a table of time differences between translated time moments $\{T_i + \Delta t_k\}$ and each j-th external, related event $j = 1..\mathrm{M}$: $\Delta t_{ijk} = |T_i + \Delta t_k - T_j|$;
2) For each Δt_k, and $i = 1..\mathrm{N}$, find the indexes of the external events for which this time difference $|T_i + \Delta t_k - T_{j,\min}|$ is minimal;
3) Sum up the time differences over $i = 1\ldots\mathrm{N}$, for each Δt_k and find Δt corresponding to the minimum of function S, defined as:

$$S(\Delta t_k) = \Sigma_i\, |T_i + \Delta t_k - T_{j,\min}|\,, \quad \Delta t_k = -K\Delta,..0,..K\Delta\ . \tag{3}$$

The numerical procedure is swifter compared to quite strenuous finding it by trial and error, i.e., by visually comparing a shifted series with related series – which is also effective but slow – and gave very similar indications of the time shifts. In the case when a +CG lightning time series is taken as the related series we can set $\{T_i\}$ not exactly as the start of the first event field but some ~10–20 ms earlier. By using observations where both PC and GPS timing was present we established that a difference of 10 ms used in the procedure recreated the time shift values calculated directly (±0–20 ms). It is also worth noting that this procedure, when applied to GPS-stamped series of events, such as that observed at GLC on 5 August 2012, gave indication of Δt from 0 to 20 ms.

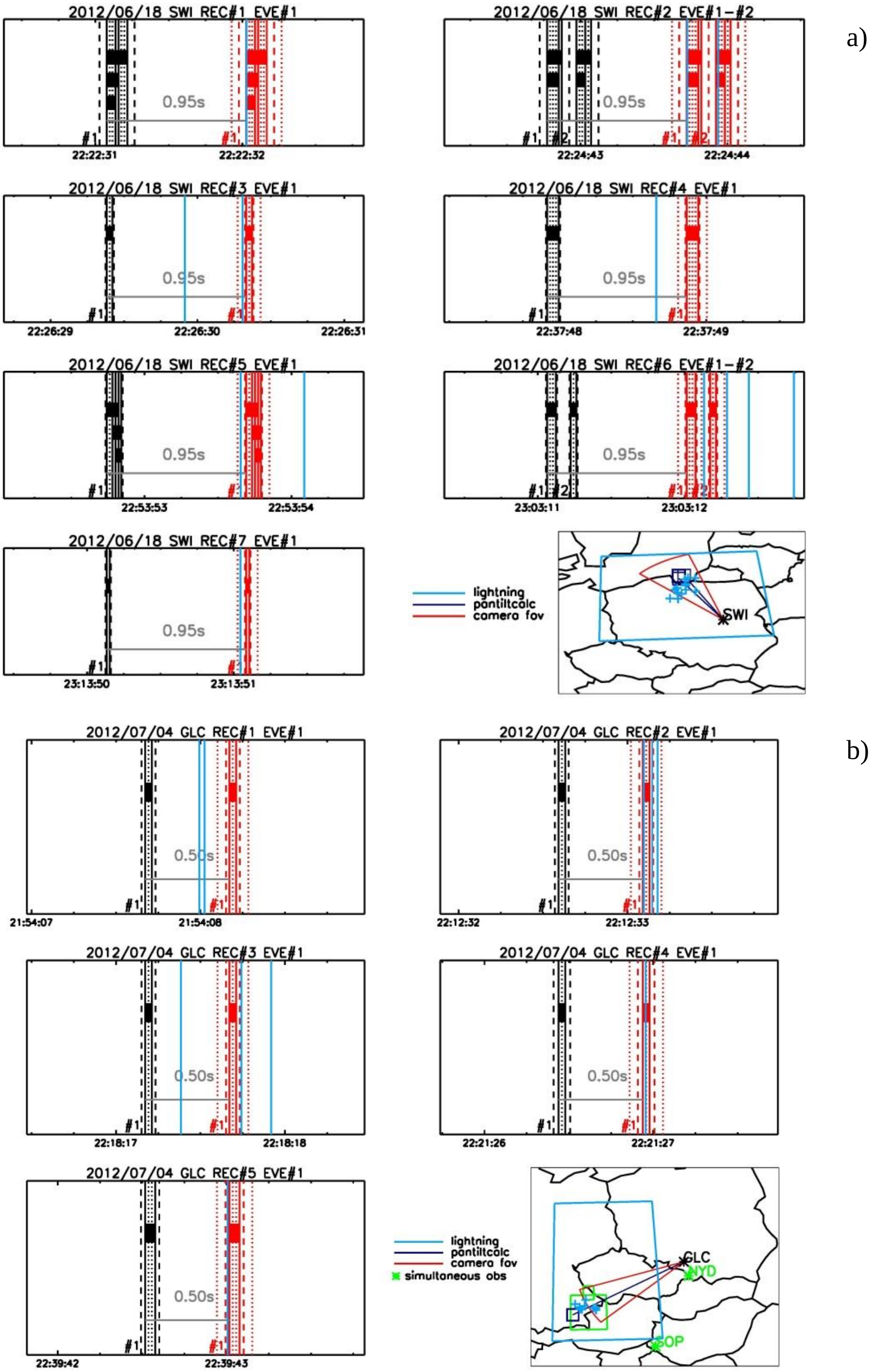

Fig. 3. Results of application of calculated time shifts for a series of sprite events: a) 18 June 2012, Świder (SWI: 7 events between 22:22 and 23:14 UTC); b) 4 July 2012, Gliwice (GLC: 6 events between 21:54 and 23:00 UTC) using +CG times. Black and red lines: times of sprites before and after the time-shift, dashed lines indicate calculated errors, and dotted lines include the 50 ms uncertainty related to the additional translation in time. Light blue lines: time moments of +CG lightning (records courtesy of Torsten Neubert). Grey line and caption: time range between original corrected and translated moments. Map at the bottom shows locations of the +CG lightning displayed in the panels, and the direction and field of view (fov) of the camera based on the aimed calculated azimuth (pantiltcalc) or the azimuth noted in the camera log. Additional camera locations (NYD, SOP) in light green in the map indicate simulataneous observations during this time period and the range of lightning locations (Arnone et al. 2019).

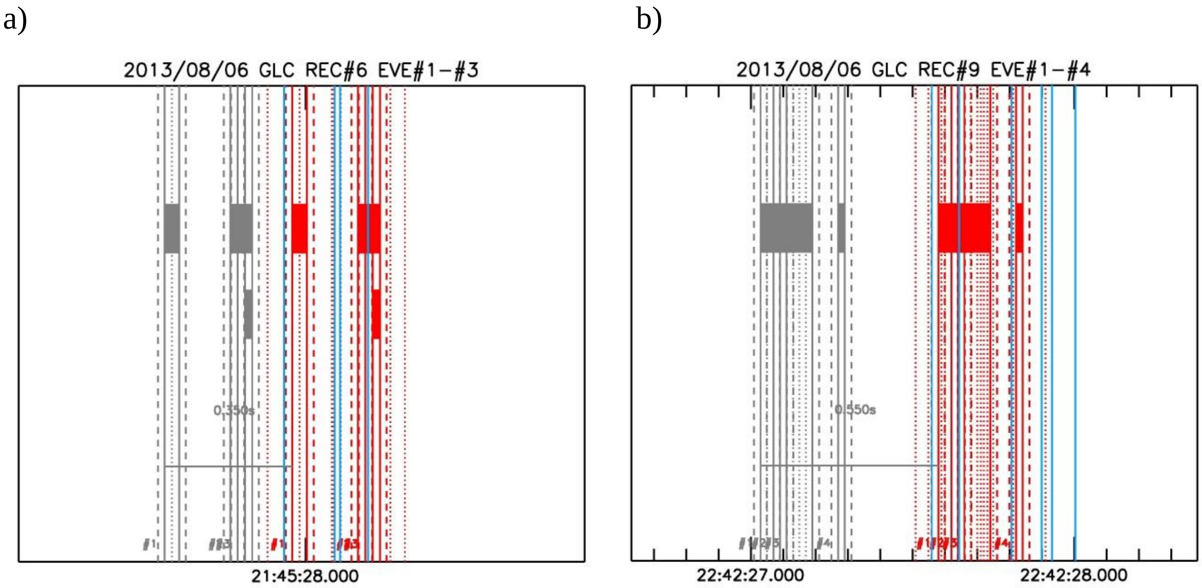

Fig. 4. Results of application of calculated time shifts for two dancing sprite events observed from Gliwice (GLC) on 6 August 2013 at 21:45:27 and 22:42:27 UTC. Description as in Fig. 3, original times indicated by grey lines.

An additional error that needs to be applied after the translation is problematic in the estimate but it is at least of the order of the time step Δ. Accounting also for events which can be delayed we arbitrarily set the final time shift value rounded to the nearest 50 ms and an additional ±50 ms of error (see Figs. 3 and 4).

In the case of events from 18 June 2021, using detections of positive cloud-to-ground lightning as the reference external series, the time correction occurred to be about +0.95 s. In the case of observation of 4 July 2012 from Gliwice, the time shift was estimated at +0.50 s, using all 8 recordings between 21:54 and 22:40 UTC. The results of the time shift are shown in Fig. 3a and 3b, respectively. The time positions of sprites in each recording before and after applying the translation in time are displayed in subsequent panels. Maps attached to panels show locations of lightning displayed in the panels, camera direction and field of view (fov) based on aimed calculated azimuth (referred to as “pantiltcalc”) or a manual camera log. The result seems satisfactory – after application of the time shift all sprites aquire potential parent lightning, and usually no other lightning was detected in the close neighbourhood. The database of the TLE events observed over Western and Central Europe in 2011–2013 by Arnone et al. (2019) indicates that there have been simultaneous observations from Sopron, Hungary, and from Nýdek in the Czech Republic. Observations from Nýdek had no GPS timing, but indicate a consistent difference from the GLC moments of ~3 s (M. Popek, private communication). Other time correction calculations performed for GLC indicated differences in timing on 11 September 2011 by +22.85 s, and on 5 May 2012 by –1.30 s. It is expected that the results of this correction depend on the quality and spatial range of +CG detections; therefore, in our final calculations we also used data from other detection networks[6]. More complicated approach was used for the events of 6/7 August 2013, as discussed below.

---

[6] These corrections have been confirmed by using data from CELDN, and corrections for Świder have been supported by detections from PERUN lightning detections system (Odzimek et al. 2022b; this issue).

4. ANALYSIS OF TIMING OF DANCING SPRITES OF 6–7 AUGUST 2013

Observations made from Gliwice on 6/7 August 2013 turned out to be the most fruitful, with several dancing sprites. Observational reports indicate favourable TLE-producing conditions that lasted for at least ~5 hours (Arnone et al. 2019). Sprite recordings from Gliwice on this night span between 20:20 and 00:20 UTC. In total 48 events were recorded, 20 of which can be grouped into 7 dancing sprite events (Odzimek et al. 2022a; this issue). GPS timing was only available for the first two events between 20:06:58 and 20:24:14 UTC, indicating a ~0.22 s difference between GPS and PC time. The remaining sprites occurred to be recorded in three main time windows: 21:25–22:05, 22:35–23:00, and 23:55–00:20 UTC. Expecting that the time shift may significantly fluctuate over several hours of observations we calculated the time-shift for each of these windows rather than for the whole period. In addition, we made further test calculations by applying the procedure to subsets of sprites in these periods. For example, in 22:35–23:00 UTC these have given consistent time shifts of 0.55 s. In the first period, 21:25–22:05 UTC, they varied between ~–0.10 and +0.35 s. We applied the latter value only to all events occurring after 21:30 UTC in the first period. We note here that before the calculation of the time differences each recording has been analysed as described in Subsections 3.2.1 and 3.2.2, as a correct frame counting is needed for the relative time differences between events appearing in the same video recording to be determined. In Fig. 4 we present the results of the time correction (shift) procedure for the dancing sprite events at 21:45:27–28 and 22:42:27 UTC. The corrected time ranges for the duration of the events from first to last observed are 21:45:27.614–27.854±0.018, and 22:42:27.030–27.290±0.021 UTC, while the corrected and shifted times are 21:45:28.014–28.254±0.068, and 22:42:27.580–27.840±0.071 UTC, respectively. Bór et al. (2018) give the time frames of these events in the ranges: 21:45:27.939–28.199 UTC, and 22:42:27.570–27.836 UTC, so the new values differ by ~0.075 and ~0.010 s, which is comparable to the error. In addition, the GPS timing of one of the sprites observed simultaneously from Sopron at 22:52:17.144–164 UTC (J. Bór, private communication) agrees well with its corrected timing 22:52:17.167–187±0.070 UTC. The corrected times of the observed sprites with their determined errors now enable further analysis of the events.

5. SUMMARY

We have presented a way of verification and correction of the times and time range of sprites observed optically with a TV camera in Świder and Gliwice over 2011–2015. We give details and results of verification of timing within a single recording and the corrections to timing of series of events in the absence of GPS timing. Calculations of errors allow further analysis of the events.

Acknowledgments. This work is supported by subsidies from Poland’s Ministry of Education and Science to the Institute of Geophysics, Polish Academy of Sciences.

We thank Torsten Neubert of National Space Institute, Technical University of Denmark, for the access to cloud-to-ground lightning data for the Eurosprite campaigns 2012–2014 which have been used in our analysis.

References

Allin, T.H., T. Neubert, and S. Laursen (2006), Imaging systems in TLE research. **In:** M. Füllekrug, E.A. Mareev, and M.J. Rycroft (eds.), *Sprites, Elves and Intense Lightning Discharges,* NATO Science Series II: Mathematics, Physics and Chemistry, Vol. 225, Springer, Dordrecht, 101–121, DOI: 10.1007/1-4020-4629-4_5.

Arnone, E., P. Berg, F. Boberg, J. Bór, O.A. Chanrion, C.-F. Enell, M. Ignaccolo, Á. Mika, A. Odzimek, O. van der Velde, T. Farges, S. Laursen, T. Neubert, and G. Sátori (The Eurosprite 2005 team) (2008), The Eurosprite 2005 campaign. **In:** Sandahl I. and J. Arvelius (Eds), *Proceedings of 33rd Annual European Meeting on Atmospheric Studies by Optical Methods,* 28 August – 1 September 2006, Kiruna, Sweden, IRF Sci. Rep., 29–40.

Arnone, E., J. Bór, O. Chanrion, V. Barta, M. Füllekrug, R. Labanti, K. Mezuman, A. Odzimek, M. Popek, S. Soula, D. Valeri, O. van der Velde, Y. Yair, F. Zanotti., and P. Zoladek (2019), *The Eurosprite 2009–2013 Catalogue (Version 1.3),* Zenodo, DOI: 10.5281/zenodo.3480108.

Arnone, E., J. Bór, O. Chanrion, V. Barta, S. Dietrich, C.-F. Enell, T. Farges, M. Füllekrug, A. Kero, R. Labanti, A. Mäkelä, K. Mezuman, A. Odzimek, M. Popek, M. Prevedelli, M. Ridolfi, S. Soula, D. Valeri, O. van der Velde, Y. Yair, F. Zanotti, P. Zoladek, and T. Neubert (2020), Climatology of Transient Luminous Events and lightning observed above Europe and the Mediterranean Sea, *Surv. Geophys*. **41**, 2, 167–199, DOI: 10.1007/s10712-019-09573-5.

Boccippio, D.J., E.R. Williams, S.J. Heckman, W.A. Lyons, I.T. Baker and, and R. Boldi (1995), *Science* **269**, 5227, 1088–1091, DOI: 10.1126/science.269.5227.1088.

Boeck, W.L., O.H. Vaughan Jr., R.J. Blakeslee, B. Vonnegut, and M. Brook (1998), The role of the space shuttle videotapes in the discovery of sprites, jets and elves, *J. Atmos. Sol.-Terr. Phys.* **60**, 7–9, 669–677, DOI: 10.1016/S1364-6826(98)00025-X.

Bór, J., G. Sátori, and H.D. Betz (2009), Observation of TLEs in Central Europe from Hungary supported by LINET, *AIP Conf. Proc.* **1118**, 1, 73–83, DOI: 10.1063/1.3137716.

Bór, J., Z. Zelkó, T. Hegedüs, Z. Jäger, J. Mlynarczyk, M. Popek, and H.D. Betz (2018), On the series of +CG lightning strokes in dancing sprite events, *J. Geophys. Res.: Atmos*. **123**, 19, 11030–11047, DOI: 10.1029/2017JD028251.

Cummer, S.A., U.S. Inan, T.F. Bell, and C.P. Barrington-Leigh (1998), ELF radiation produced by electrical currents in sprites, *Geophys. Res. Lett.* **25**, 8, 1281–1284, DOI: 10.1029/98GL50937.

Damjanovski, V. (2005), *CCTV. Networking and Digital Technology*, 2nd ed., Elsevier Butterworth-Heinemann, Amsterdam, 584 pp.

Franz, R.C., R.J. Nemzek, and J.R. Winckler (1990), Television image of a large upward electrical discharge above a thunderstorm system, *Science* **249**, 4969, 48–51, DOI: 10.1126/science.249.4964.48.

Ganot, M., Y. Yair, C. Price, B. Ziv, Y. Sherez, E. Greenberg, A. Devir, and R. Yaniv (2007), First detection of transient luminous events associated with winter thunderstorms in the eastern Mediterranean, *Geophys. Res. Lett*. **34**, 12, L12801, DOI: 10.1029/2007GL029258.

Huang, E., E. Williams, R. Boldi, S. Heckman, W. Lyons, M. Taylor, T. Nelson, and C. Wong (1999), Criteria for sprites and elves based on Schumann resonance observations, *J. Geophys. Res.: Atmos*. **104**, D14, 16943–16964, DOI: 10.1029/1999JD900139.

Iwański, R., A. Odzimek, L.B.N. Clausen, V. Kanawade, I. Cnossen, and N.J.T. Edberg (2009), Meteorological study of the first observation of red sprites from Poland, *Acta Geophys*. **57**, 3, 760–777, DOI: 10.2478/s11600-009-0008-7.

Li, J., S.A. Cummer, W.A. Lyons, and T.E. Nelson (2008), Coordinated analysis of delayed sprites with high-speed images and remote electromagnetic fields, *J. Geophys. Res.: Atmos.* **113**, D20, D20206, DOI: 10.1029/2008JD010008.

Lyons, W.A. (1994), Characteristics of luminous structures in the stratosphere above thunderstorms as imaged by low-light video, *Geophys. Res. Lett.* **21**, 10, 875–878, DOI: 10.1029/94GL00560.

Mende, S.B., Y.S. Chang, A.B. Chen, H.U. Frey, H. Fukunishi, S.P. Geller, S. Harris, H. Heetderks, R.R. Hsu, L.C. Lee, H.T. Su, and Y. Takahashi (2006), Spacecraft based studies of Transient Luminous Events. **In:** M. Füllekrug, E.A. Mareev, and M.J. Rycroft (eds.), *Sprites, Elves and Intense Lightning Discharges,* NATO Science Series II: Mathematics, Physics and Chemistry, Vol. 225, Springer, Dordrecht, 123–149, DOI: 10.1007/1-4020-4629-4_6.

Neubert, T., T.H. Allin, E. Blanc, T. Farges, C. Haldoupis, Á. Mika, S. Soula, L. Knutsson, O. van der Velde, R.A. Marshall, U. Inan, G. Sátori, J. Bór, A. Hughes, A. Collier, S. Laursen, and Ib L. Rasmussen (2005), Co-ordinated observations of transient luminous events during the EuroSprite2003 campaign, *J. Atmos. Sol.-Terr. Phys.* **67**, 8–9, 807–820, DOI: 10.1016/j.jastp.2005.02.004.

Odzimek, A., M. Mielniczek, M. Pajek, and P. Novák (2022a), Red Sprites over thunderstorms in Czech Republic, Germany and Poland, observed from Gliwice in 2011–2013, *Publs. Inst. Geoph. PAS* **D-77 (442)**, 41–54, DOI: 10.25171/InstGeoph_PAS_Publs-2022-024 (this issue).

Odzimek, A., W. Gajda, M. Pajek, and M. Kubicki (2022b), Red Sprites over northwest Poland and the southern Baltic coast observed from Świder Geophysical Observatory 2012-2015, *Publs. Inst. Geoph. PAS* **D-77 (442)**, 55–70, DOI: 10.25171/InstGeoph_PAS_Publs-2022-025 (this issue).

Rairden, R.L., and S.B. Mende (1995), Time resolved sprite imagery, *Geophys. Res. Lett.* **22**, 24, DOI: 3465–3468, DOI: 10.1029/95GL03332.

Rodger, C.J. (1999), Red sprites, upward lightning, and VLF perturbations, *Rev. Geophys.* **37**, 3, 317–336, DOI: 10.1029/1999RG900006.

Rycroft, M.J., and A. Odzimek (2010), Effects of lightning and sprites on the ionospheric potential, and threshold effects on sprite initiation, obtained using an analog model of the global atmospheric electric circuit, *J. Geophys. Res.: Space Phys*. **115**, A6, A00E37, DOI: 10.1029/2009JA014758.

Stanley, M., P. Krehbiel, M. Brook, C. Moore, W. Rison, and B. Abrahams (1999), High speed video of initial sprite development, *Geophys. Res. Lett.* **26**, 20, 3201–3204, DOI: 10.1029/1999GL010673.

Yamamoto, M.-Y., S. Okamoto, T. Miyoshi, Y. Takamura, A. Aoshima, and J. Hinokuchi (2010), TLE triangulation campaign by Japanese high school students as a space educational project of the SSH Consortium Kochi. **In:** *Proceedings of 38th COSPAR Scientific Assembly, 18–15 July 2010, Bremen, Germany*, PE1-0016-10, 3 pp., SAO/NASA Astrophysics Data System, available from: https://ui.adsabs.harvard.edu/abs/2010cosp...38.3902Y.

Yaniv, R., A.D. Devir, Y. Yair, C. Price, B. Ziv, and N. Reicher (2009), Calibration of CCD cameras for measurements of sprites and elves, *AIP Conf. Proc.* **1118**, 1, 92–98, DOI: 10.1063/1.3137719.

Received 16 September 2022
Received in revised form 30 December 2022
Accepted 31 December 2022

Publications of the Institute of Geophysics, Polish Academy of Sciences
Geophysical Data Bases, Processing and Instrumentation
vol. 442 (D-77), 2022, pp. 85–119
DOI: 10.25171/InstGeoph_PAS_Publs-2022-027

A Novel Application of the Virtual Fujita Scale (VFS) Number Approach as a Useful Tool for Assessment of Lightning Discharges Development and Severity for the Derecho Episode in Poland on 11 August 2017 Together with its Synoptic Context

Jan PARFINIEWICZ[1*,✉], Piotr BARAŃSKI[2,✉], and Michał HERMANOWICZ[3,✉]

[1]Institute of Meteorology and Water Management – National Research Institute, Warsaw, Poland
[2]Institute of Geophysics, Polish Academy of Sciences, Warsaw, Poland
[3]Interdisciplinary Centre for Mathematical and Computational Modelling (ICM),
University of Warsaw (UW), Warsaw, Poland

*retired

✉ Jan.Parfiniewicz@gmail.com
✉ baranski@igf.edu.pl
✉ m.hermanowicz@icm.edu.pl

Abstract

Everyone agrees that the episode of the derecho of 11 August 2017, commonly known as “Suszek”, was the most catastrophic weather event in Poland of the last decade. This case of a rapidly and very fast-moving mesoscale convection system (MCS) is still being analyzed. The current work uses the lightning detection data from the PERUN remote sensing system, which allowed to estimate the electrical activity of such a huge convection system. The primary lightning discharge density is then transformed into the useful scalar parameter, i.e., the predictor characterizing lightning and convection severity of the considered MCS and denoted farther as the virtual Fujita scale (VFS) number. The scrutinized analysis conducted by us presents firstly the detailed mapping of disturbance involved in the MCS propagation path by using the moving filters approach, secondly the area determination of the MCS event development in the form of a mask, and thirdly the analysis of selected aspects of the phenomenology of the MCS occurrence. Such filters make it possible to split the main space domain of the considered convection area into two separated parts of each filter, i.e., its west and east flanks/sides.

A refined analysis and comparison of the aside thunderstorm tracks allowed us to better characterize the development structure of the considered MCS region. In this case, the meteorological context of the MCS episode, i.e., the influence of synoptic background on the course of such a convection, was essential. A better understanding of this violent convective process requires a detailed and complex diagnosis of the complementary and additional information coming from various measurement and database sources, e.g., the ground meteorological measurements, lightning discharges detections and locations, radar and satellite observations together with the relevant model simulations and various severe weather reports. In turn, the used data should be projected/presented in the common and one reference grid. This common reference context was provided by the operational computer simulations at 12:00 and 18:00 GMT of the derecho day expressed by the study of the 3D fields of such parameters as the air pressure, the potential temperature of the tropopause, the air vorticity, the vertical component of air motion and the turbulence air potential. This last was broken down into two components related to the Reynolds and Richardson numbers. The first component represents momentum and is denoted further as PT_{Re} and the second one, relevant to buoyancy and the air flow shear, is denoted by PT_{Ri}. The presented approach allowed for a rational tracking of the evolution of the whole MCS system connected with the derecho episode in Poland.

Keywords: derecho, convection, mesoscale convection system, propagation path, movable filter, lightning location system.

1. INTRODUCTION

Celiński-Mysław and Matuszko (2014) reported and analyzed six cases of the derecho phenomenon that occurred in Poland in 2007–2012. They have found that the regions that were most often affected by the derechos lay in southern and central Poland, but the derecho of “Suszek”, that occurred between 12:40–23:50 UTC on 11 August 2017 and propagated along the SW-NE line was the most disastrous in the last decade, as noted by Taszarek et al. (2019a,b). Among the 6 victims, there were also two girl scouts who died near the site of Suszek, and the case had a court epilogue. During the 10-th European Conference on Severe Storms – ECSS in Kraków, Poland, on 4–8 November 2019, there were at least three poster presentations given by Taszarek et al. (2019a,b), Mazur et al. (2019), and Barański and Parfiniewicz (2019), devoted to the comprehensive analysis of time and space development of different meteorological sources of the “Suszek” derecho incident. This case of a violently and very fast-moving MCS, as shown in the satellite data by Łapeta et al. (2021), is very different from the cases of tornadoes generated by classical, large and slowly moving supercells, reported previously by Parfiniewicz and Barański (2014). Here, the structure of the jet stream, located above the western border of Poland was crucial for supporting the convective system and moving it to the northeast, as was indicated by Taszarek et al. (2019a,b), Mańczak et al. (2021), and Wrona et al. (2022).

In the works mentioned above, the lightning activity of the MCS was not considered at all; therefore, it was advisable to address this issue of lightning activity with greater detail. The operational system of lightning discharge detections PERUN was active during the MCS life time and the PERUN lightning data have supplemented perfectly the radar reflectivity scans of the considered convective system. The detected lightning discharge zones are more compact objects compared to the radar scans of the vast and huge MCS. Hence, such lightning discharge zones may be considered as a kind of compact signature that is more convenient to monitor the MCS’s time and space development. The subject of the presented work was to collect and analyze the data of lightning discharge detections that were gathered during the derecho catastrophic event on 11 August 2017. The carried analysis converts the lightning discharge detections to the so-called virtual Fujita scale (VFS) number. The area changes of the particular

VFS number were used to determine the considered MCS propagation path, its duration and distance traveled, and additionally to indicate also its path split time moment together with this split location.

2. USING OF THE PERUN LIGHTNING DETECTION DATA TO INTRODUCE THE USEFUL SCALAR PARAMETER DENOTED THE SEVERITY DEGREE GENERATED BY MCS EVENTS

PERUN is the Polish name of the French lightning detection and location system called SAFIR (in French: Surveillance et Alerte Foundre par Interférométrie Radioélectrique) that has operated in Poland since 2002. This system enables one to detect and locate atmospheric discharges using the interferometry techniques in the VHF frequency band (Richard and Lojou 1996). Additionally, the low-frequency electromagnetic waves generated by lightning discharges are also analyzed to measure some electrical parameters of these discharges and to discriminate between their types. Such a system mainly uses the arrival signal direction finding (DF) technique to determine the plane locations of lightning sources by the geographical coordinate and distinguishes three groups of detected lightning incidents: the cloud-to-ground flashes by their positive or negative strokes, the intra-cloud lightning discharges by their nodes and the so-called isolated points, i.e., not fully discriminated the flash strokes (Bodzak et al. 2006; Parfiniewicz 2013).

The data from PERUN lightning detection and localization system are transformed into a useful scalar parameter that is characterizing the severity of MCSs or other Extreme Convective Phenomena (ECP). Such a parameter is called Virtual Fujita Scale (VFS) and is similar to some extent to the original Fujita scale (F) postulated by Fujita (1978). On the other hand, Parfiniewicz (2012) proposed some new empirical formulas that enable to transform the primary lightning discharges density field to the relevant VFS parameter/number. Such transformation was based on and validated by the statistical correlation between the occurrence of the severe weather events evaluated in the primary Fujita scale (F) by the SKYWARN POLSKA database and the frequency occurrence of IC (intracloud) or CG (cloud-to-ground) lightning discharges detected and located by the PERUN system and archived in its database. Due to that, two statistical formulas, i. e., F_a and F_b, as a function of lightning discharge densities have been proposed.

The best-fitted formula for the cases of strong ECP events, with the number of lightning discharges (NoL) under the condition that there is at least one return stroke (RS) detection of CG flash and the whole IC lightning discharge detection consists of more than 70 node signals separated in time, is then given by Eq. (1):

$$F_a = a \times (b \times \mathrm{ICs} + c \times \mathrm{ICi})^{1/2} + d \quad , \tag{1}$$

where: $a = 0.047$, $b = 0.7$, $c = 0.3$, $d = 0.22$, and ICs, ICi are measured/expressed in the units (NoL/$\pi \times (15\ \mathrm{km})^2 \times 10$ min). Here ICs denote the number of the first inter-cloud discharge node signals detected by the PERUN as the starting lightning source emission points. ICi is the burst of intermediate lightning emission points showing the whole IC flash event development in 2D.

For less severe convective events, i.e., with $0 < F \leq 2.5$, another formula, that includes both CG (with the number of $\mathrm{RS} > 1$) and IC lightning flash detection data given by ICs number, is expressed by Eq. (2):

$$F_b = a \times [b \times \mathrm{ICs} + c \times \mathrm{RS} + d \times (\mathrm{ICs} \times \mathrm{RS})^{1/2}]^{1/2} \quad , \tag{2}$$

where: $a = 0.088$, $b = 0.624$, $c = 0.112$, $d = 0.264$.

Basing on the calculated value of F_a and F_b, and taking into account the above-mentioned limitations, the resulting convective strength of the considered MCS event is finally evaluated as $[F_0]$ = maximum (F_a, F_b).

This conversion of PERUN lightning detection data was carried out on 7 km × 7 km and 2.8 km × 2.8 km grids, but for each grid mode, any lightning detection points are attributed to their circle surroundings with a radius up to 15 km. It means that, if any PERUN lightning detection points are found in such an area, then the value of lightning discharge density at this site accounts for the number of all lightning discharge locations detected in the circle of 15 km radius surrounding the primary cell of the chosen grid net.

It is worth noting that the relationship between the calculated VFS number and the number of ICs, ICi, and RS obtained from the considered PERUN lightning detection data for the selected VFS threshold level in the range from 1 to 5, depends generally on the used grid model resolution and noted lightning statistics. Here, for the used COSMO (COnsortium for Small-scale MOdeling) _07 km reference grid model and taking into account 10-minute intervals for PERUN lightning detection data during the whole day of 11 August 2017, our exemplary VFS threshold calculations are summarized in Table 1.

Table 1

Relationship between ICs, ICi, and RS number obtained from the PERUN lightning detection data in 10-minute intervals and with the used COSMO_07 km reference grid model, and related to the selected VFS number threshold in the range from 1 to 5

PERUN detection of ICs incidents	PERUN detection of ICi incidents	PERUN detection of RS incidents	Range of VFS number threshold
139.	117.	78.	1.0
636.	361.	233.	2.0
1514.	1036.	347.	3.0
2652.	2073.	590.	4.0
4128.	2839.	1090.	5.0

Such formulas, Eqs. (1)–(2), were also used by Barański and Parfiniewicz (2019) to create a nowcast prediction of severe thunderstorm occurrence connected with the derecho episode in the Bory Tucholskie district on 11 August 2017. This approach was tested in real time by the weather forecasters. It is worth noting that the presented method in this section allowed for efficient and reliable identification of different types of severe convective events, including also tornado incidents.

3. THREE CONVECTIVITY DEVELOPMENT STAGES OF THE DAY WITH THE DERECHO EPISODE

The convective activity of the whole day of 11 August 2017, represented by the density of lightning discharges, is at first divided into three development stages. The analysis, based on Eqs. (1)–(2) given in the previous section, uses 144 patterns of the Virtual Fujita Scale (VFS) number field obtained from the PERUN lightning detection data and recalculated in every 10-minute intervals. By scrolling through them and animating these scans, it is possible to identify these changes that are characteristic of each development stage of the considered MCS. Each of the 3 subjectively identified stages was described by the summary maps of the maximum values of a given parameter that occurred at the given position during that stage. Hence, such maps present electrical activity (EA) expressed by the calculated relevant VFS number and overlapped on the radar reflectivity and the radar-derived precipitation. The radar-derived precipitation was calculated according to the INCA system reported by Szturc et al. (2018) and using the "radar precipitation" formula given by Marshall and Palmer (1948). Thus, such radar-derived precipitation is similar to the primary radar reflectivity data.

Finally, we have divided the considered MCS development from 11 August 2017 into three different phases. The first started before 04:40 UTC and was evaluated as a very strong thunderstorm convection preceding the derecho event. The second lasted from 04:50 to 12:30 UTC and was determined as the intermediate period with two separated thunderstorm episodes and the third one lasted from 12:40 to 23:50 UTC and was connected with the catastrophic gust wind incidents of violent convection that swept over Poland. These differentiated stages are presented in Figs. 1–3, respectively. Let us note, after Mańczak et al.

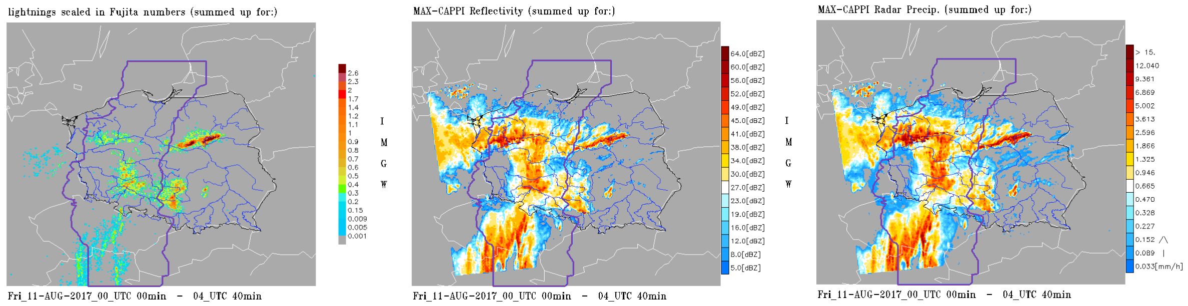

Fig. 1. Three signature maps presenting the first development stage of the considered MCS in the time interval from 00:00 to 04:40 UTC on 11 August 201 by electric activity expressed through fields of VFS number, radar reflectivity, and radar precipitation parameters, respectively, from left to right. The area denoted by the violet line shows the used mask to report/analyze the propagation path of the main MCS part/core during the whole day of 11 August 2017.

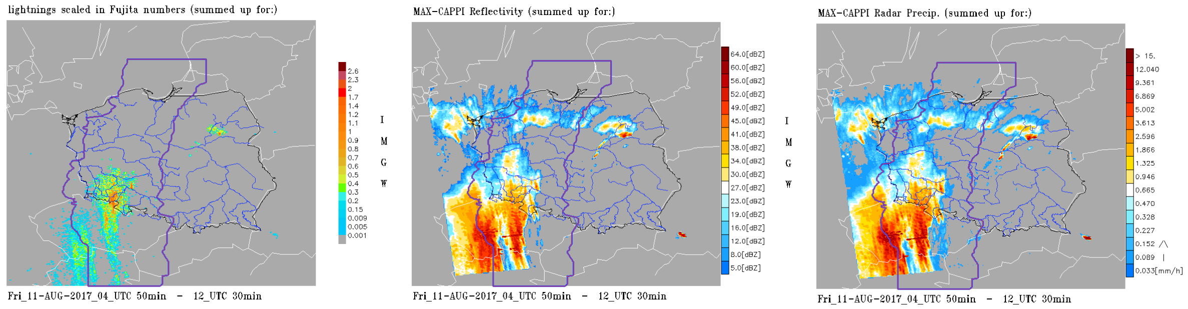

Fig. 2. The same as in Fig. 1, but for the time interval from 04:50 to 12:30 UTC on 11 August 2017, representing the second development stage of the considered MCS with the relevant three signature maps showing the intermediate and moderate thunderstorm activity.

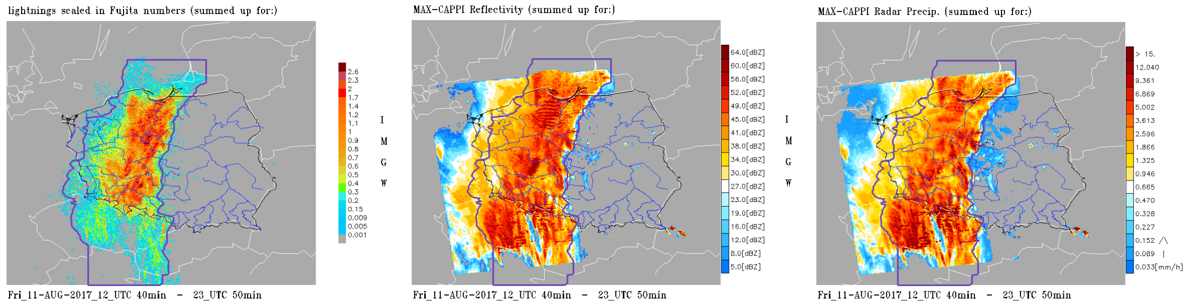

Fig. 3. The same as in Fig. 1, but for the time interval from 12:40 to 23:50 UTC on 11 August 2017, representing the third development stage of the considered MCS with the relevant three signature maps showing the severe thunderstorm activity connected with violent derecho episode.

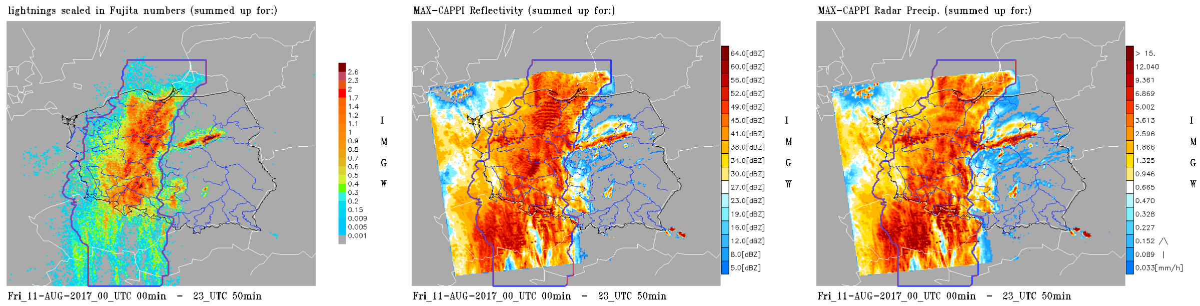

Fig. 4. The same as in Fig. 1, but for the time interval from 00:00 to 23:50 UTC on 11 August 2017 and three collective signature maps summarized this whole day.

(2021) and Wrona et al. (2022), that the first stage was "important for the development of the synoptic situation", which was also confirmed by weather reports from 10 August 2017 09 UTC to 11 August 2017 03 UTC given by the European Severe Weather Database and noted also by Lelątko (2020). In turn, the beginning of the third stage at 12:40 UTC was chosen because then the linear thunderstorm zone from South Bohemia changed the direction of its movement from the SEE-NNW to SSW-NNE. Later, this propagation direction remained unchanged until the end of the considered MCS episode, i.e., until 23:50 UTC.

To better explain the idea of determination of the used area mask to report the propagation path of the main MCS part/core during the whole day of 11 August 2017, the set of three collective signature maps is given in Fig. 4.

4. THE RESULTING MCS PROPAGATION PATH REFINED FOR THE DERECHO EPISODE

In principle, the MCS propagation path can be estimated from the wind trajectory, thunderstorm destruction path, and direct tracking of the movement of thunderstorm cells. Here, the latter idea was applied for the subjectively defined area of the main MCS electrical activity, limiting its range by a horizontal rectangle. The sides of such chosen rectangle coincide with the numerical grid of the operational COSMO model with the grid size of 2.8 km and are presented in Fig. 5. This rectangle is called farther the filter and is defined every 10 minutes according to

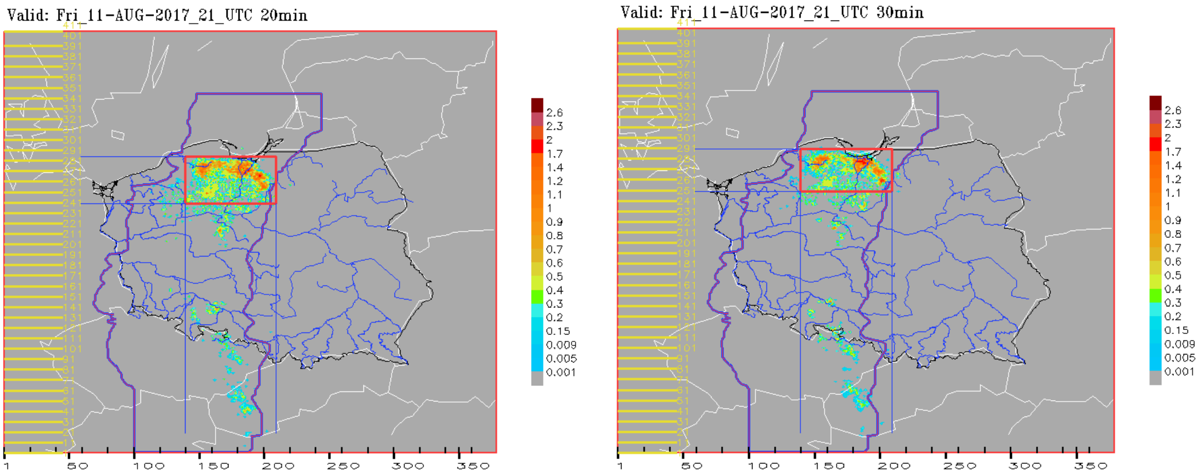

Fig. 5. The scheme presenting the idea of a movable filter as a useful tool that allows to evaluate the current location of the most active disturbance/convective area in relation to the used calculation grid. Here, the COSMO grid 2.8 × 2.8 km was applied. This example concerns two neighboring scans obtained at 21:20 and 21:30 UTC, that are given from left to right, respectively.

the PERUN lightning detection data converted to the relevant VFS numbers. The goal of this approach is to filter out all dispersed lightning discharges located outside the area of their main activity cluster and in order to focus on the impact of these not rejected flashes.

In Fig. 5, the y-axis of the used COSMO grid is parallel to the geographic north-south direction on the meridian of 10 degrees toward the east. Over Poland, the deviation of this axis from this direction does not exceed 10 degrees. Thus, it is sufficient to use the COSMO grid to describe the geographical orientation of the considered MCS propagation path. Moreover, the y coordinates given by the COSMO gird at the sides of the rectangle filter, i.e., ($y_{\min}$, $y_{\max}$), define the instantaneous range of the MCS displacement in this direction. Hence, as the MCS moves northward, these distinguished y coordinates are used to evaluate and monitor the speed of such propagation and to determine the overall impact range of the derecho dislocation/shift.

On the other hand, we define a few useful geometric objects to characterize the extent and structure of the considered MCS. The basic object is a rectangular filter, defined above and covering the entire compact/coherent part of the convection system. This method, denoted the main convective area domain, is assumed to be the geometric "gravity" center derived from the 10-minute VFS number distribution in the area delimited by the used filter. The next considered objects are two parts of this filter, i.e., its west and east sides/flanks. These flanks are the result of dividing the primary filter along the meridian of the COSMO grid passing through the center of "gravity" of the convection system. They also allow that the geometric location of the western and eastern flanks can be determined as the "gravity" centers related to the VFS numbers relevant to such parts of the considered convection system that are co-located, respectively, at its western and eastern side by the used filter. The locations defined in this way, enable us to evaluate the main trajectory of the convection system together with the trajectories of its flanks and to monitor the latitudinal extent of the whole moving system.

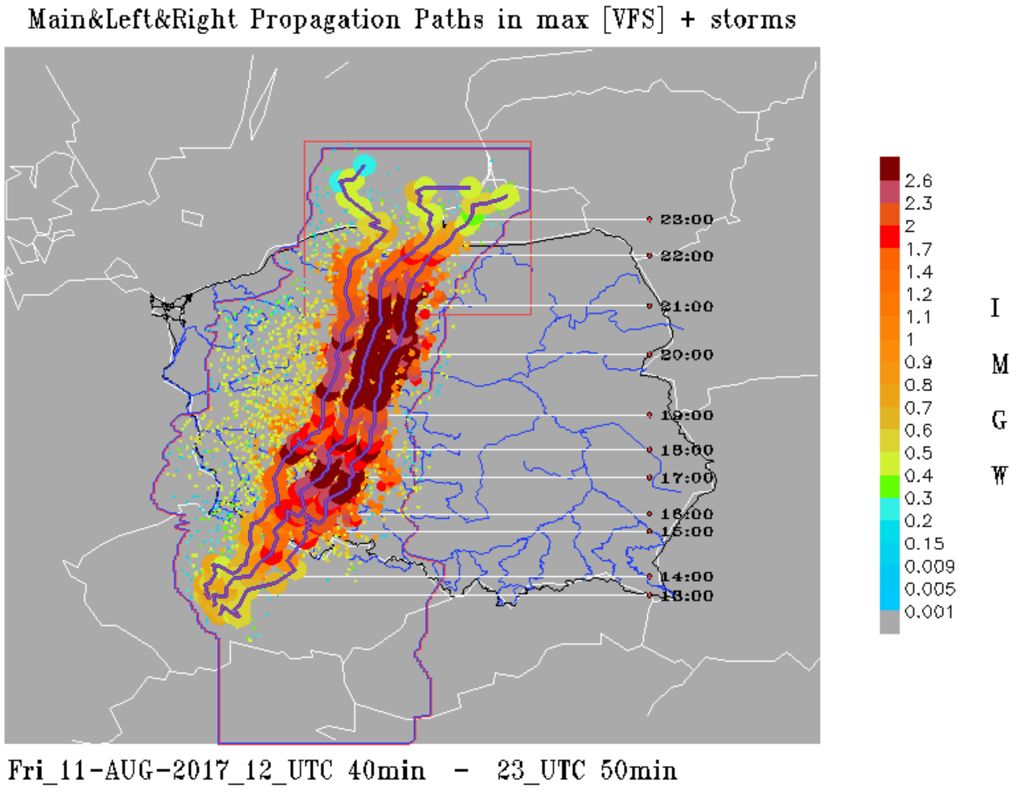

Fig. 6. Evaluation of the left, main, and right propagation paths of the whole considered MCS according to results obtained from the applied movable filter. More detailed description in the text.

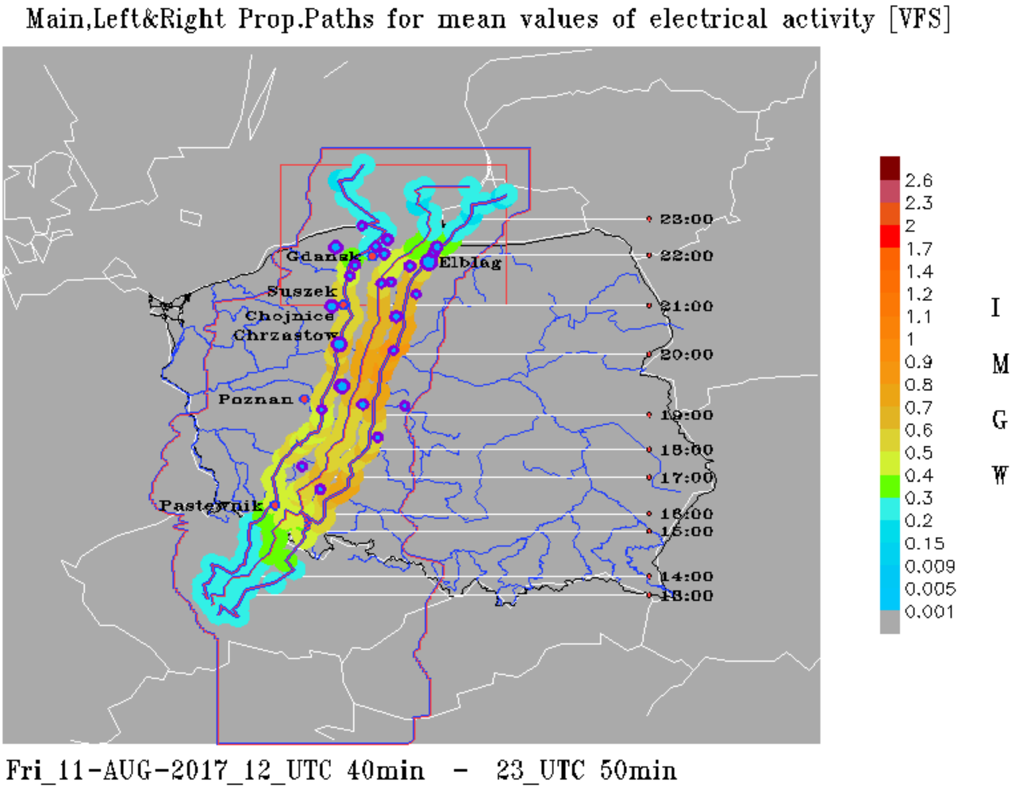

Fig. 7. The same as in Fig. 6, but for the result/change obtained from using the average VFS numbers for performing a movable filter. Blue dots indicated locations where gusts of wind were noted higher than 20 m/s. More detailed description in the text. Small pink dots stand for the Doppler radar locations.

Finally, we have shown in Figs. 6–7 the propagation paths of the whole considered MCS together with its left and right flanks. Figure 6 shows the trajectories superposed on 10-minute maximum VFS numbers for the entire system and its both flanks, respectively. But, in Fig. 7, such trajectories are superposed on the weighted average electrical/lightning activity along the whole system paths.

Figures 8–9 present the evolution of the maximum and spatially averaged VFS, i.e., the maximum of electrical activity for three types of the evaluated propagation paths of the considered convection system: main, western, and eastern. After 15:30 UTC, the time course of such electrical activity for all three types is similar, but around 17:00 UTC and after 20:00 UTC the noted dispersion is most meaningful. The first occurrence of local dispersion maximum at 17:00 UTC can be related to a supercell formation reported by Mańczak et al. (2021) and Wrona et al. (2022), while the second one, after 20:00 UTC and later, is caused probably by a significant detachment of a new thunderstorm cell evolving from the previous main propagation track of the considered convection system.

On the other hand, we can see in Fig. 10 that the eastern propagation path of the considered convection system is practically consistent with its main path throughout the entire analyzed time period and their courses are parallel, indicating similar VFS number changes, whereas the west track is consistent with the main track and together with the eastern track at most until 20:00 UTC. Such a time period ends with the wind gust record of 36.0 m/s in Chrząstów at 20:00 UTC. Let us add that this wind gust value is second in order, after the measurement of 42.2 m/s in Elbląg-Milejewo at 21:40 UTC. However, this maximum recorded wind gust that was noted later on, was related to the right propagation path of the considered convection system.

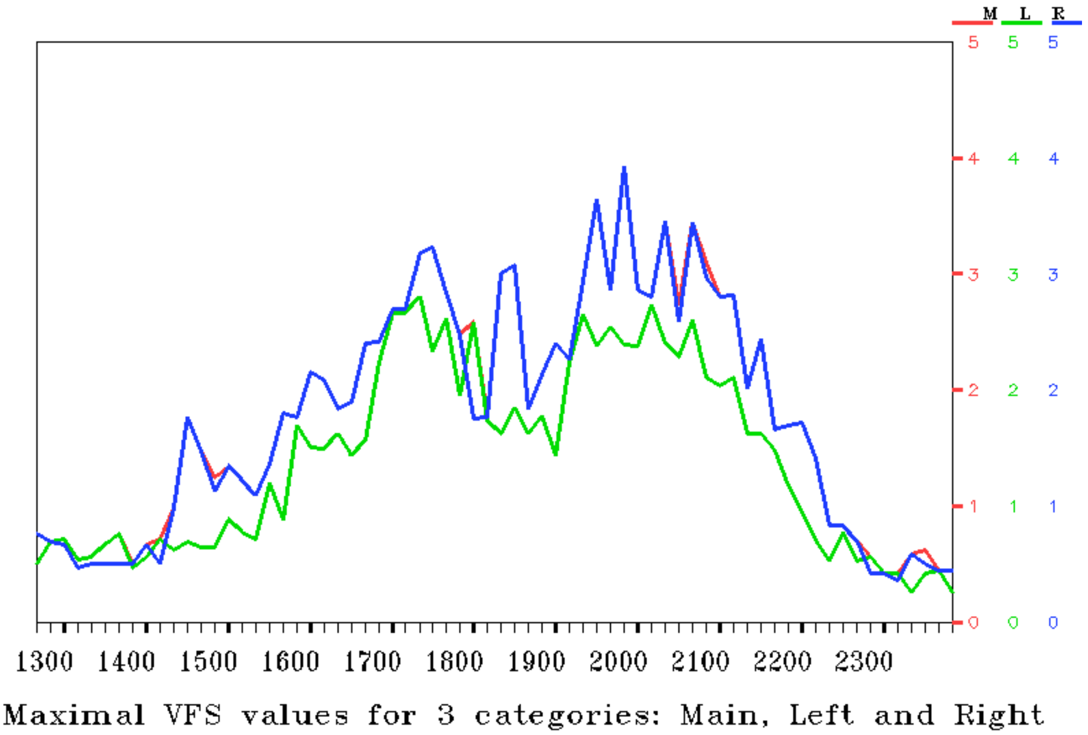

Fig. 8. The time evolution of the maximum VFS number evaluated in the successive windows/slots of the used moveable filter during the propagation paths of the considered convection system: Main (red), Left/west (green), and Right/east (blue). Note that the maximum VFS number for the Main and Right paths practically coincide.

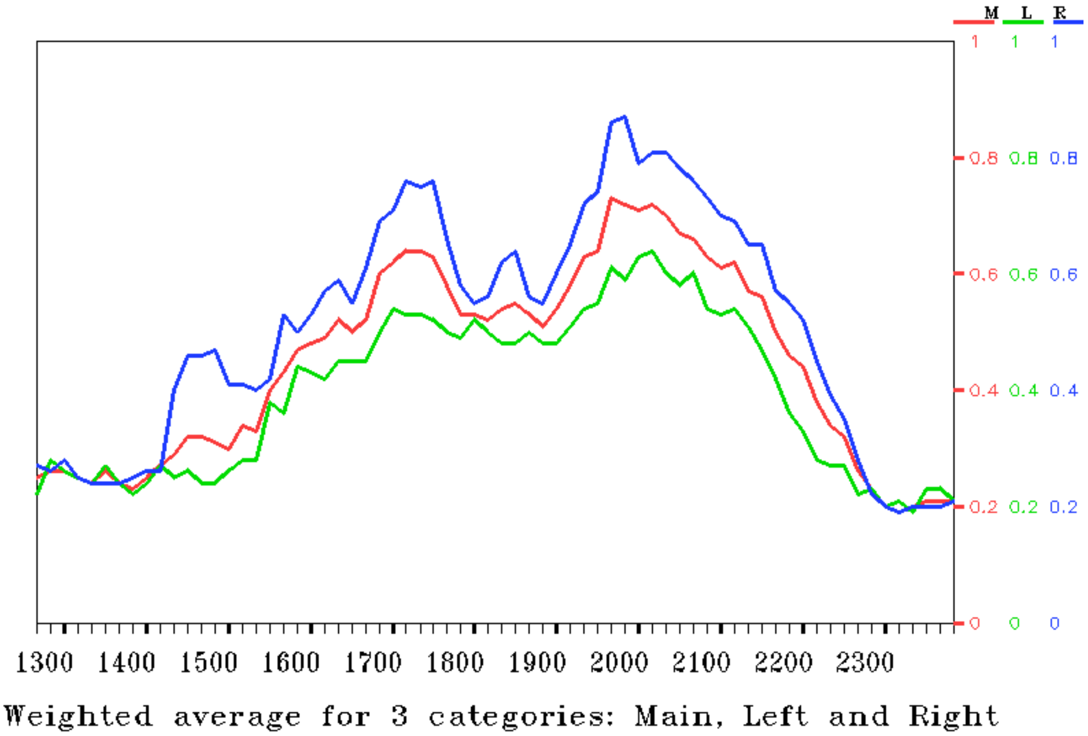

Fig. 9. The same as in Fig. 8, but concerns the time evolution of the spatially averaged VFS number for three types: main, left, and right propagation path of the considered convection system, denoted by red, green, and blue curves, respectively.

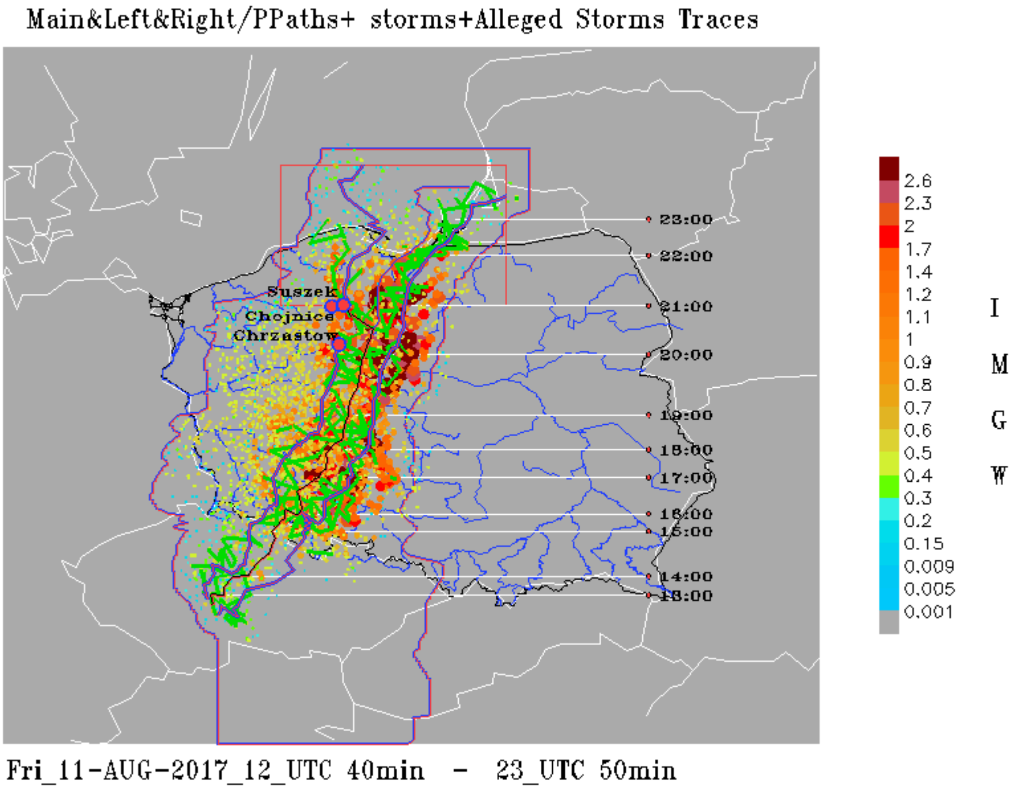

Fig. 10. The same as in Fig. 6, but shows the background of three propagation tracks of the considered convection system marked by blue-purple lines. This background consists of the reduced lightning hot points given by color and size according to the VFS number scale, while visible green lines link the locations with the extremely high VFS number, i.e., lightning hot points noted at the adjacent time terms. Three sites Chrząstów, Chojnice, and Suszek, where the devastating wind gusts have been noted, are indicated by pink circles.

It should be noted that the electrical activity of the western flank of the considered convection system, noted in the time period from 20:00 to 21:00 UTC, deserves a more detailed analysis (see the set of five maps presented in Fig. 11). Focusing on the western part of the system, i.e., the vicinity of Chrząstów, Chojnice, Suszek, and Rytel, we can notice that the electrical activity noted at these sites fluctuates distinctly. At first, it is intense at the exit from Chrząstów, then weakens, reaching the minimum at 20:40 UTC, and 20 minutes later it gains strength in the vicinity of Chojnice, Suszek, and Rytel. Further away, it detaches from the mainstream and advances north, maintaining its strength and distinctiveness. Such analysis of electrical activity changes, given in Fig. 11, can suggest that the westernmost area of the electric activity detaches from the main core of the considered convection system before 21.00 UTC. On the other hand, the re-analysis of the situation given in Figs. 6–7, which has indicated the sharp western bent of the left flank trajectory at 20:40 UTC, suggests that it can be considered as the occurrence of a propagation path splitting for the whole convective system.

We assume that a probable cause of the occurrence of such MCS split at 20:40 UTC is resulted from the additional presence of a mesocyclone system in the considered area and given in Figs. 11–13. Such mesocyclone was also recognized on radar scans by Taszarek et al. (2019a,b) and then analyzed in detail by Łuszczewski and Tuszyńska (2021). In turn, the considered split process was limited territorially by the site locations of Rytel, Suszek, Chrząstów, and Bydgoszcz. However, the range of the Poznań and Gdańsk radars rather does not allow for a detailed reliable analysis of the mesocyclone development in this area. Hence,

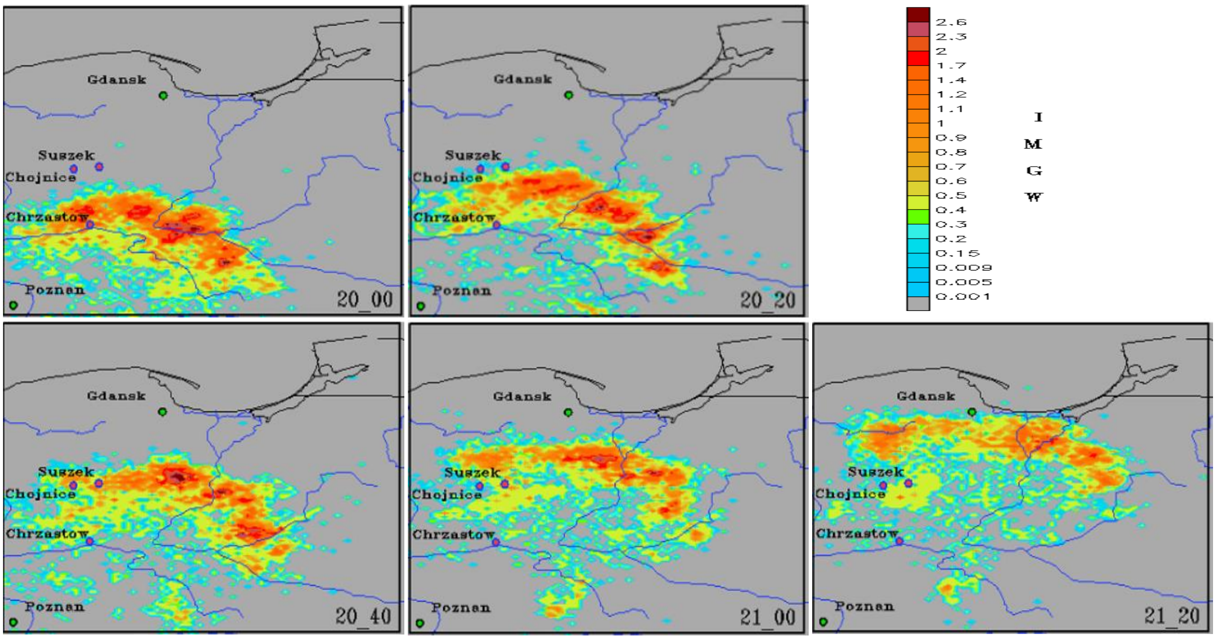

Fig. 11. Set of five maps presenting the evolution of VFS number changes in the vicinity of Chrząstów, Chojnice, and Suszek from 20:00 to 21:20 UTC with the 20-minute time step. The scale of noted VFS number is given by the colored bar. These maps are a necessary supplement to Figs. 6–10 in order to determine precisely the time moment of splitting propagation paths of the considered convective system. More detailed scenario of such split trajectories is depicted in Fig. 12.

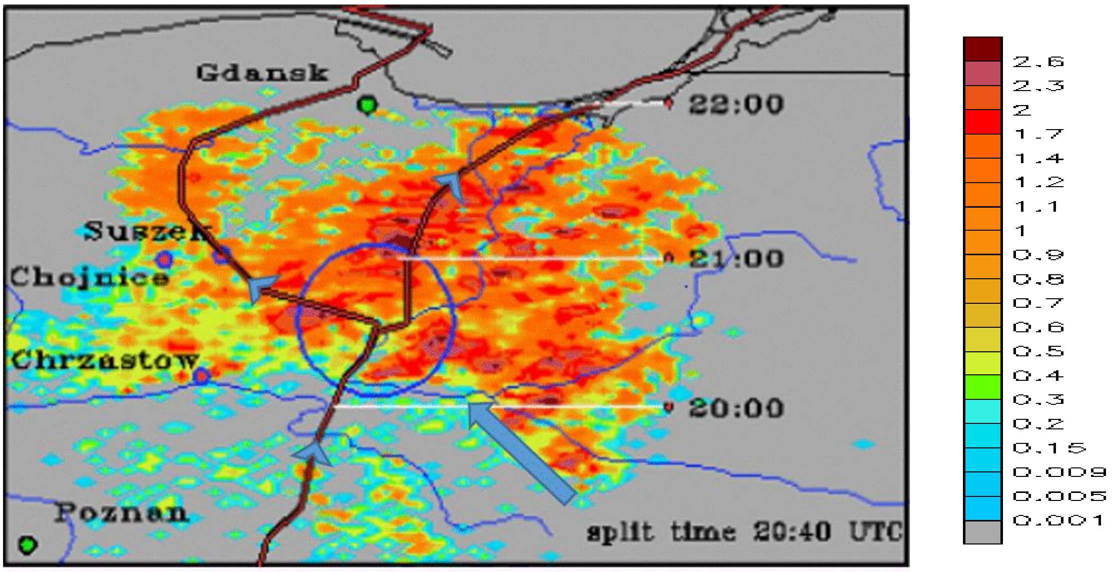

Fig. 12. The scenario of split trajectories of the considered convective system at 20:40 UTC, as the resumption result of five maps given in Fig. 11.

an attempt was made to identify thunderstorm cells at the adjacent dates and recreate their trajectories based on the PERUN lightning detection data that confirmed initially the split occurrence. But such an approach was not straightforward. Thus, forced by the necessity to depart from the pure phenomenology, simulations obtained from the relevant COSMO_2.8 km model were analyzed. These simulations, which routinely started from 18:00 UTC and produced "forecast" fields for the next 6 hours, reproduced unexpectedly well the mesocyclone development process and confirmed the earlier locations of this mesocyclone system given by the relevant Doppler radar products. We presented in Fig. 13 the enlarged (zoomed) space domain together with the considered split occurrence at 20:45 UTC. There we can see the projection of the maximum values of the vertical component of vorticity on the XY and ZY planes, while the barbs illustrate the appropriate wind field at the altitude of 10 km. Here, yellow barbs denote "true wind" in the absolute motion and black ones denote wind in the relative motion to the whole system motion, defined as the absolute motion and reduced by its averaging. These latter well emphasize the properties of the shear-related vorticity. It should be noted that the absolute-motion of the considered air mass turned westward just behind the area of increased vorticity that matches the independently determined propagation path of the western part of the considered convective system to its strong electric activity. Moreover, the relative-motion of air mass agrees well with the whole vorticity pattern. On the other hand, the discussion with experts on the subject pointed to the possibility that the potential MCS split observed by the relevant electric activity changes related to their used pattern may have different characteristics and concern different and higher thundercloud areas in comparison to the occurrence MCS split observed by radar and concerning such cloud regions with a large density of the big-size cloud particles. Hence, the wind field at height of 10 km presented in Fig. 13 corresponds well to the inferred MCS propagation path and changes evaluated from the noted electric activity during the MCS development.

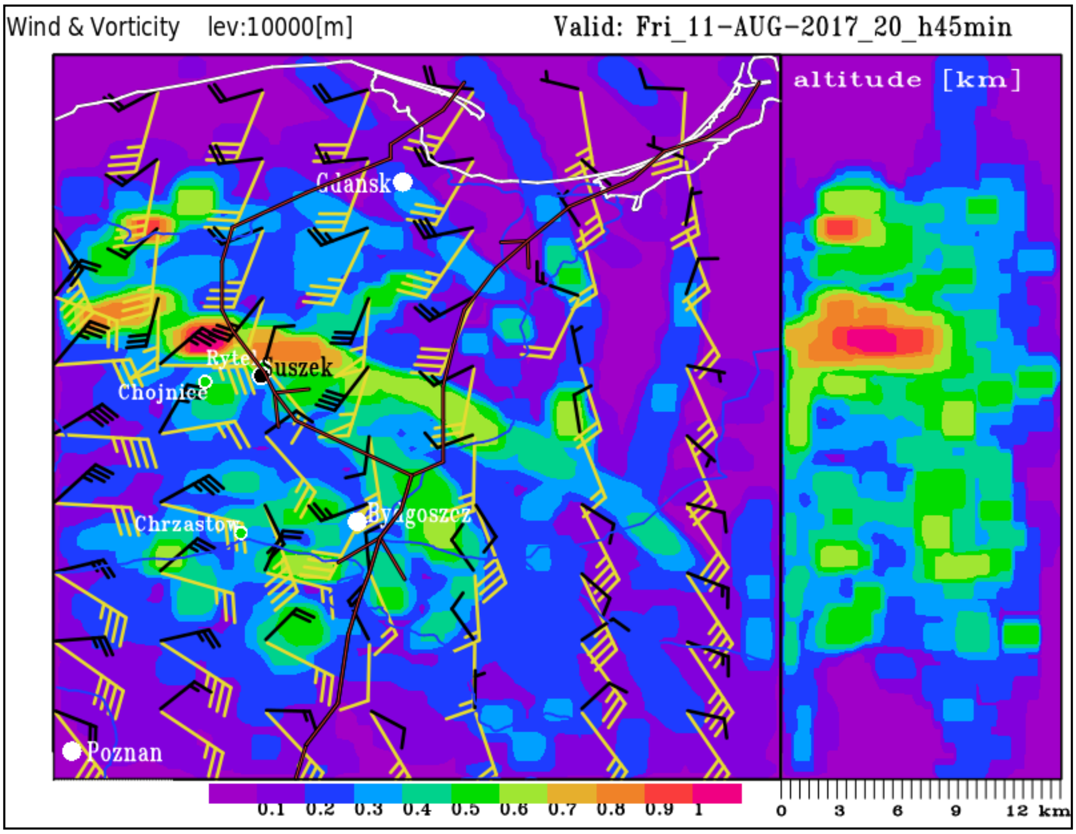

Fig. 13. Projection of the maximum values of 3D vorticity, i.e., the vertical component of the rotation of wind velocity vector multiplied by the scale factor of 2.6×10^3, on the XY and ZY planes. The color and numerical scale of the considered air vorticity is given at the bottom of the XY plane. Additionally, on the XY plane, the wind marked by yellow barbs indicates the absolute air motion/flow and the wind marked by black barbs indicates the relative air motion/flow given for 11 August 2017 at 20:45 UTC for a height of 10 km. Other topographic details superimposed on the XY plane are the same as in Fig. 12.

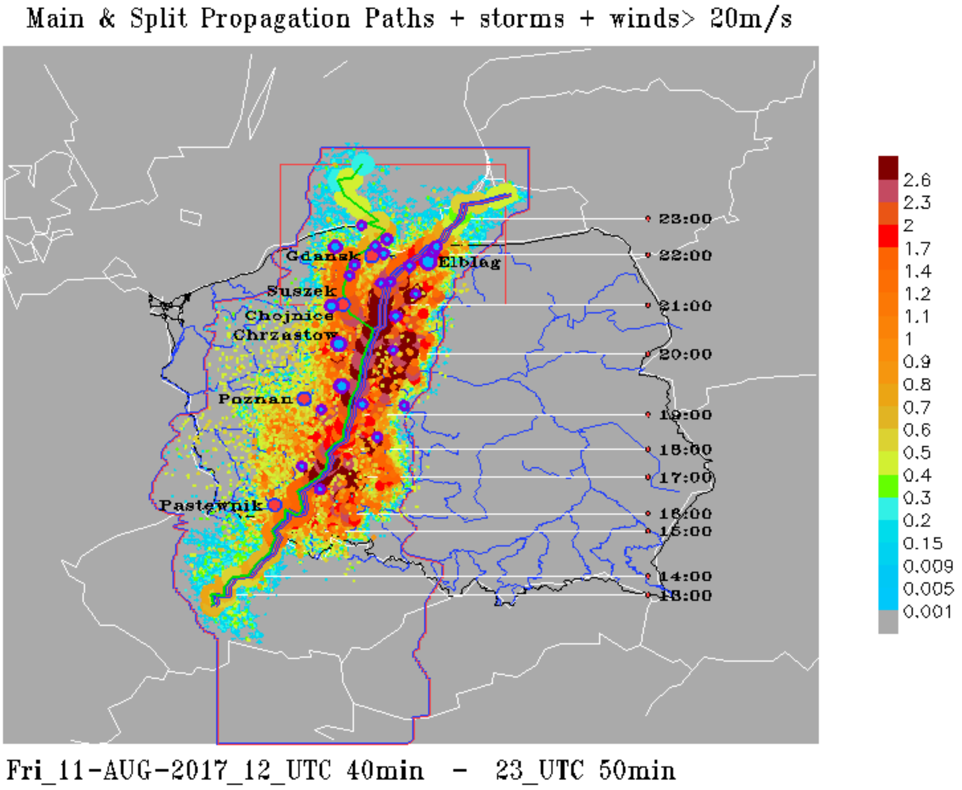

Fig. 14. Main and left propagation paths of the considered MCS with final derecho episode. These paths are overlapped on the MCS electrical activity given in the relevant VFS number indicated by colored bar. Here the wind gusts greater than 20 m/s are marked by blue and violet circles, whose sizes are proportional to the wind strength. Four pink circles show the Doppler radar locations.

The summary result of the analysis performed by us and presented previously in Figs. 6–13 is given in Fig. 14. Here, three hypothetical propagation paths of the considered MCS, in the sense of their physical distinctiveness, were reduced to a single lane with the denoted one split. However, the main path of the MCS has been preserved and additionally marked, because it practically coincided with the MCS eastern propagation path. It is shown as the bold purple line superimposed on the set of separated blue circles, that converged into the single serpentine line and is colored according to the maximum VHS number evaluated for each of the used 68 primary scans. Whereas the thin green line corresponded to the western flank of MCS in accordance with the previous analysis and should coincide with the main MCS track, at least until 20:00 UTC. This can mean that at this time the MCS moving over Poland was compact and without any split. But in the time span from 20:00 to 21:00 UTC, or possibly earlier, if we take, in accordance to Łuszczewski and Tuszyńska (2021), that 19:10 UTC has been the beginning of the MCS split indicated by radar data, it can be seen from Figs. 11 and 12 that the formation of a new separate thunderstorm area was focused at Suszek. Such a thunderstorm area kept its subjectivity (coherence) during its farther northward movement. Hence, the Suszek site can be considered as the location where a detachment or split process of the primary formation of MCS occurred. It is worth relating this MCS split place to possible interaction with the mesocyclone formation given in Fig. 13. Summarizing, the green line that detached from the main MCS path and is shown in Fig. 14 can be understood as a side path of the derecho disturbance. In Fig. 14 there are also indicated 24 different sites where the telemetric measurements of wind gusts exceeding 20 m/s were reported by Mańczak et al. (2021) and Wrona et al. (2022). Although these characteristic wind gust records were noted on both sides

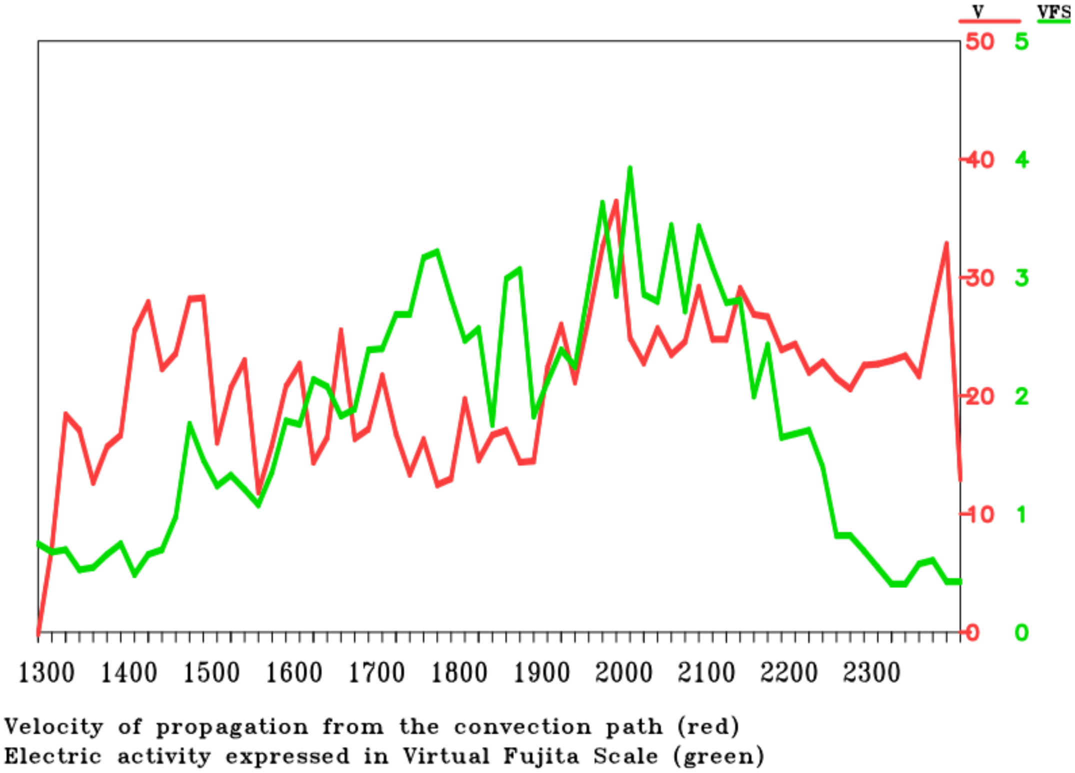

Fig. 15. Synchronous graphs/courses of the MCS propagation velocity and the MCS electrical activity for the considered MCS case on 11 August 2017 in the time interval from 12:40 to 23:50 UTC.

of the main MCS track, the wind activity on its west side correlated more clearly with the most spectacular casualties and damage caused by the considered derecho episode, e.g., in the Tuchola Forest. In turn, the derecho electrical activity prevailed certainly on its eastern flank. For understandable reasons, most of the attention in the papers cited above was focused on the analysis of the western flank, which was also better, but not fully and satisfactorily, documented by radar data from Poznań and Gdańsk.

The eastern and right side of the MCS propagation path presented in Fig. 14 was expressed in the coordinates of the COSMO_2.8 km model and then was used to determine the propagation speed of the whole convection system. This propagation speed calculation was based on the particular locations of such a system, changing in ±10 minutes relative to the given/chosen time moment. The final plot of the variation of MCS propagation velocities obtained for its main path together with changes of the maximum VFS number indicated the MCS electrical activity in the considered MCS area and in the time interval from 12:40 to 23:50 UTC are presented in Fig. 15. The highest estimated MCS propagation speed, up to 40 m/s, occurred around 19:30 UTC and preceded the MCS path split. Additionally, three general characteristics of the MCS with derecho episode, namely, the travelled distance, the time duration, and the average propagation speed, were estimated at 864.42 km, 11.17 hours, and 77.4 km/h, respectively.

5. EVOLUTION OF THE MCS WITH DERECHO EPISODE REFINED FROM ITS LIGHTNING DISCHARGES ACTIVITY AND RELATED TO THE PERFORMED COMPUTER SIMULATIONS CONTEXT

The performed computer simulations of the derecho day at 12:00 and 18:00 GMT enable us to interpret the detected lightning activity of the MCS in a broader synoptic context. Here, the starting point is the proven diagnostic tool, i.e., the operational forecast of turbulence potential, used by the Polish internet pages awiacja_imgw_pl since 2012 and given by Parfiniewicz and Bojanek (2013). The turbulence potential (*PT*) is expressed as a weighted average of two rudimental numbers relating to turbulence, i.e., the Reynolds number (PT_{Re}) and the Richardson number (PT_{Ri}). The formula in Fortran notation for the *PT* parameter can be roughly written as:

$$PT(i,j,k) = \mathrm{SQRT}([PT_{\mathrm{Re}}]**2 + [PT_{\mathrm{Ri}}]**2)/\mathrm{SQRT}(2.)\ \ ,$$

where

$$[PT_{\mathrm{Re}}] = (Ro(k)*V(i,j,k)/\mathrm{skala});\ \mathrm{skala} = 1.\ [\mathrm{kg/m^3}]*30.\ [\mathrm{m/s}]$$

$$[PT_{\mathrm{Ri}}] = (Ro(k)*dV/dz(i,j,k)/a_{\mathrm{min}}1(1.,(0.5 + a_{\mathrm{max}}1(0.,\mathrm{amin}1(1.,3.33*\mathrm{Ri}(\mathrm{i,j,k})))))) \ /\ \mathrm{skala}$$

$$[RoV] = (Ro(k)*V(i,j,k)/\mathrm{skala});\ \mathrm{skala} = 1.\ [\mathrm{kg/m^3}]*1.\ [\mathrm{m/s}]$$

In turn, the additional parameter PT_{Re} per *RoV* can be taken as a calibrated air flow momentum for the considered convective system, where *Ro* stands for the air density and *V* is the 3D air velocity, whereas the PT_{Ri} represents a balanced convection scale, i.e., the air buoyancy versus air flow shear normalized by the scaling factor (skala). However, important in terms of the synoptic approach are, as always, the pressure parameter (*p*3*D*), especially this brought to the sea level [Pmsl], and the distribution of potential temperature parameter (teta), directly related to the height of the tropopause. Since the subject of the considered synoptic process turned out to be a supercell that was created around 17:00 UTC and retained its subjectivity at least until 24:00 UTC during the derecho episode, its rotation (left or right-handed) might be identified as the horizontal vorticity at the mesh model nodes, denoted by *Rot*. The intensity of the considered convection process may be also directly diagnosed by the vertical flow rate parameter *W*.

5.1 The first-stage development, from 12:40 to 15:50 UTC, and the early stage of a supercell formation

We have chosen 12:40 UTC as the beginning of the considered derecho incident. Then the linear thunderstorm zone from South Bohemia changed the direction of movement from SEE-NNW to SSW-NNE. In practice, this propagation direction remained unchanged until the end of the derecho episode, i.e., until 23:50 UTC. The propagation path of the MCS as a whole was presented with details in Section 4. Until 14:00 UTC the linear thunderstorms zone, arranged perpendicular to the propagation, was on the Czech side, approaching the Sudetes (a mountain range constituting the Polish-Czech border). The process of overcoming the mountain barrier ended at 15:50 UTC. At that time, the whole of Lower Silesia region was in a stormy area, with two characteristic and separate lightning patterns grouped in the vicinity of the Kłodzko Valley (see the map at 15:50 UTC in Fig. 16) and far west of the Moravian Gate, that was usually privileged when convection flew from the Czech side. To conclude the consideration of this stage, it is worth noting that the maximum peak values of lightning discharge activity, given in Fig. 16 by changes of the relevant VFS number, increased from 0.5 at 13:50 UTC in the area of Prague, in the Czech Republic, to 1.8 at 15:40 UTC in the Kłodzko region, in Poland. The whole course of this early, convective stage development is presented in Fig. 16 by the set of four selected maps showing changes of the equivalent VFS number obtained during the 10-minute time interval.

The related synoptic context of the considered MCS convection process in the time interval from 12:40 to 15:50 UTC is summarized by the relevant set of four maps for *p*3D, (teta), *W*, and *RoV* parameters simulated at 15:45 UTC and shown in Figs. 17–20, respectively.

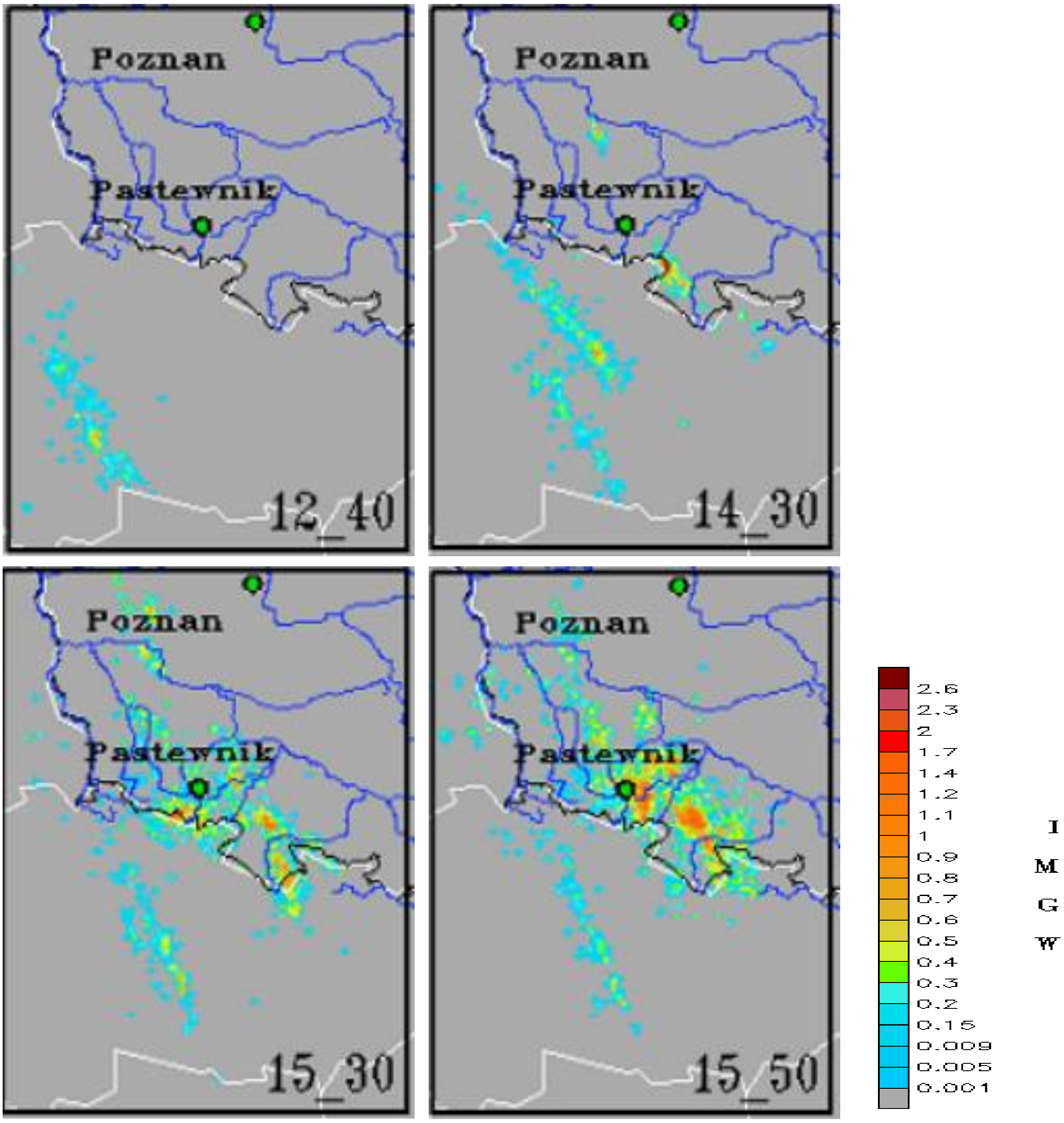

Fig. 16. Set of four selected maps indicating changes of the equivalent VFS number obtained during the 10-minute time interval and evaluated at 12:40, 14:30, 15:30, 15:50 UTC, respectively, and illustrating the first stage of MCS development.

Basing on the relevant air flow field patterns given in Figs. 17–20 we can note that a characteristic feature of the considered MCS convection process during its early development stage with a supercell formation was firstly connected to the deepening of the pressure depression and formation of ground-level convergence zones, as shown in Fig. 17; secondly – to a lowering of the tropopause height on the derecho track and covering the areas of Wrocław and Poznań from the west side, as presented in Fig. 18; thirdly – to an increase of the vertical air velocities in the area of Wrocław and Poznań, as given in Fig. 19; and forthly – to an increase of the air flow momentum strength from the west together with the formation of a "wind hammer" in the Wrocław-Poznań region, as depicted in Fig. 20.

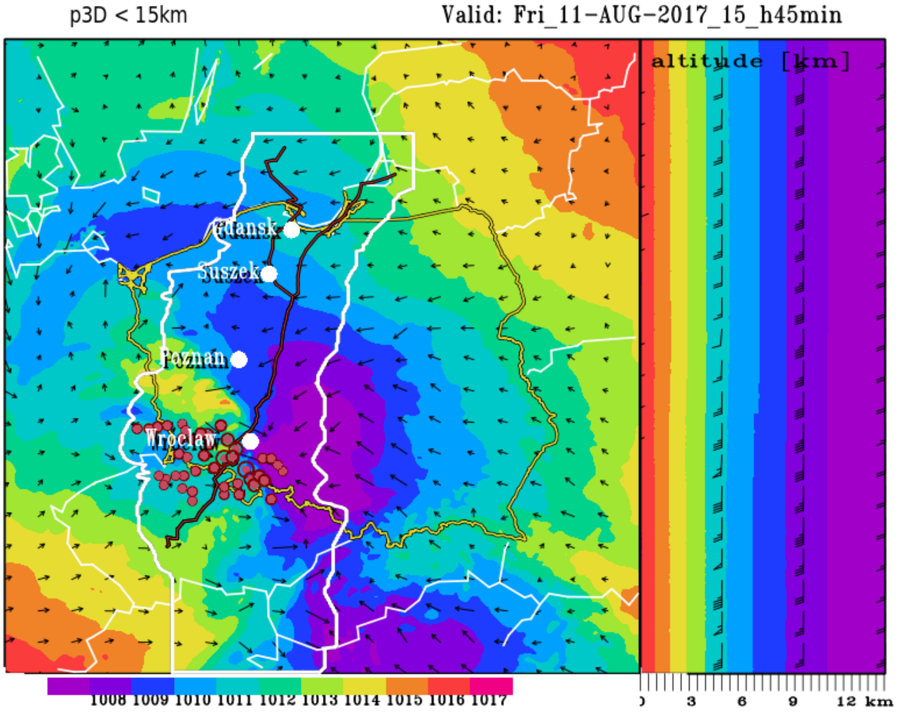

Fig. 17. The simulated map of the *p3D* parameter calculated for 15:45 UTC and shown in the XY and ZY planes. The color and numerical scale in hPa units is indicated at the bottom of the XY plane. The relevant wind pattern (in knots), for its horizontal components (*u*, *v*), is indicated by black vectors in the XY plane and by barbs for its vertical components (*w*, *v*) in the ZY plane. Additional topographic details superimposed on the XY plane related to the considered MCS path with spilt incident are the same as in Fig. 14. In turn, the set of small and bigger red dots presents the locations of lightning activity sources detected at 15:45 UTC, whose size is in the accordance to the calculated VFS numbers in the particular location area.

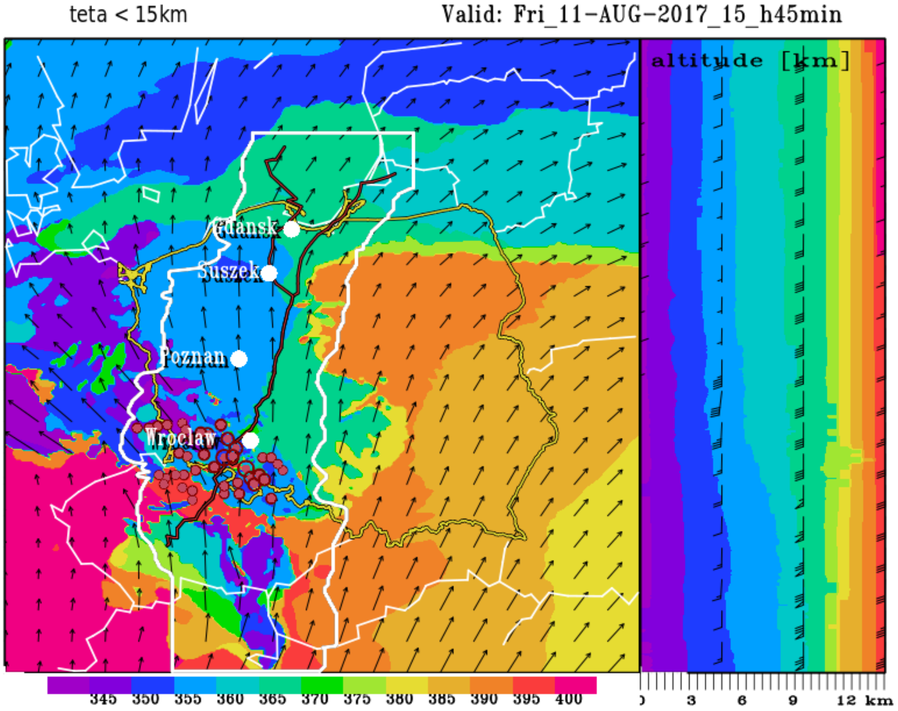

Fig. 18. The same as in Fig. 17, except of the pattern for the simulated map of the (teta) parameter calculated at 15:45 UTC, and the color and numerical scale indicated in °K unit.

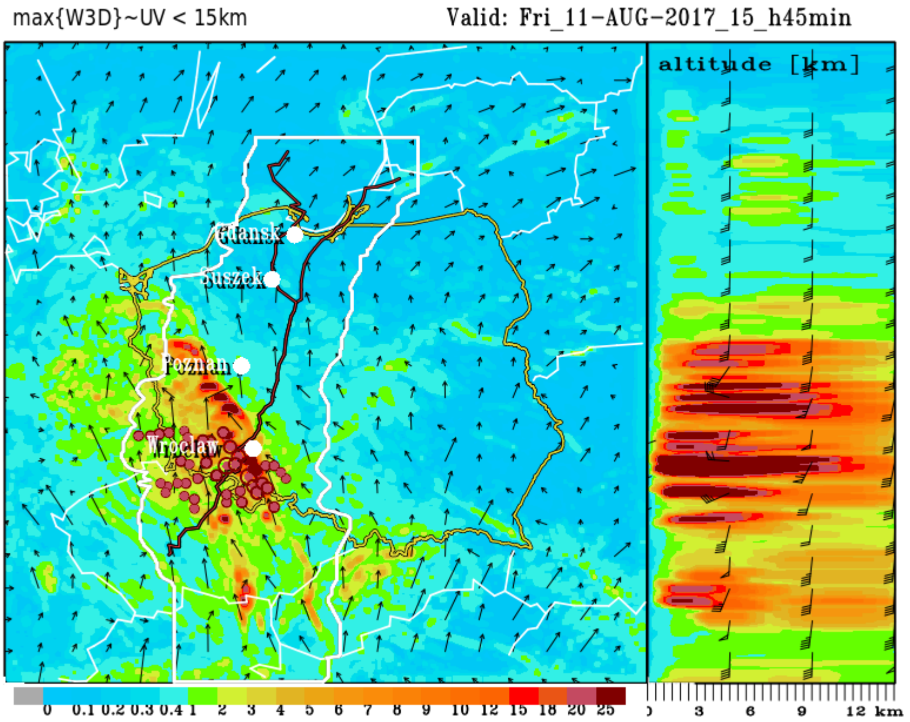

Fig. 19. The same as in Fig. 17, except of the pattern for the simulated map of the *W* parameter calculated at 15:45 UTC, and the color and numerical scale indicated in knots.

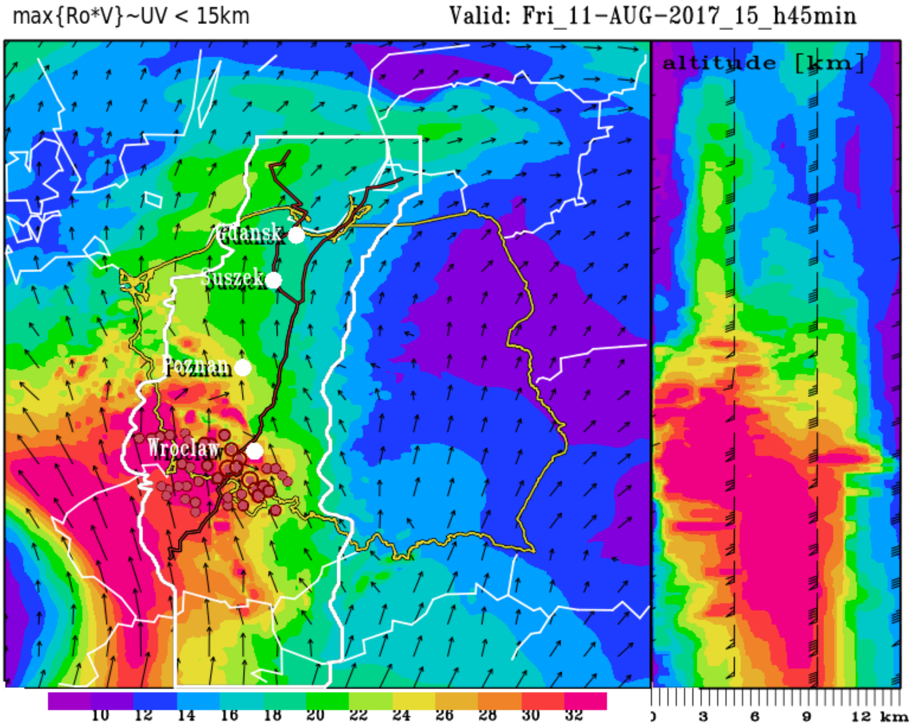

Fig. 20. The same as in Fig. 17, except of the pattern for the simulated map of the *RoV* parameter calculated at 15:45 UTC, and the color and numerical scale indicated in formally dimensionless units (due to the normalization of *RoV* by a scaling factor (skala = 1. [kg/m^3]*1. [m/s]), which numerically reduces this expression to a calibrated by density air flow).

5.2 The second stage development, from 16:00 to 17:30 UTC, and further supercell consolidation

We can talk about an earlier evolution of a derecho incident over Poland from 15:50 UTC. The considered MCS route, just from this time moment, takes place over Poland territory. In turn, from 16:00 UTC we have observed a fluctuating increase in the electric activity reaching the relevant VFS number equal to 2.4 at 16:40 UTC. After that, the value of VFS number increased sharply to 3.23 at 17:30 UTC (see Fig. 22). Hence, we can presume that this electric activity stage of the MCS is connected to its consolidation process into a supercell form, as reported by Łuszczewski and Tuszyńska (2021). Indeed, as can be seen from the Poznań radar data, at this time the considered MCS makes its overshooting to the stratosphere, as shown in Fig. 21.

Here, it should be noted what happens during this MCS development stage over the Silesian Lowlands region, where the MCS consists of two separated convection cores indicated in Fig. 22 by the map at 17:30 UTC. They are located in the NW and SE sectors, respectively, while the one from the SE sector is electrically more active, with a set of two-chamber/twin storm cores indicated by the evaluated VFS number equal to 3.23 and having two convection shafts. It can be interesting to notice and probably it is a characteristic feature for such a development stage of the considered MCS formation that the building-up phase of its electrical activity is finished in a significant decrease of the MCS propagation speed. This might mean that the considered two storm cores could possibly slow down the expected jet stream support for a further development of the MCS. But unfortunately, it does not happen at that time. This was verified and confirmed by the course of the considered MCS development process that lasted from 16:00 to 17:30 UTC and is presented in Fig. 22 by the set of five maps indicating the particular change of the relevant VFS number evaluated in accordance to the PERUN lightning detection data given in the real time.

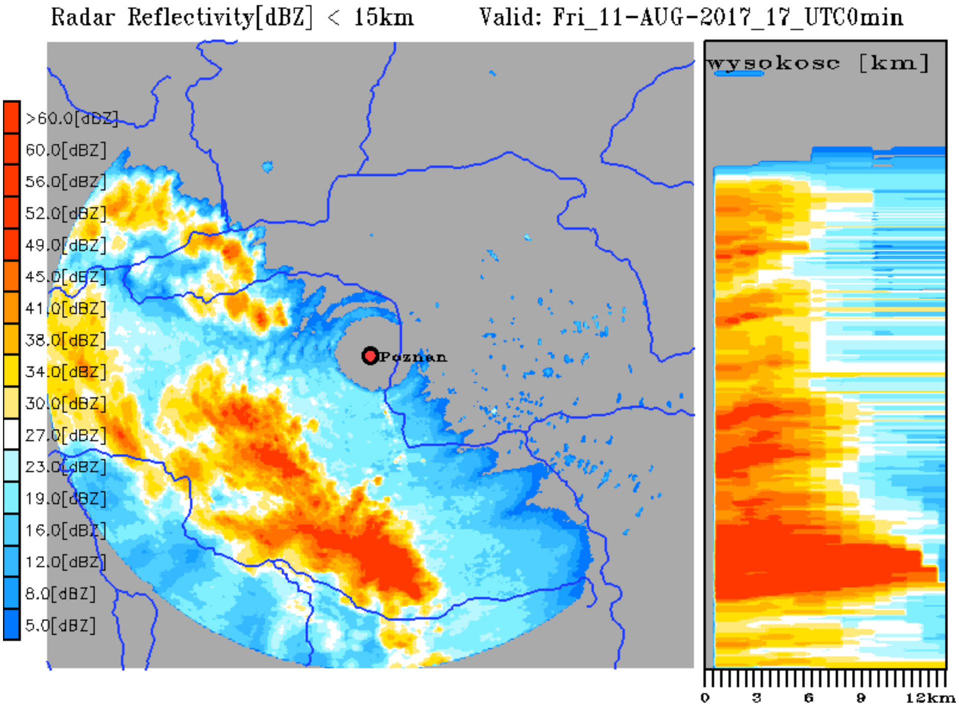

Fig. 21. Quasi 3D scans of radar reflectivity data obtained from the Poznań radar at 17:00 UTC. These radar scans were also preceded by the interpolation of the measured radar reflectivity in the altitude range from 1 to 18 km and the grid step of the XY plane of about 0.7 km, similar to the computational grid COSMO_2.8 km model with $\Delta z = 250$ m.

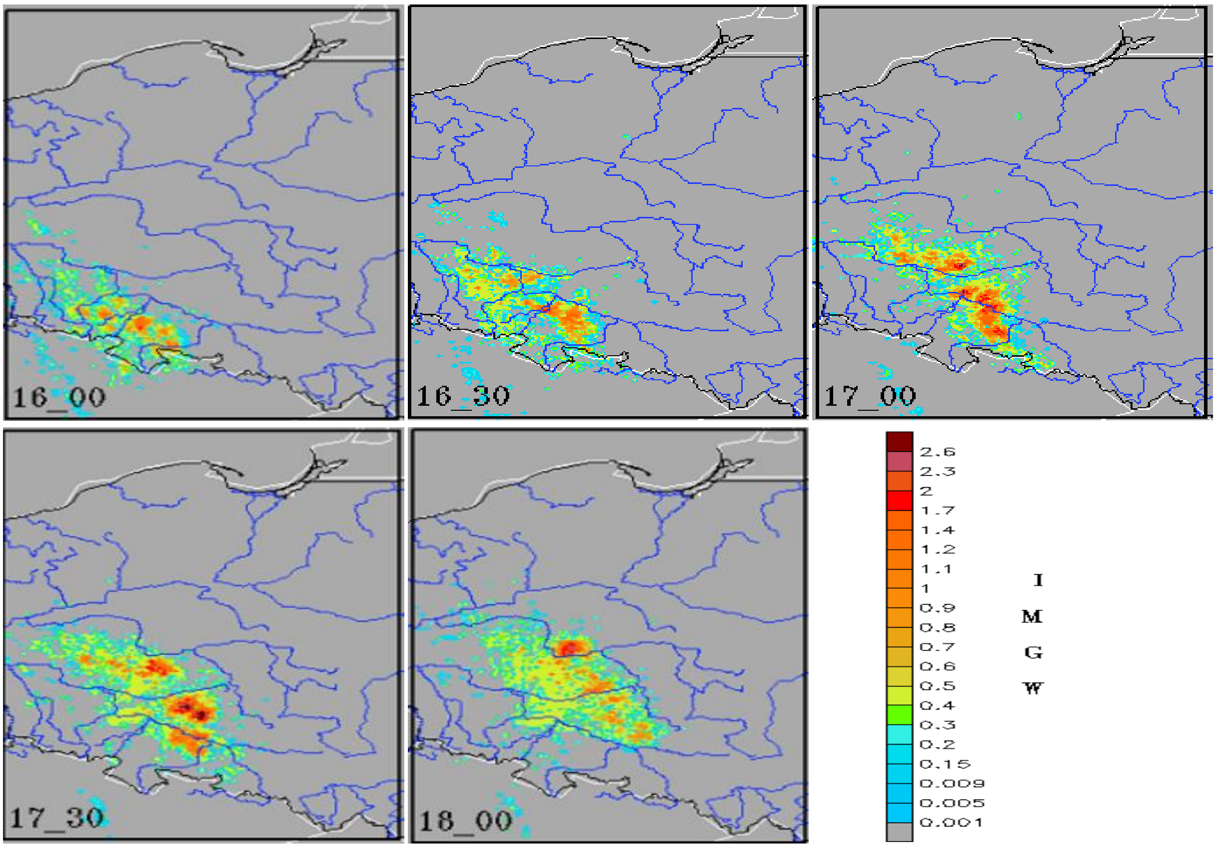

Fig. 22. Set of four selected maps indicating changes of the equivalent VFS number obtained during the 30-minute time interval and illustrating the second stage of MCS development lasting from 16:00 to 17:30 UTC. The additional fifth map just shows the transformation of MCS to its structure noted at 18:00 UTC and starting the next and later MCS development stage.

The relevant synoptic context of the following development of the considered MCS convection process in the time interval from 16:00 to 17:30 UTC is summarized by the next set of four maps for *p*3*D*, (teta), *RoV*, and *Rot* parameters simulated at 17:00 UTC and shown in Figs. 23–26, respectively. Additionally, the METEOSAT SEVIRI color-enhanced IR brightness temperature image showing the exact location of the supercell formation over Poland on 11 August 2017 taken from the EUMETSAT 2017 database at 17:00 UTC is given in Fig. 27.

Taking into account the air flow field patterns given in Figs. 23–26 we can note that a characteristic feature of the considered MCS convection process during this development stage involves further supercell consolidation. This consolidation was connected to: first – the deepening of the pressure depression with an extremely strong ground-level convergence zone, as shown in Fig. 23; second –the lowering of the tropopause height that coincided, in the XY projection, with such supercell formation covering the regions of Poznań and Wrocław, as presented in Fig. 24; third – to the formation of a stream air flow transferring energy from the upper atmosphere to the ground layers, as given in Fig. 25; and fourth – to the increase in negative rotation airflow, indicating that the positive left-handed flows which prevailed at the beginning were gradually followed by negative right-handed flows, as shown in Fig. 26.

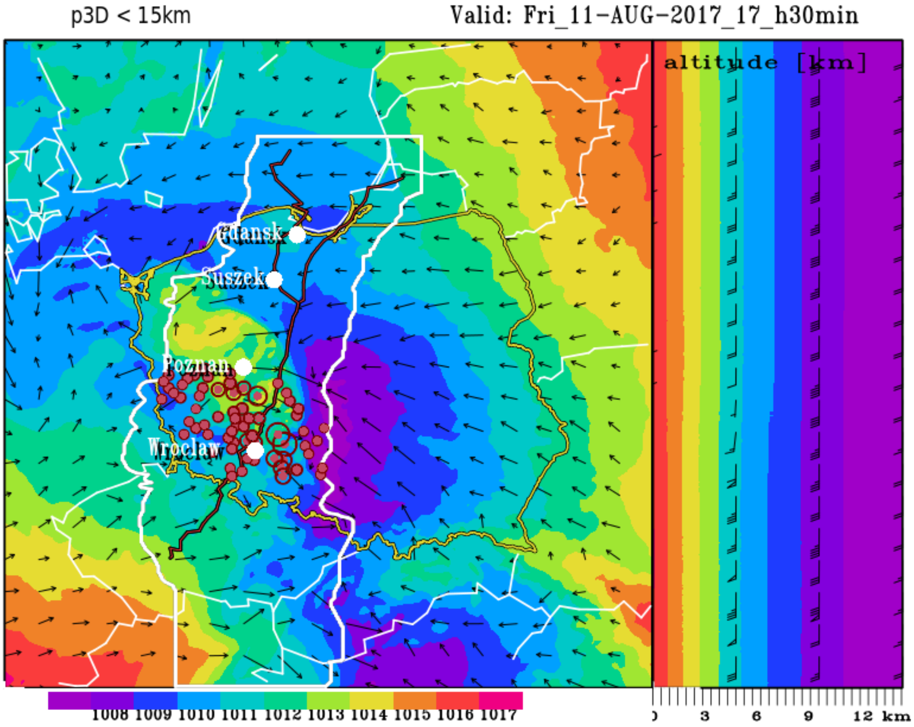

Fig. 23. The same as in Fig. 17, except for the pattern for the simulated map of the *p3D* parameter and lightning activity calculated at 17:30 UTC.

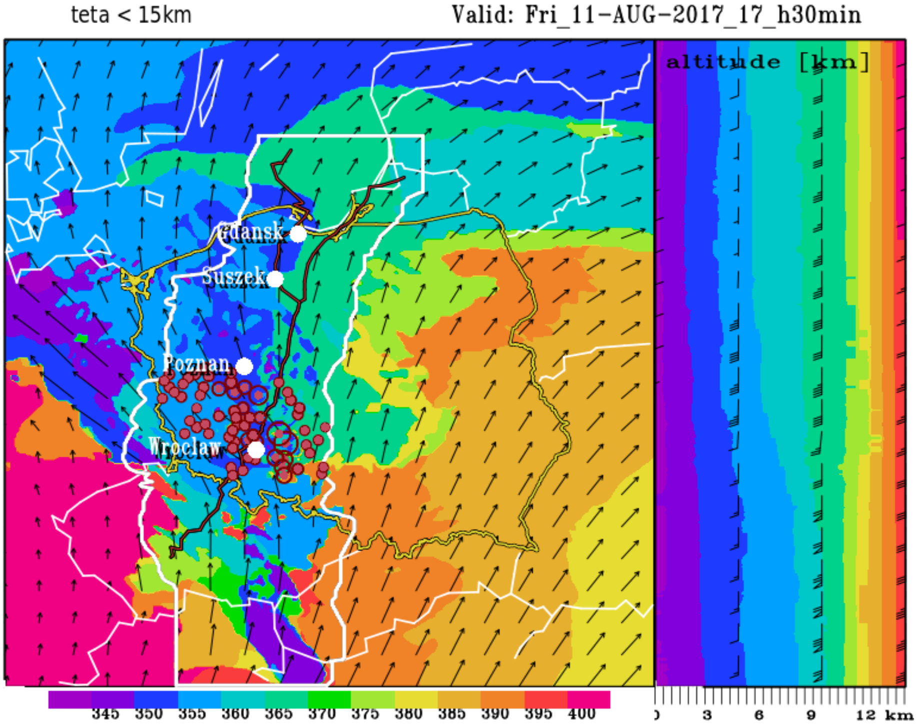

Fig. 24. The same as in Fig. 23, except for the pattern for the simulated map of the (teta) parameter and lightning activity calculated at 17:30 UTC.

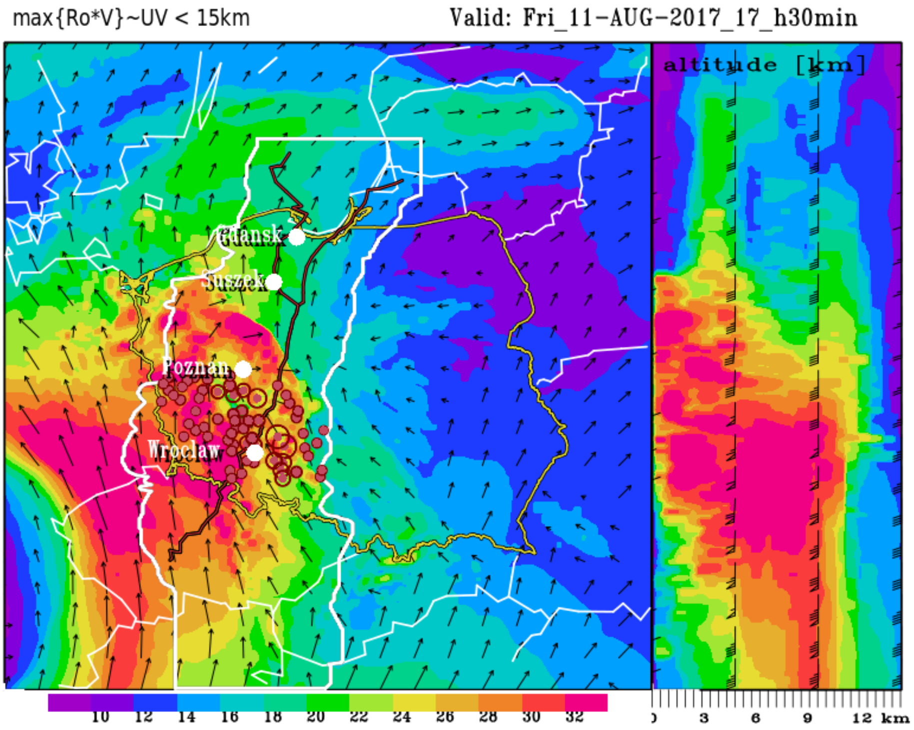

Fig. 25. The same as in Fig. 23, except for the pattern for the simulated map of the *RoV* parameter and lightning activity calculated at 17:30 UTC.

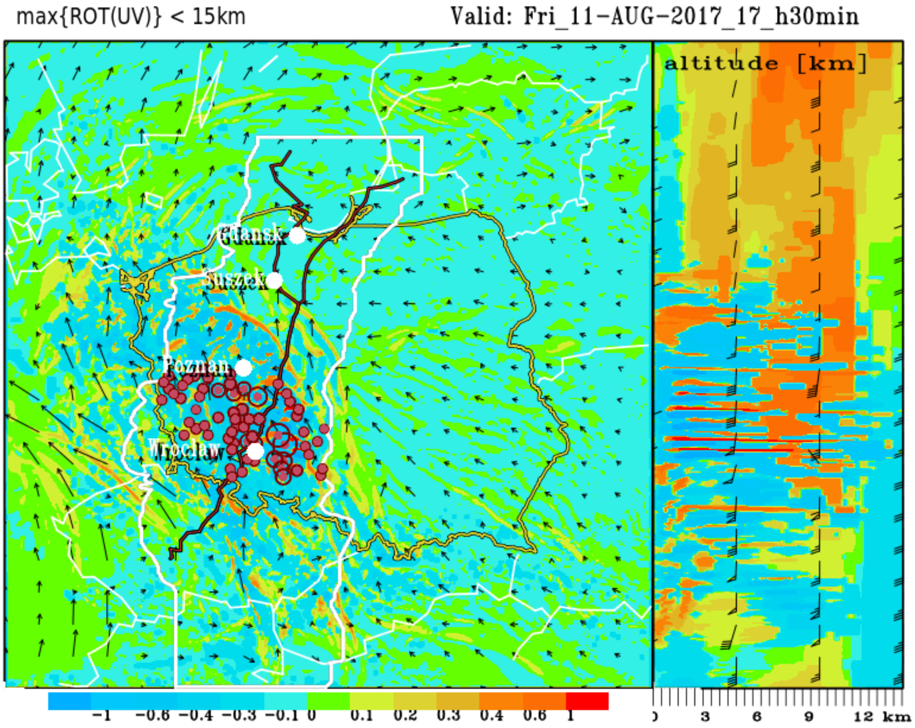

Fig. 26. The same as in Fig. 23, except for the pattern for the simulated map of the *Rot* parameter and lightning activity calculated at 17:30 UTC.

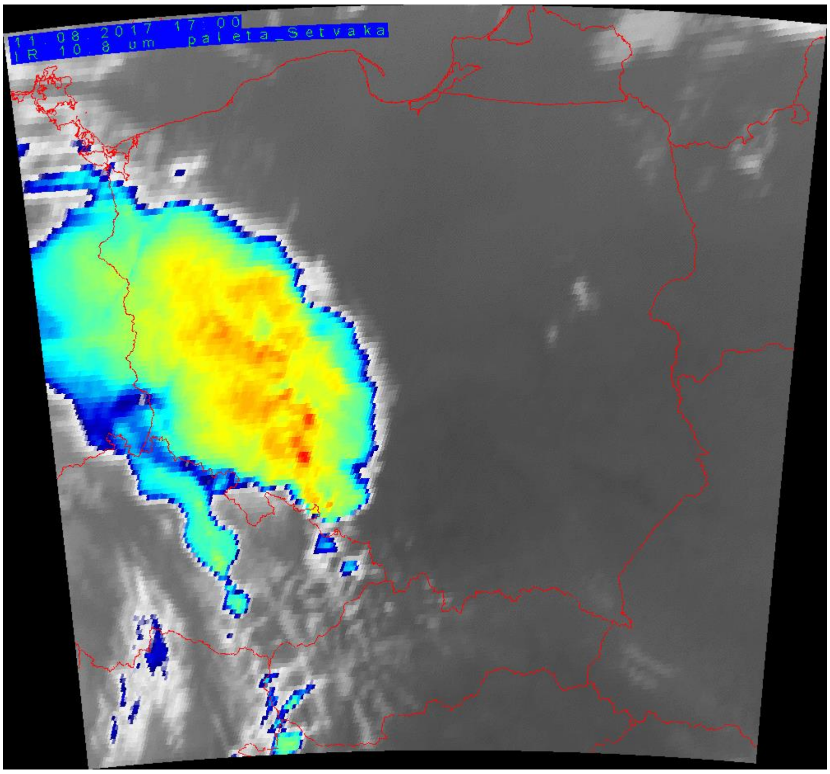

Fig. 27. METEOSAT SEVIRI color-enhanced IR brightness temperature image of the considered supercell formation over Poland on 11 August 2017 taken from the EUMETSAT 2017 at 17:00 UTC (© EUMETSAT 2017, © dane.sat4envi.imgw.pl, © OpenStreetMap contributors, reported also by Łapeta et al. (2021)).

5.3 The third stage development, from 17:30 to 21:00 UTC, together with the MCS split episode at 20:40 UTC

Let us define now the considered MCS as the set of convective nuclei (cores) of an evolving supercell. After 17:30 UTC, further MCS consolidation took place. In the considered time period, two separated strong convective areas of thunderstorm lightning activity have merged into one coherent and huge convection region, where the dominance of the NW located thunderstorm pattern was noted and presented in Fig. 22 by the map given at 18:00 UTC. Moreover, ten minutes later, at 18:10 UTC, we recorded the minimum VFS number equal to 1.77, that later on rapidly increased, reaching the local maximum of 3.08 at 18:30 UTC, which was shown in Fig. 15.

At 19:10 UTC dense/compact lightning discharge zones occurred east of Poznań and were stretched linearly from SE to NW (see Fig. 28). The further evolution process of the whole convection system was toward the transformation into a characteristic bow echo structure, which was reached at 19:20 UTC and lasted beyond this time. Such a development phase of the considered MCS is presented in Fig. 29.

After a temporary decrease, there was a sharp increase in electric activity and propagation speed of the MCS, as shown in Fig. 15 at 19:10 UTC. Moreover, as the surface wind records reported by Mańczak et al. (2021) and Wrona et al. (2022) have shown, also the strength of surface wind activity increased rapidly and, at the time period of the derecho, it entered into the most destructive force. At the beginning of this development period, at 19:10 UTC, the developing bow echo MCS structure consisted of four distinct and separated thunderstorm areas presented clearly in Fig. 28. In turn, going back to the synchronous courses of the MCS

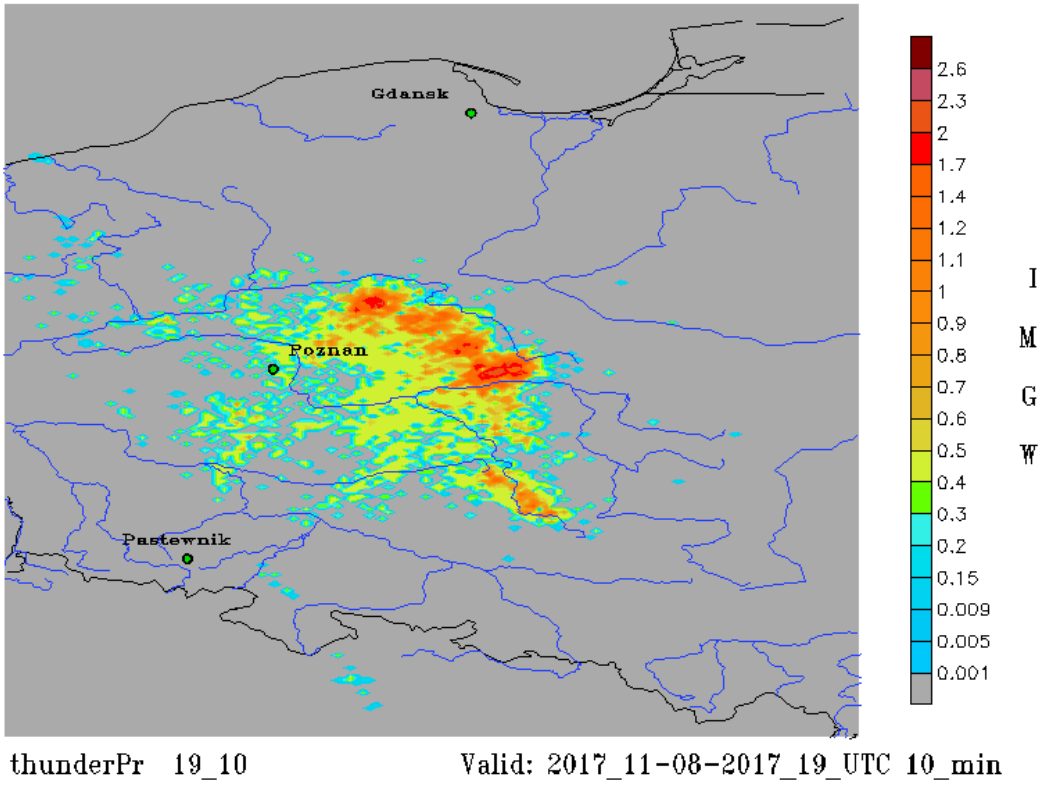

Fig. 28. Characteristic bow echo structure of the considered MCS that was indicated at 19:10 UTC and given by the relevant values of VFS number according to the colored bar on the right. Three green circles stand for the Pastewnik, Poznań, and Gdańsk radar location, respectively.

propagation velocity and the MCS electrical activity expressed by VFS number given in Fig. 15, we can notice that the absolute maximum of VFS number of 3.93 was reached at 19:50 UTC, whereas the four-chamber convective structure was transformed into three massive thunderstorm centers to merge 20 minutes later, at 19:30 UTC, as the expanded and arched thunderstorm structure presented in Fig. 29. Such state lasted until 20:10 UTC. After this time, we have noticed the process of the torn and splitting of the western part of the whole convective system described in detail in Section 4 and presented in Figs. 12–13. Such process ended with a clear breakdown of the MCS into two branches, i.e., the first stronger and eastern, and the second weaker and western, which then turned north, as shown in Figs. 11–12 and 29–35. This MCS transformation process evolved further until 20:30 UTC, when it was possible to distinguish two convection regions separated by the Vistula river, i.e., the west part and the east part. By 20:50 UTC, the western convective region was more electrically active, reaching the relevant VFS number equal to 3.44 at 20:40 UTC and equal to 3.10 at 20:50 UTC, as shown in Fig. 29 by the time span from 20:30 to 21:00 UTC and in Fig. 35 by the time span from 21:10 to 21:50 UTC. The whole course of this MCS development phase lasted from 19:00 to 21:00 UTC, which was documented by changes in the relevant value of VFS number obtained from the real time PERUN lightning detection data and presented in Fig. 29, as a sequence of the selected seven maps given with the 20-minute time step.

The supplementary synoptic context of the MCS development process lasting from 17:30 to 21:00 UTC was presented in Figs. 30–33 by four simulated maps of the relevant parameters (teta), *RoV*, *Rot*, and PT_{Ri} obtained at 20:45 UTC, i.e., at the simulation output time close to the time moment of the MCS split incident determined from the PERUN lightning detection data.

Additionally, after Łapeta et al. (2021), the METEOSAT SEVIRI color-enhanced IR rightness temperature image of the considered supercell formation over Poland on 11 August 2017, taken from the EUMETSAT 2017 at 20:45 UTC, was shown in Fig. 34.

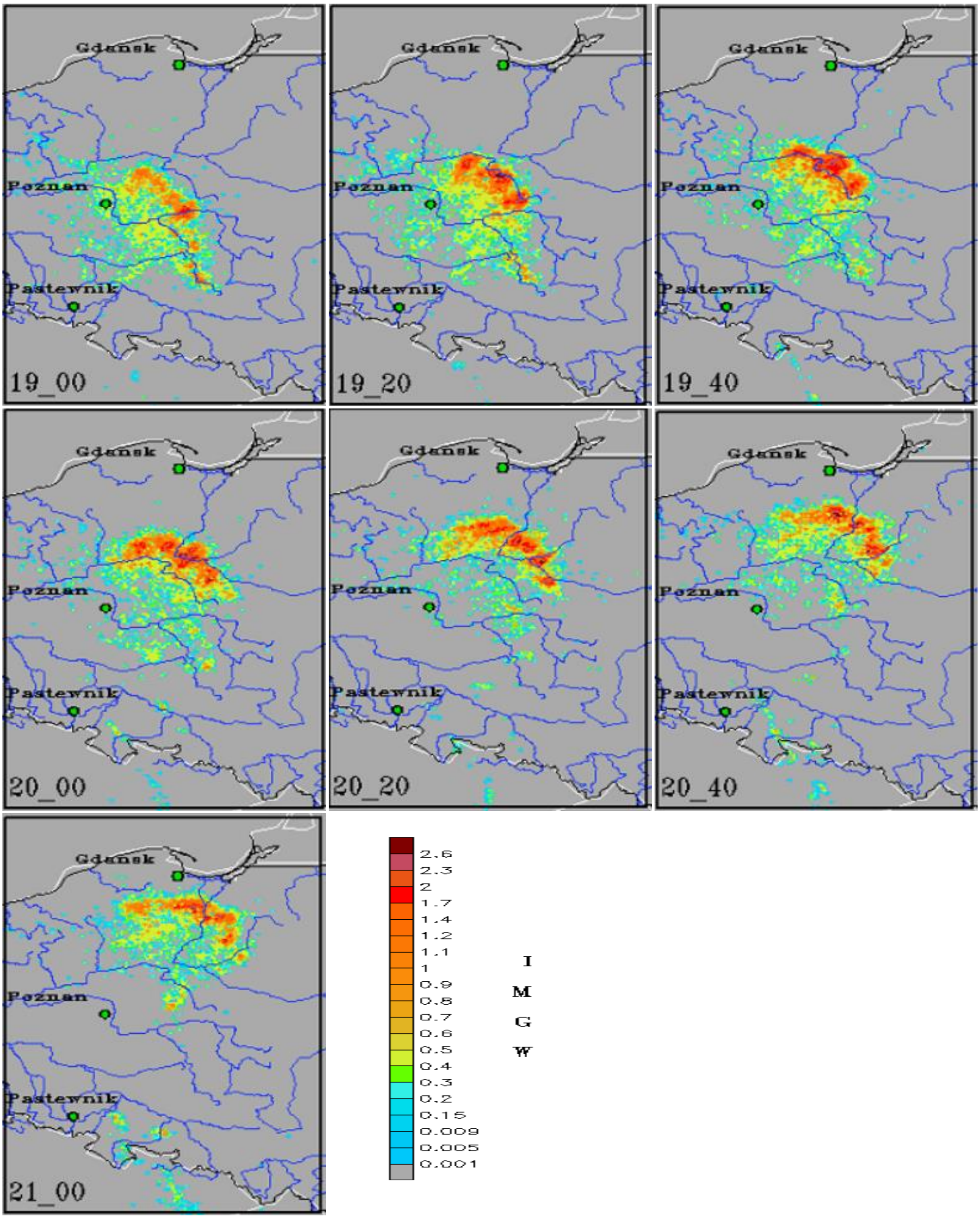

Fig. 29. Time sequence of seven maps given with the 20-minute time step presenting the relevant electrical activity changes during the MCS development stage that lasted from 19:00 to 21:00 UTC.

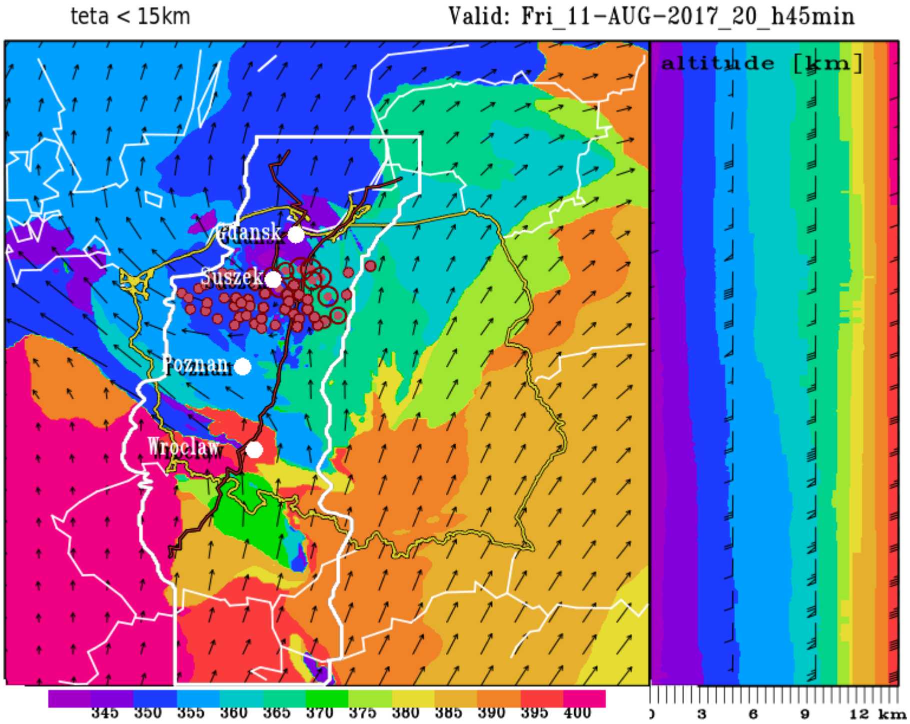

Fig. 30. The same as in Fig. 18, but showing the pattern for the simulated map of the (teta) parameter and lightning activity calculated at 20:45 UTC.

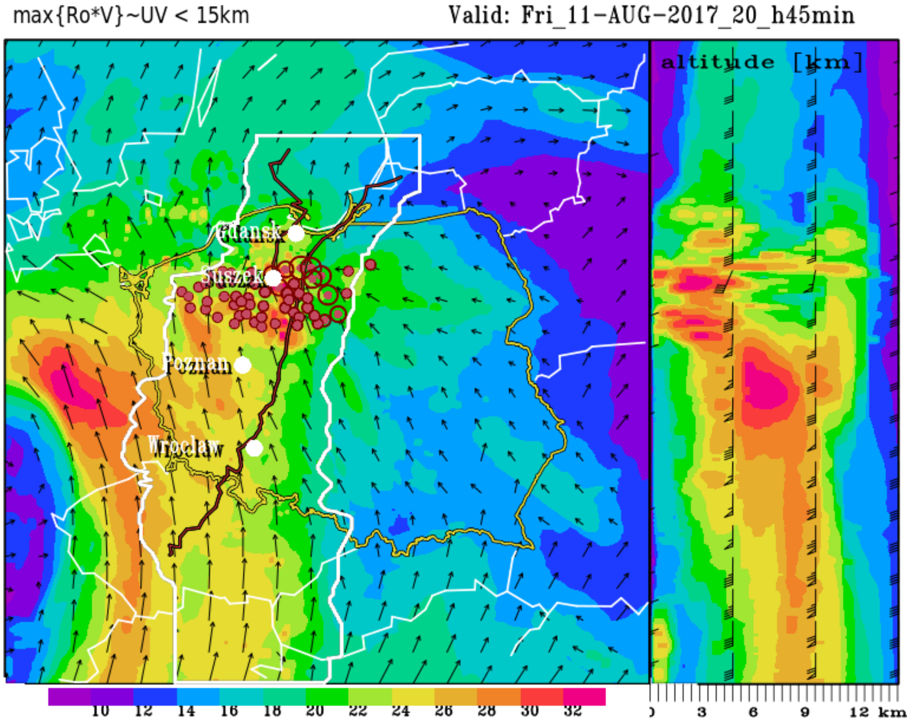

Fig. 31. The same as in Fig. 30, but showing the pattern for the simulated map of the *RoV* parameter and lightning activity calculated at 20:45 UTC.

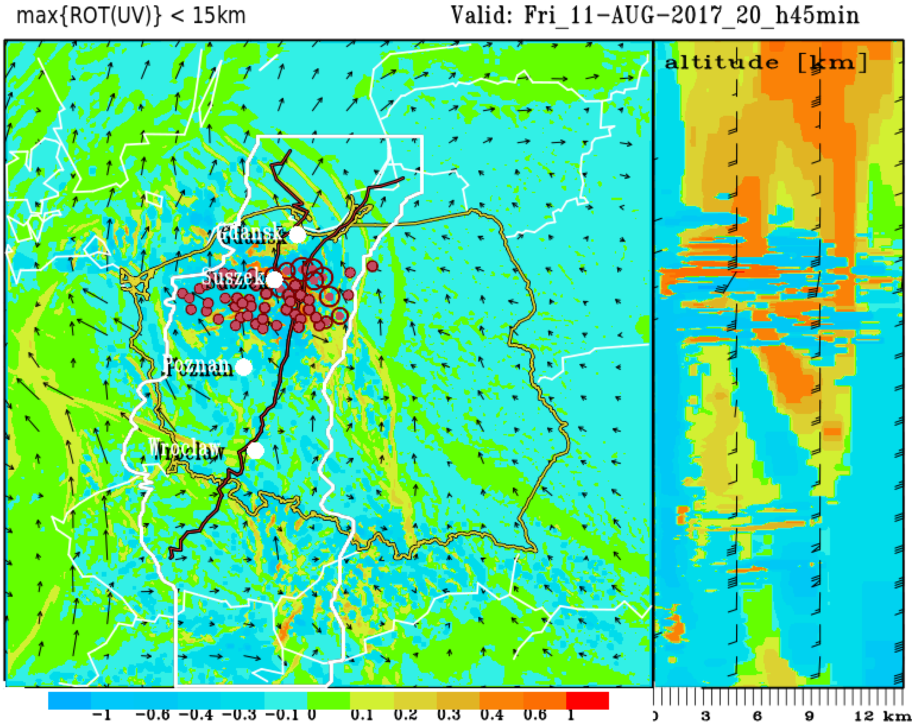

Fig. 32. The same as in Fig. 30, but showing the pattern for the simulated map of the *Rot* parameter and lightning activity calculated at 20:45 UTC.

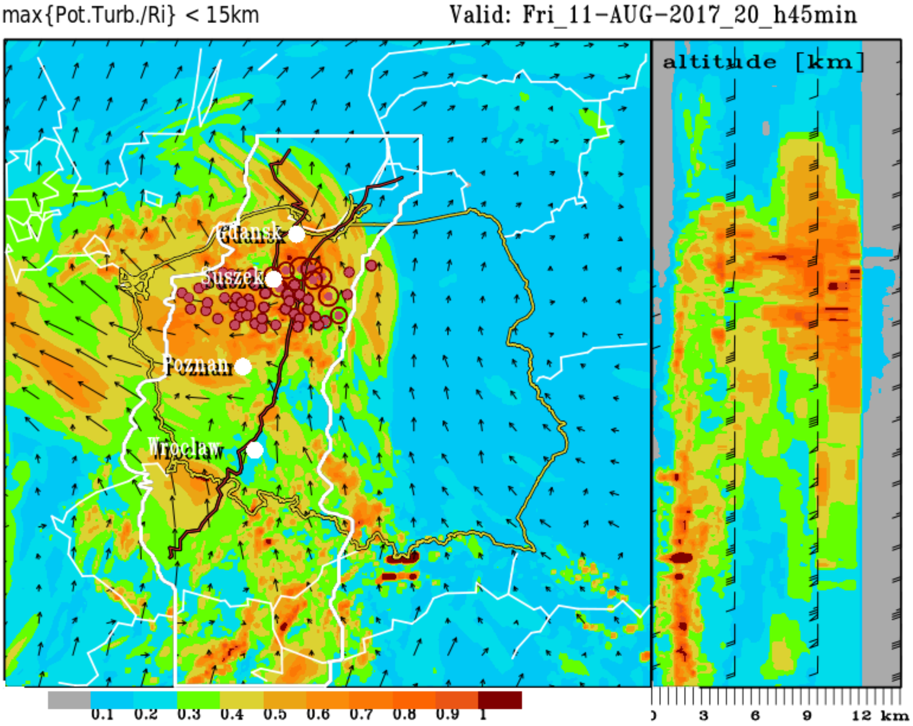

Fig. 33. The same as in Fig. 30, but showing the pattern for the simulated map of the PT_{Ri} parameter and lightning activity calculated at 20:45 UTC.

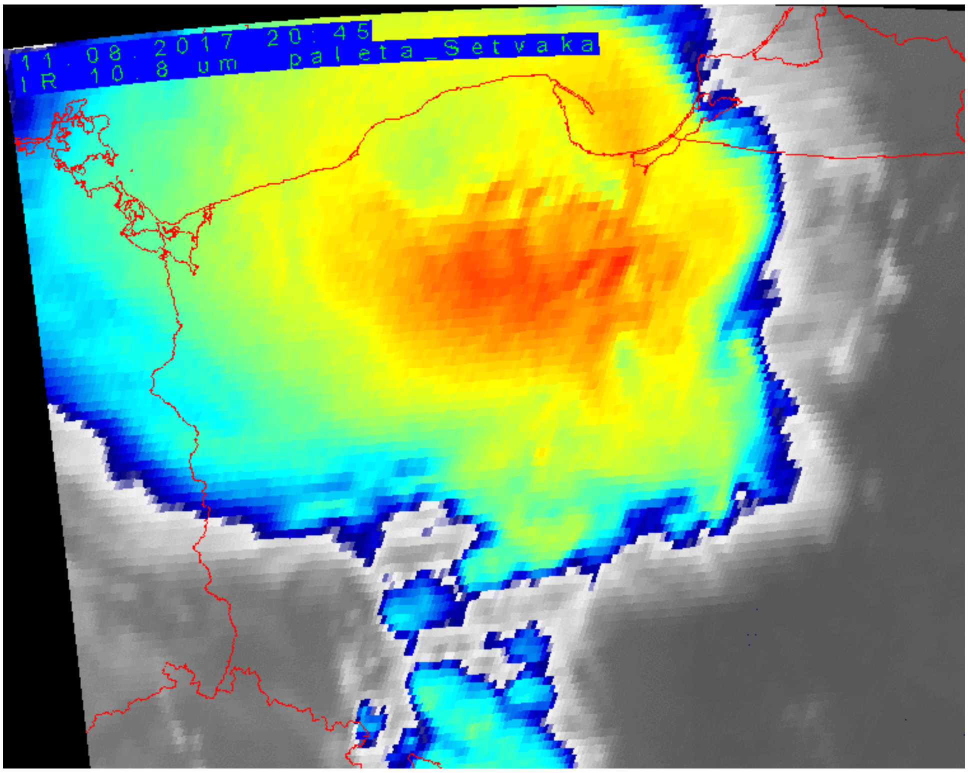

Fig. 34. METEOSAT SEVIRI color-enhanced IR brightness temperature image of the considered supercell formation over Poland on 11 August 2017 taken at 20:45 UTC (© EUMETSAT 2017, © dane.sat4envi.imgw.pl, © OpenStreetMap contributors, reported also by Łapeta et al. (2021)).

Bearing in mind that the MCS spilt incident was a characteristic feature of the convective process during this MCS development, we can find that a separate thunderstorm area occurred in the Suszek region between 20:00 and 21:00 UTC and retained its subjectivity/coherence in the northward movement. It meant a creation, detachment, or just a split of the MCS path, whatever we call it, and a new-line MCS movement was detached from its previous main track as a side track of the appearing derecho episode. At first, as it was shown in Fig. 30, the tropopause is evidently lowered over the derecho track, with the maximum depression preceding the MCS position, and at 20:45 it is located north of Suszek. After the MCS passage, i.e., south of Suszek, clearly higher tropopause temperatures prevail. The wind field simulated at the moment at an altitude of approx. 12 000 m confirms the separation of the stream into a more western and north-eastern branch. Secondly, as it was shown in Fig. 31, the air momentum stream transferred the kinetic energy from the upper troposphere to the ground layers and its maximum value reached the ground layers just in the Suszek area. Thirdly, as it was presented in Fig. 32, high values of the wind rotation field, alternating positive and negative, coincided well with the supercell space domain, which was clearly seen in the satellite IR images. At this time, the whole MCS determined from the activity of lightning discharges resided in the supercell area. On the other hand, as indicated in Fig. 33, the Richardson component of turbulence potential located the supercell space domain quite well, and similarly to the location provided by the wind rotation field, especially at the sub-tropopausal levels. Taking into account that the satellite diagnostics of the supercell occurrrence, as given by Setvak et al. (2010), is related to the temperature of the upper atmosphere by a cold ring or cold U shape, we can note that such a numerical index PT_{Ri} as depicted in Fig. 33 enables complementary phenomenological diagnostics of supercell formations. In turn, the temperature of supercell top shown by IR brightness image in Fig. 34 uniquely and phenomenologically diagnoses the supercell space domain. The considered synoptic context that has turned out to be a supercell formation, needs further tracing of the supercell, in space and time, to better understand the whole derecho evolution process. However, some limitations of such phenomenological diagnostics are well illustrated by the quotation taken from Łapeta et al. (2021): "The transformation from cold U shape into a cold ring structure again seemed to begin around 20:30 UTC, however, the temperature distribution along the ring was not homogenous and a distinctive minimum can be seen in its northwestern part. This complicated structure should be considered as the result of the interaction between single overshooting tops located close to each other."

5.4 The final, fourth stage development, from 21:10 to 23:50 UTC, with weakening and degradation of the whole MCS

The final completion of the whole MCS evolution process resulted in the single remnant thunderstorm cluster activity on the western MCS flank, that was departed from the main system at about 20.40 UTC and farther moved north. At first, this part of MCS kept its strength and individuality but later on started to dissolve quickly. At the same time, on the eastern MCS flank, its eastern thunderstorm part was also weakening. Then the main convection areas entered the Vistula river delta and, still weakening, moved northeast towards the Courland. At the same time, the weak convection region of the MCS western flank was taken by its western branch, and then weakened, entering the area of the Gdańsk Bay. Such a final stage of the considered MCS development is presented in Fig. 35 by the time sequence of six maps given with the 20-minute time step.

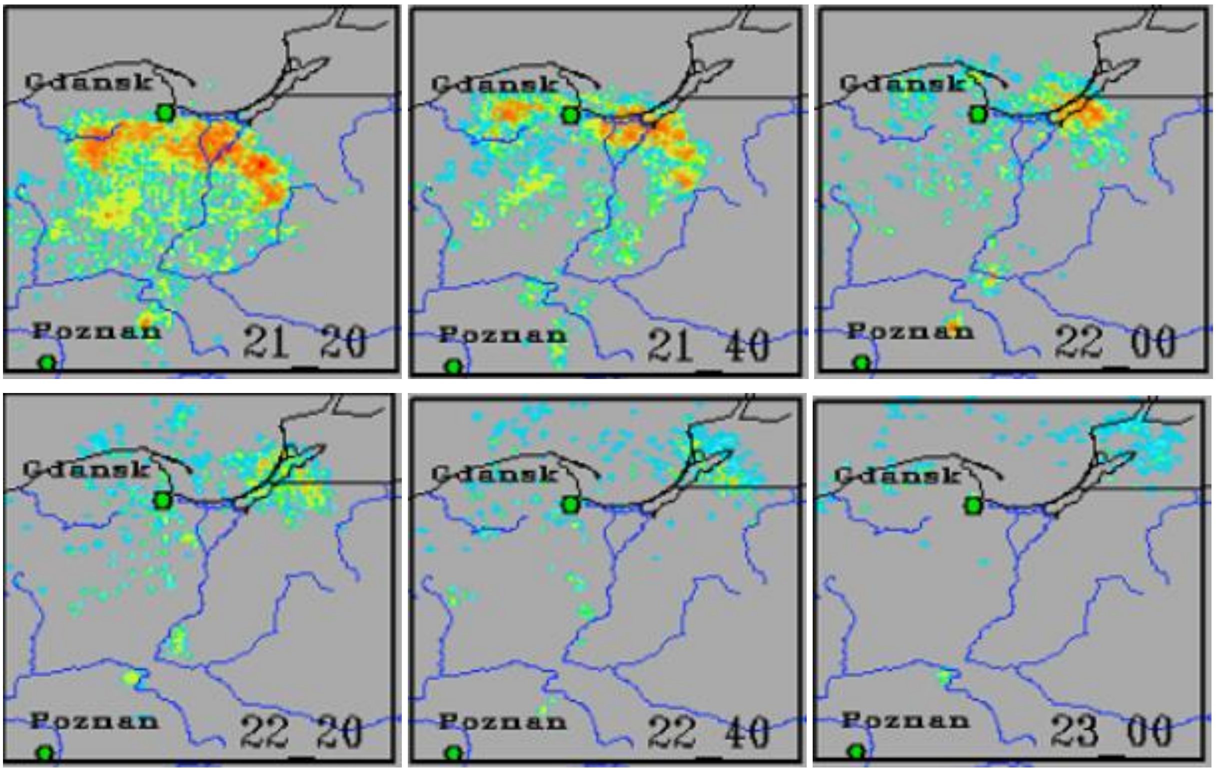

Fig. 35. Time sequence of six maps given with the 20-minute time step, presenting the relevant electrical activity changes during the final MCS development stage that lasted from 21:00 to 23:00 UTC.

The synoptic context of the last MCS development stage with the degradation phase that lasted from 21:10 to 23:50 UTC is presented in Figs. 36–39 by the set of four maps for *p3D*, (teta), *RoV*, and *Rot* parameters simulated at 23:45 UTC together with the adequate 3D wind field taken from the NWP model and lightning discharge detections obtained from the PERUN

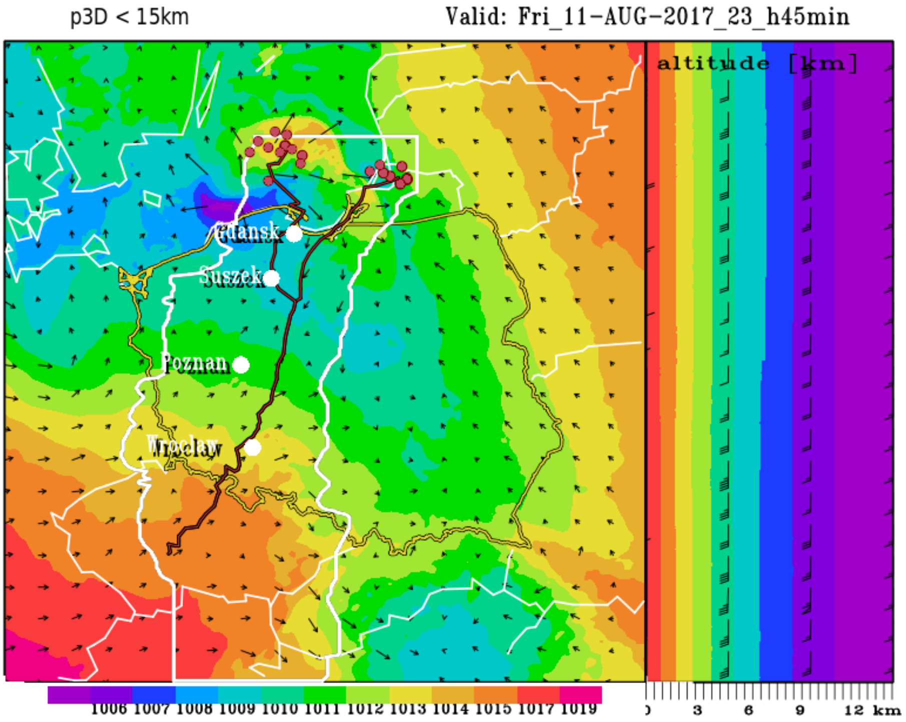

Fig. 36. The same as in Fig. 17, but showing the pattern for the simulated map of the *p3D* parameter and lightning activity calculated at 23:45 UTC.

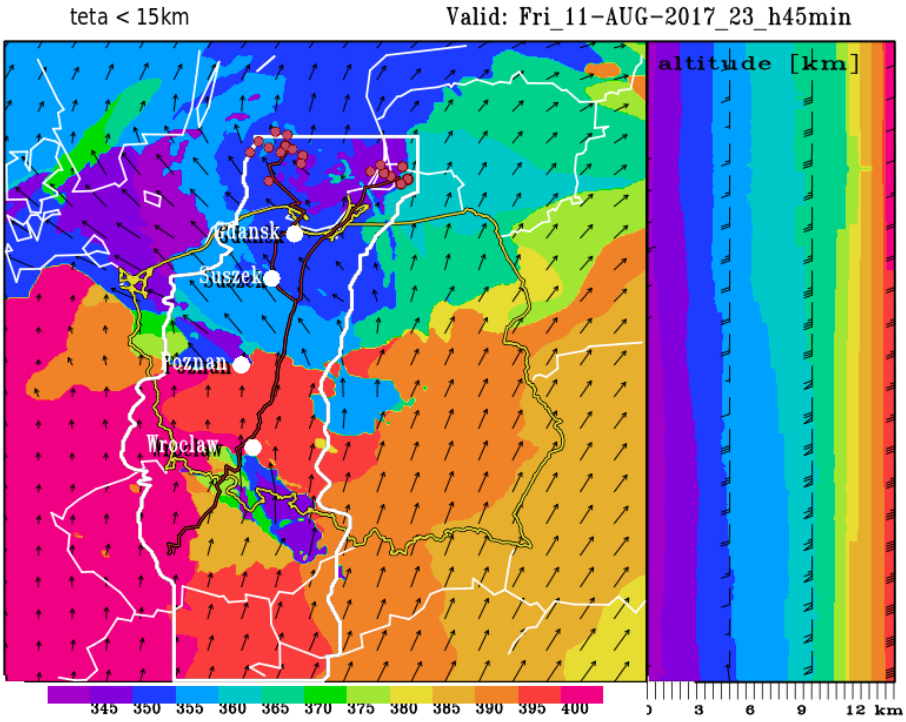

Fig. 37. The same as in Fig. 18, but showing the pattern for the simulated map of the (teta) parameter and lightning activity calculated at 23:45 UTC.

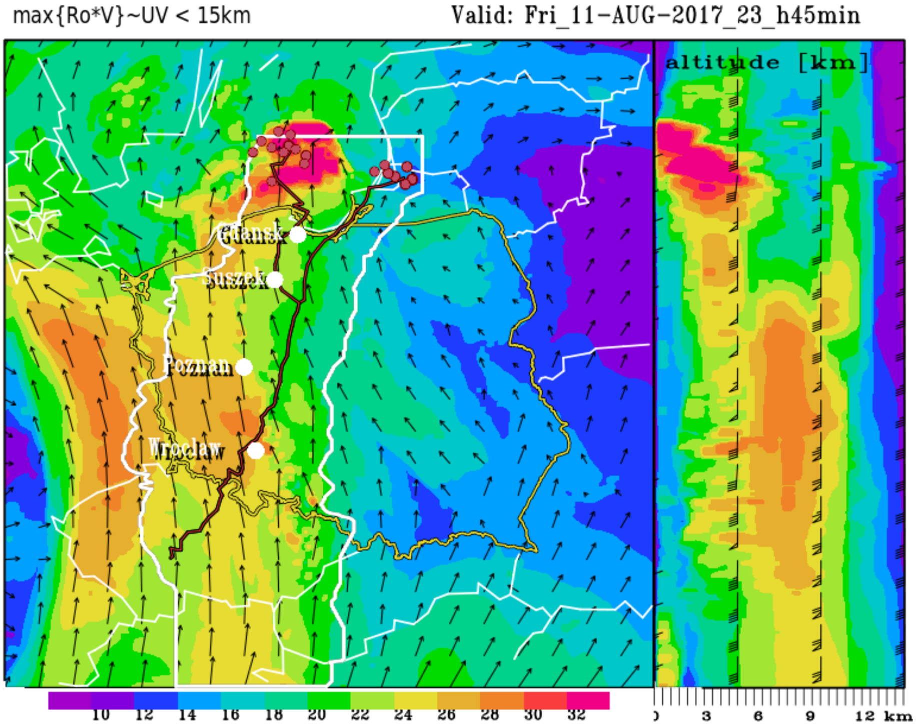

Fig. 38. The same as in Fig. 19, but showing the pattern for the simulated map of the *RoV* parameter and lightning activity calculated at 23:45 UTC.

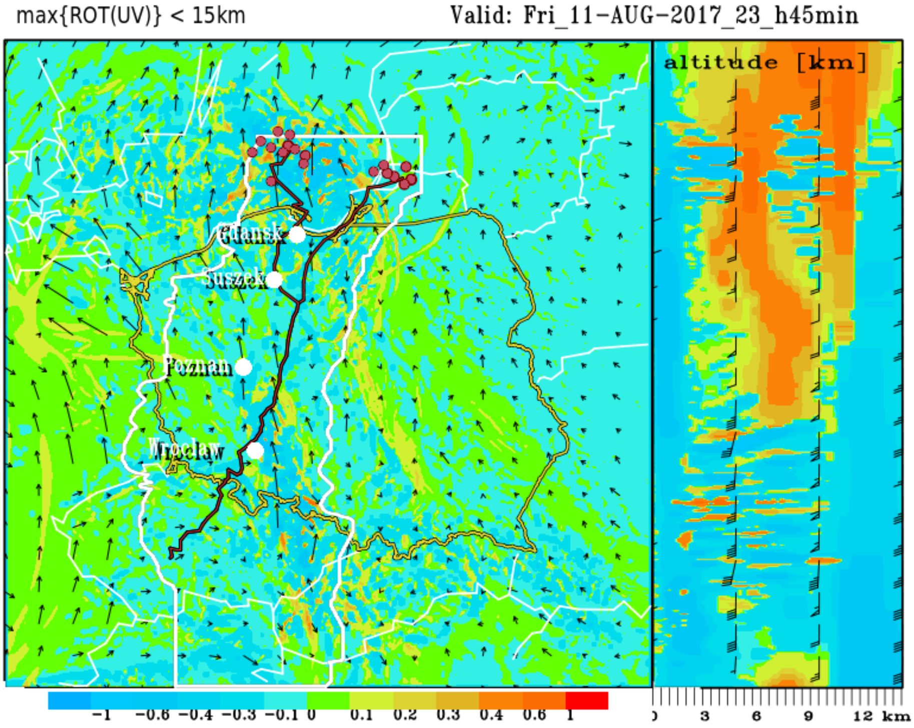

Fig. 39. The same as in Fig. 20, but showing the pattern for the simulated map of the *Rot* parameter and lightning activity calculated at 23:45 UTC.

data. Additionally, the METEOSAT SEVIRI color-enhanced IR brightness temperature image cofirming the final MCS degradation together with its split and taken from the EUMETSAT 2017 database at 23:45 UTC is given in Fig. 40.

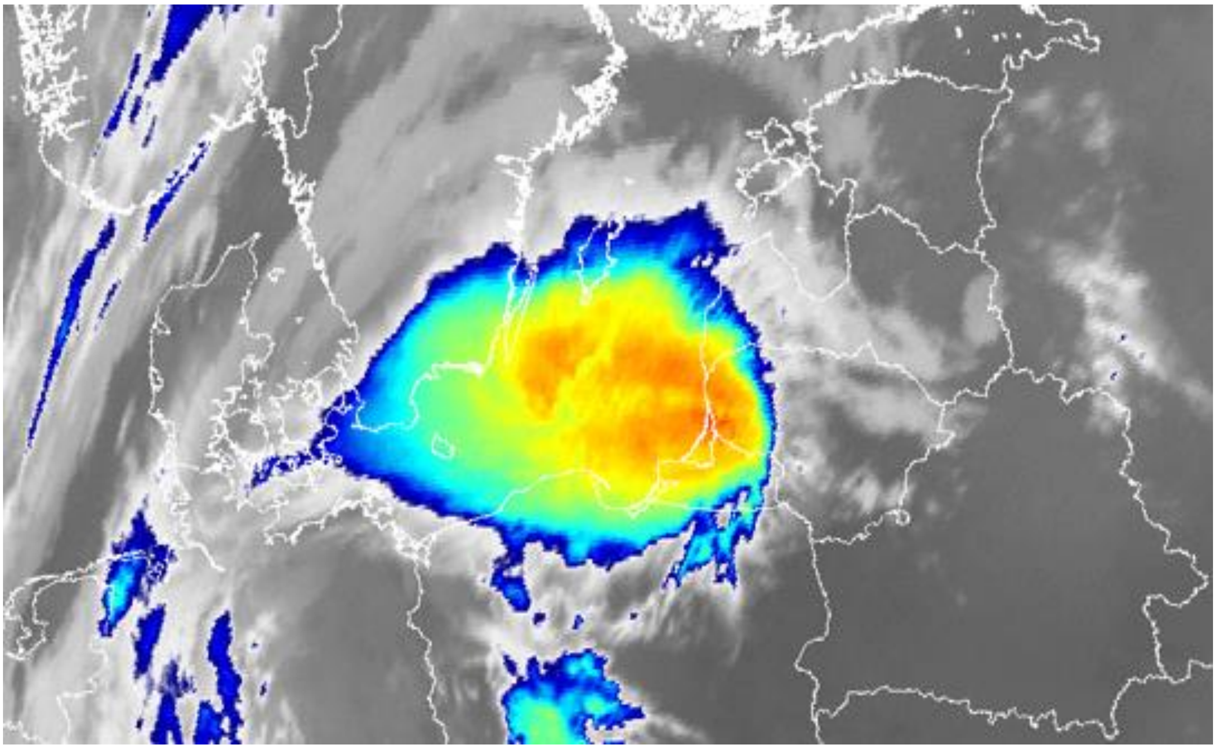

Fig. 40. METEOSAT SEVIRI color-enhanced IR brightness temperature image at 23:45 UTC on 11 August 2017 (© EUMETSAT 2017, © dane.sat4envi.imgw.pl, © OpenStreetMap contributors, reported also by Łapeta et al. (2021)).

A characteristic feature of this process, given in Figs. 35–39, was a distinct weakening and degradation of the whole MCS. As it was shown in Fig. 15, after 22:10 UTC, all VFS values are below 1. It is interesting that in the area of Wrocław at 22:10 UTC new lightning discharges are detected as a replica of a later derecho episode and they move farther north, reaching Poznań. But this lightning discharges zone lies far south of the considered supercell, which lasts itself until the end of the study period, i.e., 00:00 UTC on the next day, 12 August 2017. Its decay will come later.

In turn, as it can be retrieved from Fig. 36, the pressure depression noticeably weakens and decreases in the considered area after 23:15 UTC. Nevertheless, at the ground-level, the wind field pattern is a characteristic peculiarity indicating a strong downburst combined with a horizontal outbreak. Moreover, we can find from Fig. 37 that the tropopause depression still accompanies MCS, including both propagation paths with two characteristic discharge groups, but the area of low potential temperature values has shrunk considerably. On the other hand, based on Fig. 38 it can be noticed that the power to the considered MCS is cut off through the nucleus of the tropospheric jet after 22:45 UTC. However, the maximum of air momentum is concentrated below 3 km, while, after 21:30 UTC, in the vicinity of the western border of Poland, the jet stream is fragmented into a western branch, associated with the mother cyclone from above Germany, and an eastern branch controlling the following derecho episode. However, the whole MCS is weakening but not fading away. Finally, as can be seen in Fig. 39, the negative (anticyclonic) rotation dominates the considered supercell area from 21:30 UTC. In this final evolution phase, at 23:15 UTC, the whole MCS divides definitively into two areas. As for the vertical currents, given by the *W3D* parameter, they remain until the end of the period under study, i.e., until 00:00 UTC of the next day, 12 August 2017, but after 20:45 UTC their domain shrinks noticeably. The turbulence index PT_{Ri} remains unchanged in area, but its values in the middle troposphere are getting weaker.

6. CONCLUSIONS

According to the evaluation of Parfiniewicz and Konarski (2016), the MCS with the derecho episode over Poland on 11 August 2017, reaching the maximum value of VFS number equal to 3.93, was not a strong convective incident on the European scale. The main MCS propagation path expressed in the coordinates of the COSMO_2.8 km model was abstracted and then used to determine the propagation speed of this convection system. These calculations were performed only for the main MCS propagation path. The highest estimated propagation speed, up to 40 m/s, occurred around 19:30 UTC, preceding the MCS path split. Although the calculated MCS propagation speeds are burdened with some errors, they still remain fairly consistent with the telemetry and damage measurements reported by Mańczak et al. (2021), Wrona et al. (2022), and Taszarek et al. (2019a,b). The basic characteristic parameters, such as the traveled distance, the lifetime, and the average propagation speed of the considered MCS with the derecho event were also estimated. They were equal to 864.42 km, 11.17 hours, and 21.50 m/s, i.e., 77.4 km/h, respectively. Moreover, 24 records of wind gusts exceeding 20 m/s were shown by the telemetry data gathered along the evaluated MCS path. Although those severe wind gusts were noted on both sides of the main MCS track, the wind gusts activity seemed to be dominant on the MCS west side and well correlated with the most spectacular damages reported in the Bory Tucholskie Forest. Certainly, the derecho electrical activity dominated the eastern MCS flank, but for understandable reasons, most of the attention in the papers cited above was focused on the analysis of the western MCS flank,well documented by the radar data from Poznań and Gdańsk. The review and analysis of 144 maps displaying the evolution of MCS electrical activity expressed by changes of the relevant VFS number allowed to describe and present all MCS development stages, including this remarkable episode of the “Suszek” convection incident and other MCS essential details responsible for its electrical activity. It was done in a novelty way which, to our best knowledge, has never been used in any published papers dealing with this case of MCS. Our individual approach to this study complements and well validates other phenomenological evaluations related to the assessment of such severe convection episodes. The considered MCS case of the very fast-moving convective system is significantly different from the cases we have studied earlier and that occurred in Poland, e.g., the stormy day on 28 March 1997 with the hurricane incident on the Baltic Sea analyzed in Parfiniewicz (2001) or the tornado case of 20 July 2007 reported by Parfiniewicz et al. (2009) and Parfiniewicz (2014). No doubt, a better understanding of each MCS case and processes involved in its development requires a separate and detailed diagnosis in different fields, while our paper dealing with this issue is phenomenological in nature and is only a modest contribution to the achievement of such a primary goal. At the end, we should also underline that our idea of the conversion of the primary lightning discharge density field to the presentation of this field by the particular scalar value of the relevant VFS number based on two empirical formulas, given in Section 4 by Eqs. (1)–(2), was successfully implemented to some nowcasting procedures used by the internet portal of awiacja_imgw_pl to indicate – on the background of thunderclouds radar reflectivity – their areas where the vigorous convection development was anticipated, posing a danger for people, different objects of ground infrastructure, or even for plane communication.

Acknowledgments. We express our gratitude to Dr. Michał Ziemiański, expert in meteorology, for his effective, meaningful, and creative support. Many thanks to Mrs. Marzena Kawecka and prof. Jan Szturc for the rainfall data from the INKA system, and also to Anna

Goławska for providing valuable supplementary telemetry data. To Jerzy Konarski and Wojciech Gajda for PERUN data and to Wiesław Łazarewicz and Jan Walasek for joint works on nowcasting thunderstorms for https://awiacja.imgw.pl/. We also thank the reviewers for their insightful comments and valuable advice. Chapter 5 of this work, devoted to the evolution of the MCS on a synoptic background, was made on the computing infrastructure of the Interdisciplinary Centre for Mathematical and Computational Modelling (ICM) of the University of Warsaw under the Allocation No. G88-1220: "Suszek".

References

Barański, P., and J. Parfiniewicz (2019), The derecho episode in the Bory Tucholskie district 11 August 2017 – the present state of the predicting severe storms by awiacja_imgw_pl. **In:** *Proc. 10th European Conference on Severe Storms, 4–8 November 2019, Kraków, Poland*, ECSS2019-6-2, DOI: 10.13140/RG.2.2.19737.36965.

Bodzak, P., Z. Dziewit, and W. Gajda (2006), The ratio of cloud to cloud-to-ground flashes in summer seasons for Poland territory on the basis of data from PERUN system. **In:** *Proc. 19th International Lightning Detection Conference, 24–25 April 2006, Tucson, USA*.

Celiński-Mysław, D., and D. Matuszko (2014), An analysis of selected cases of derecho in Poland, *Atmos. Res.* **149**, 263–281, DOI: 10.1016/j.atmosres.2014.06.016.

Fujita, T.T. (1978), Manual of downburst identification for project NIMROD, Satellite and Mesometeorology Research Project, The University of Chicago, Research Paper No. 156, 104 pp.

Lelątko, I. (2020), Ekstremalnie silne porywy wiatru 11 sierpnia 2017. Wstępna analiza przypadku z punktu widzenia pracy operacyjnej IMWM–NRI CBPM Kraków, available from: http://intranet.imgw.ad/wp-content/uploads/2020/11/BowEchoOf 11 August 2017Iwona.pdf (in Polish).

Łapeta, B., E. Kuligowska, P. Murzyn, and P. Struzik (2021), Monitoring the 11 August 2017 storm in central Poland with satellite data and products, *Meteorol. Hydrol. Water Manage.*, DOI: 10.26491/mhwm/144590.

Łuszczewski, H., and I. Tuszyńska (2022), Derecho radar analysis of August 11, 2017, *Meteorol. Hydrol. Water Manage.*, DOI: 10.26491/mhwm/152504.

Mańczak, P., B. Wrona, A. Woźniak, M. Ogrodnik, and M. Folwarski (2021), Synoptic analysis of derecho over Poland on 11 July 2017, *Meteorol. Hydrol. Water Manage.* (submitted).

Marshall, J.S., and W. Mc K. Palmer (1948), The distribution of raindrops with size, *J. Meteorol.* **5**, 4, 165–166, DOI: 10.1175/1520-0469(1948)005 <0165:TDORWS>2.0.CO;2.

Mazur, A., G. Duniec, W. Interewicz, and A. Wyszogrodzki (2019), Ensemble forecasting of extreme convective phenomena using universal tornadic index. **In:** *Proc. 10th European Conference on Severe Storms, 4–8 November 2019, Kraków, Poland*, ECSS2019-57.

Parfiniewicz, J.W. (2001), Addendum to "Diagnostic study – storm over Poland", *Meteorol. Z.* **10**, 2, 151–152, DOI: 10.1127/0941-2948/2001/0010-0151.

Parfiniewicz, J. (2012), Concerning Thunderstorm Potential prediction. **In:** *The European Meteorological Society Annual Meeting Abstracts*, Vol. 9, No. EMS2012-81, 12th EMS / 9th ECAC, available from: http://meetingorganizer.copernicus.org/EMS2012/EMS2012-81.pdf.

Parfiniewicz, J. (2013), Nowcasting strong convective events (SCE) – the thunderstorm thermometer. **In:** *Meteorological Technology World Expo 2013 Preview*, available from: http://www.ukintpressconferences.com/uploads/SPMTWX13/Breakout_Session_d2_s2_p5_Jan_Parfiniewicz.pdf; http://viewer.zmags.com/publication/f088b3fc#/f088b3fc/62.

Parfiniewicz, J. (2014), Steps to a storm – forecasting and nowcasting strong convective events, *Meteorol. Technol. Int.* **April 2014**, 48–51, available from: http://viewer.zmags.com/publication/c4f984ab#/c4f984ab/50.

Parfiniewicz, J., and P. Barański (2014), An explosive convection over Europe with 8-minute tornado incident in Poland on July 20, 2007, *Int. J. Environ. Eng. Nat. Resour.* **1**, 6, 262–276.

Parfiniewicz, J., and G. Bojanek (2013), Jak możemy pomóc w weryfikacji prognoz turbulencji CAT? Dlapilota.pl, Prognozowanie Clear Air Turbulence, available from: http://dlapilota.pl/wiadomosci/dlapilota/jak-mozemy-pomoc-w-weryfikacji-prognoz-turbulencji-cat (accessed: 21 November 2013) (in Polish).

Parfiniewicz, J., and J. Konarski (2016), On thunderstorm quantification (continuation), *COSMO Newslett.* **16**, 13–15, DOI: 10.13140/rg.2.2.29118.08007.

Parfiniewicz, J., P. Barański, and W. Gajda (2009), Preliminary analysis of dynamic evolution and lightning activity associated with supercell event: case story of the severe storm with tornado and two heavy hail gushes in Poland on 20 July 2007, *Publs. Inst. Geoph. PAS* **D-73 (412)**, 65–88.

Richard, P., and J.Y. Lojou (1996), Assessment of application of storm cell electrical activity monitoring to intense precipitation forecast. **In:** *Proceedings: 10th International Conference on Atmospheric Electricity, June 10–14, 1996*, International Commission of Atmospheric Electricity, Osaka, Japan, 284–287.

Setvák, M., D.T. Lindsey, P. Novák, P.K. Wang, M. Radová, J. Kerkmann, L. Grasso, S.-H. Su, R.M. Rabin, J. Šťástka, and Z. Charvát (2010), Satellite-observed cold-ring-shaped features atop deep convective clouds, *Atmos. Res.* **97**, 1–2, 80–96, DOI: 10.1016/j.atmosres.2010.03.009.

Szturc, J., A. Jurczyk, K. Ośródka, A. Wyszogrodzki, and M. Giszterowicz (2018), Precipitation estimation and nowcasting at IMGW-PIB (SEiNO system), *Meteorol. Hydrol. Water Manage.* **6**, 1, 3–12, DOI: 10.26491/mhwm/76120.

Taszarek, M., N. Pilguj, J. Orlikowski, A. Surowiecki, S. Walczakiewicz, W. Pilorz, K. Piasecki, Ł. Pajurek, and M. Półrolniczak (2019a), Derecho evolving from a mesocyclone—a study of 11 August 2017 severe weather outbreak in Poland: event analysis and high-resolution simulation, *Mon. Wea. Rev.* **147**, 6, 2283–2306, DOI: 10.1175/MWR-D-18-0330.1.

Taszarek, M., N. Pilguj, J. Orlikowski, A. Surowiecki, S. Walczakiewicz, W. Pilorz, K. Piasecki, Ł. Pajurek, and M. Półrolniczak (2019b), Derecho evolving from a mesocyclone—a study of 11 August 2017 severe weather outbreak in Poland: event analysis and high-resolution simulation, ECSS2019-77, 4–8 November 2019, Kraków, Poland.

Wrona, B., P. Mańczak, A. Woźniak, M. Ogrodnik, and M. Folwarski (2022), Synoptic conditions of the derecho storm. Case study of the derecho event over Poland on August 11, 2017, *Meteorol. Hydrol. Water Manage.*, DOI: 10.26491/mhwm/152798.

Received 16 September 2022
Received in revised form 30 December 2022
Accepted 31 December 2022

"Publications of the Institute of Geophysics, Polish Academy of Sciences: Geophysical Data Bases, Processing and Instrumentation" appears in the following series:

A – Physics of the Earth's Interior

B – Seismology

C – Geomagnetism

D – Physics of the Atmosphere

E – Hydrology (formerly Water Resources)

P – Polar Research

M – Miscellanea

Every volume has two numbers: the first one is the consecutive number of the journal and the second one (in brackets) is the current number in the series.